Title
Multiscale Modeling and Homogenization of Composite Materials

Permalink
https://escholarship.org/uc/item/5wt609sz

Author
Mseis, George

Publication Date
2010

Peer reviewed|Thesis/dissertation

Multiscale Modeling and Homogenization of Composite Materials

by

George Mseis

A dissertation submitted in partial satisfaction of the
requirements for the degree of
Doctor of Philosophy

in

Mechanical Engineering

in the

GRADUATE DIVISION
of the
UNIVERSITY OF CALIFORNIA, BERKELEY

Committee in charge:

Professor Tarek Zohdi, Chair
Professor George Johnson
Professor Jon Wilkening

Fall 2010

Multiscale Modeling and Homogenization of Composite Materials

Abstract

Multiscale Modeling and Homogenization of Composite Materials

by

George Mseis

Doctor of Philosophy in Mechanical Engineering

University of California at Berkeley

Professor Tarek Zohdi, Chair

In this study we analyze a method for the multiscale modeling of heterogeneous materials with a special emphasis on unidirectional fiber composites. The method relies on defining two problems. The first boundary value problem is defined with homogenized material properties and the second boundary value problem is defined with the exact heterogenous properties. Based on these definitions a modeling error between these two problems is defined and analyzed for both small deformation and finite deformation cases. We introduce a new modeling error that gives insight into the components that contribute to this error. To improve the solution of the homogenized problem without solving the complete heterogeneous problem, we define subdomains that include microstructural information. These smaller subdomains can then be solved and included into the solution space of the homogeneous problem through a simple coupling process. Through defining local error indicators that are related to the global modeling error, we can adaptively select only the subdomains with high local error to be included in the solution space. As a preset to the multiscale process, homogenization techniques are analyzed for random unidirectional fiber composites under small deformations. This allows one to systematically obtain material properties for the homogenized boundary value problem. A thorough analysis is provided to understand the behavior of the error indicator under both small and finite deformations. We also explore the potential reduction in the modeling error when including subdomains in the solution space. The effect the size of the subdomains have on the solution improvement is also investigated.

Professor Tarek Zohdi
Dissertation Committee Chair

Dedicated to My Family,

My Wife, Saira, My Mother, Rita, My Father, Nadim and My Sister, Natalie

Contents

List of Figures

List of Tables

Acknowledgements

I would like to first and foremost thank my advisor, Professor Tarek Zohdi, for his continuous support and guidance. He has been generously patient with me and my constant questions. He also made my transition to Berkeley seamless and I'm thankful for all the opportunities he provided.

I would also like to thank my committee members, Professor George Johnson and Professor Jon Wilkening, for their feedback and advice during this process. They have both enriched my education through the wonderful courses they offered.

While at Berkeley I've had wonderful experiences and this has been exemplified by the number of amazing people I have met in the computational materials lab and outside this lab. During these past four years I have developed lasting friendships with many people. These friendships have enriched both my understanding of mechanics, science, and have given me an added appreciation of life. In the computational materials lab I would like to thank all of my lab mates including, Doron Klepach who has been a constant help and has endured my complaints and doubts through this process; he has been a great friend. Frank Dirksen who among many things introduced me to using white boards for collaborative discussions that have undoubtedly enriched my learning experience, I would have enjoyed it had Frank stayed at Berkeley for his PhD. Lik Chuan Lee, Tim Kostka and Ryan Krone with whom I've had many discussions and collaborations. Also, Gilles Lubineau, Phillp Gloesmann and Sebastian Trimpe who as visiting scholars were inspiring to have in the lab. From outside my lab, I would like acknowledge Gary Templet for the many discussions we've had and especially for introducing me to Cajun food and Neil Hodge for insight in many issues related to mechanics and for his help with my job search. I've enjoyed many outings that I will cherish with all of these friends and many more.

My family has been an unrelenting source of support and inspiration. Their sacrifices and unwavering dedication have allowed me to pursue my dreams, without them I would not be here. Last but not least, I would like to thank my wife, Saira, for her never ending patience and support. She has been a constant source of love and inspiration. Her encouragement and sense of calm kept my sanity throughout this endeavor in check. Without her this would have been a lonely adventure.

Chapter 1

Introduction

Materials consist of multiple scales. This is true for both engineering and natural materials. Specifically, there are different length scales of importance depending on the type of material of interest. There are many examples of materials which exhibit a strong dependence on the various length scales. For example we note, biological materials, composite materials, soils, rocks and even metals. When considering biological or composite materials the information at the fiber length scale is crucial to the material response at the continuum or large scale. Metals on the other hand are made up of grains and from a damage and failure point of view this length scale is important. The process in which we include the effects of the different length scales is known as multiscale modeling.

Our interest focuses on composites which have been playing an increasingly significant role in engineering design. They usually consist of two constituents, a reinforcing agent and a supporting matrix. Typically, the reinforcing component is stiffer than the matrix. There are many types of composites including particle composites and fiber composites. The most common used in engineering design are unidirectional fiber composites. We call a single layer of unidirectional fiber composite a ply. Composites have been incorporated in products ranging from aircrafts to golf clubs. Their popularity is mainly the consequence of two significant advantages. The first is the inherent ability to tailor the material response through varying the stacking sequence of unidirectional plys. The second is the high stiffness to density ratio when compared to traditional engineering materials such as metals. This in turn has resulted in a demand for higher fidelity computational simulations of composites that account for the micro-structural constituents.

The standard approach to model composite materials is to use the finite element method. In particular, since accounting for all the micro-structural components in a numerical setting is not feasible, we assume homogeneous material properties obtained either from analytical bounds or through the process of numerical homogenization. This allows us to solve large scale problems with minimal computational power. We then take advantage of the nature of composite materials and utilize mutiscale modeling by including the effects of the fiber-matrix combination.

1.1 Research Objectives and Thesis Outline

In this thesis two interconnected topics are explored. The first is the concept of homogenization, which is the process of obtaining constitutive information on the continuum or large scale from the smaller length scale that includes pertinent micro-structural information. For composite materials, which is the focus of this dissertation, the fiber-matrix combination is explicitly modeled. There has been extensive research in homogenization techniques, for an extensive overview refer to Nemat-Nasser and Hori [1] and Aboudi [2]. The notion of homogenization in this thesis is limited to the *Average-field theory* as described in Hori and Nemat-Nasser [3], where by the homogenization process is conducted to obtain macroscopic constitutive equations independent of a multiscale or coupled process. Our interest here lies in understanding the effects of using randomly distributed unidirectional fibers on the overall constitutive response. These numerical results are in turn compared to some traditional analytical results such as those of Hill and Hashin-Rosen [4]. We also explore obtaining converged representative volume element sizes for different fiber volume fractions.

The second concept is the process of multiscale modeling of unidirectional fiber composites, although homogenization is inherently a multiscale process, we make a clear distinction. Particularly, in multiscale modeling the small length scale information enriches the response of the large scale continuum in a coupled manner. There is a coupled solution of both the macroscale and microscale. Therefore, the kinematics and kinetics of both scales are explicitly related. This allows us to extract stress-strain information at both scales. There are a number of approaches for conducting multiscale analysis, many of which depend on the assumption that the microstructure is spatially periodic and that the solution space

is also periodic. A review of these types of methods can be found in Bensoussan [5], Fish [6], Allen [7] and Chung [8] and are generally known as asymptotic methods . Extensions to non-periodic micro-structures can be found in Fish [9] and Ghosh [10] who innovated the voronoi cell finite element method allowing for arbitrary heterogeneous materials. These approaches are generally applied to small strain cases. Another approach, defines representative volume elements at each integration point in a finite element analysis and utilizes the average-field theorems used in homogenization to obtain macroscopic stresses and strains and in turn for nonlinear analysis one can obtain the consistent tangent modulus. A review of these types of approaches can be found in Kouznetsova. [11], Miehe [12] and Chaboche [13] . Specific applications of these types of multiscale methods can be found in Arkaprabha et al [14] where attention was dedicated to superelasticity of Nitinol polycrystals and in Nadler and Papadopoulos [15] where a multiscale fabric model was introduced.

Our approach utilizes the concept of defining local error estimators that indicate in which regions of the large scale the local small scale is necessary to improve the global solution. This method is based on the works of Zohdi et al [16]-[17] where error estimators are introduced and analyzed for small strain and macroscopically isotropic materials. We initially analyze this method for small strains and macroscopically anisotropic materials and then extend the approach to large deformations. The objective is to assess the improvement in the solution space as a result of this type of multiscale analysis. An advantage of using error estimators is the ability to choose specific regions in which to include the micro-structural effects. This in turn allows us to reduce the computational cost of the multiscale process. Additionally, the effect of including some regions with microstructure into the global solution space is investigated for both small strains and large deformations.

The dissertation is organized as follows. We start by introducing the concepts of continuum mechanics in Chapter 2. In Chapter 3, we derive the finite element method for finite elasticity. We then in Chapter 4 introduce the concepts of homogenization in linear elasticity. Numerical experiments are then conducted on representative volume elements for random unidirectional fibers in Chapter 5. We move on to the multiscale modeling in Chapter 6 and give an introduction to the concepts by deriving some modeling error bounds. The analysis for multiscale modeling under the assumptions of linear elasticity are provided in Chapter 7, along with subdomain construction concepts. In Chapter 8, we include large deformations and analyze the accuracy of the global error bounds. We then, in

Chapter 9, conduct the multiscale analysis with large deformation by utilizing the concepts of subdomain construction. Finally, in Chapter 10 we close with conclusions.

Chapter 2

Continuum Mechanics Basics

In this chapter, fundamental concepts in continuum mechanics are introduced. For a full review of the subject refer to the works of Chadwick. [18], Spencer. [19] and Holzapfel. [20] and the references therein.

2.1   Kinematics

Kinematics is the study of motion without considering the forces that produce these motions. We start by introducing the kinematic considerations when analyzing continuum bodies. Specifically, we define a body $\mathcal{B}$ whose elements or particles $\mathcal{P}$ can be placed into a configuration $\mathcal{R}_0 \in R^3$ at time $t = 0$. Each particle $\mathcal{P}$ is associated with a unique position $\mathbf{X}$ in $\mathcal{R}_0$ defined relative to an origin O_0 with base vectors $\mathbf{E}_i$. The configuration at $t = 0$ is called the reference configuration. We now consider that the body $\mathcal{B}$ moves and assumes a new configuration $\mathcal{R} \in R^3$ at $t > 0$. The particles $\mathcal{P}$ now assume a new unique position defined by the vector $\mathbf{x}$ with respect to an origin O with base vectors $\mathbf{e}_i$. This new configuration at $t > 0$ is called the current configuration. Figure. 2.1 shows a schematic of the body $\mathcal{B}$ in its reference configuration and current configurations.

The motion involved in going from the reference configuration to the current configuration can be described through the function $\mathcal{X}(\cdot)$ such that

$$\mathbf{x} = \mathcal{X}(\mathbf{X}, t) \tag{2.1.1}$$

Therefore, we can express the complete motion of the body $\mathcal{B}$ as function of the positions
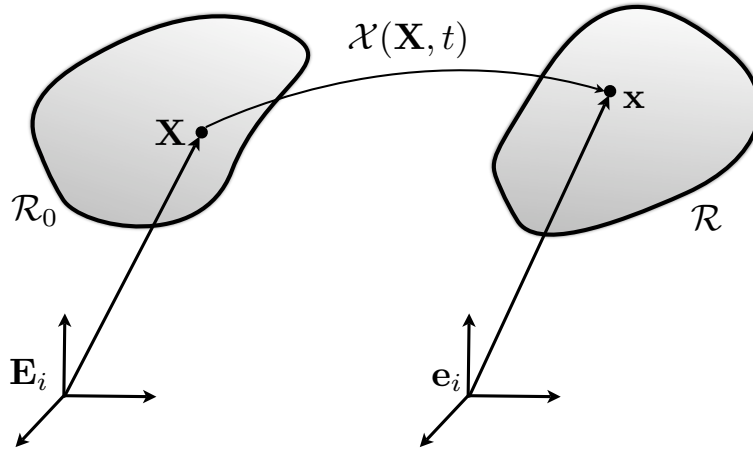
Figure 2.1: Schematics of reference and current configurations with base vectors

$\mathbf{X}$ in the reference configuration. We assume that the relation in Eqn. 2.1.1 can be inverted to get $\mathbf{X} = \mathcal{X}^{-1}(\mathbf{x}, t)$.

Given the relationship in Eqn. 2.1.1 we calculate the gradient of the motion as

$$\begin{aligned} \mathbf{F} &= \frac{\partial \mathcal{X}(\mathbf{X}, t)}{\partial \mathbf{X}} \\ &= \frac{\partial \mathbf{x}}{\partial \mathbf{X}} = \frac{\partial x_i}{\partial X_A} \mathbf{e}_i \otimes \mathbf{E}_A \end{aligned} \tag{2.1.2}$$

where $\mathbf{F} = F_{iA} \mathbf{e}_i \otimes \mathbf{E}_A$ is known as the deformation gradient and since it has one component in the current configuration $\mathbf{e}_i$ and the other component in the reference configuration $\mathbf{E}_A$ it is considered a mixed tensor,. We assume the function $\mathcal{X}(\cdot)$ is smooth enough and that the inverse of $\mathbf{F}$ exists and is defined as

$$\begin{aligned} \mathbf{F}^{-1} &= \frac{\partial \mathcal{X}^{-1}(\mathbf{x}, t)}{\partial \mathbf{x}} \\ &= \frac{\partial \mathbf{X}}{\partial \mathbf{x}} = \frac{\partial X_A}{\partial x_i} \mathbf{E}_A \otimes \mathbf{e}_i \end{aligned} \tag{2.1.3}$$

We also have that $J = \det \mathbf{F} \neq 0$ which is known as the Jacobian. We can also define the displacement vector as $\mathbf{u} = \mathbf{x} - \mathbf{X}$ and write the deformation gradient as

$$\mathbf{F} = \mathbf{H} + \mathbf{I} \tag{2.1.4}$$

where $\mathbf{H} = \frac{d\mathbf{u}}{d\mathbf{X}}$ and $\mathbf{I}$ is the identity tensor. The deformation gradient is used to get relations between the reference and current configurations for line elements, area elements and volume elements. Specifically, for line elements we have

$$d\mathbf{x} = \mathbf{F} d\mathbf{X} \tag{2.1.5}$$

and for an area element we can derive [18] the expression

$$\mathbf{n} da = J\mathbf{F}^{-T}\mathbf{N} dA \tag{2.1.6}$$

which is known as Nanson's formula and $\mathbf{n}, \mathbf{N}$ are the unit normals defining an area element in the current and reference configurations, respectively. Finally, we can express the relationship between the reference and current configuration volumes as

$$dv = J dV \tag{2.1.7}$$

where dv and dV are volume elements in the current and reference configuration respectively. Derivations for these expressions can be be found in Chadwick. [18].

We also note the polar decomposition of $\mathbf{F}$ into stretch and rotation components as

$$\mathbf{F} = \mathbf{R}\mathbf{U} \qquad \text{and} \qquad \mathbf{F} = \mathbf{V}\mathbf{R} \tag{2.1.8}$$

where $\mathbf{U}$ and $\mathbf{V}$ are symmetric positive definite tensors defining the stretch of the material in the reference and current configurations respectively. Also, $\mathbf{R}$ is a proper orthogonal tensor $(\det(\mathbf{R}) = 1)$ defining the rotation of the principle axes. This interpretation of $\mathbf{R}$

can easily be seen if we write $\mathbf{U}$ or $\mathbf{V}$ in spectral form and then expressing $\mathbf{F}$ in it's polar decomposition form thus,

$$\mathbf{F} = \mathbf{RU} \tag{2.1.9}$$

$$= \mathbf{R} \sum_{i=1}^{3} \lambda_i \mathbf{u}_i \otimes \mathbf{u}_i = \sum_{i=1}^{3} \lambda_i \mathbf{R} \mathbf{u}_i \otimes \mathbf{u}_i \tag{2.1.10}$$

such that λ_i are the eigenvalues and $\mathbf{u}_i$ are the eigenvectors of the stretch tensor $\mathbf{U}$ and we note that $\mathbf{v}_i = \mathbf{R}\mathbf{u}_i$ are the eigenvectors of $\mathbf{V}$.

2.2 Strain Concepts

Strain can be expressed or defined in multiple ways. We start by deriving an expression for the stretch of a material element. Consider the reference material line $d\mathbf{X} = dS\mathbf{M}$ where dS is the length of the material line and $\mathbf{M}$ is the unit vector defining the orientation. This line element in the current configuration is $d\mathbf{x} = ds\mathbf{m}$ where ds is the length of the material line and $\mathbf{m}$ is the unit vector defining the orientation. Recalling, the relationship between material lines $d\mathbf{x} = \mathbf{F}d\mathbf{X}$ we have

$$ds\mathbf{m} = \mathbf{F}dS\mathbf{M} \tag{2.2.1}$$

taking the dot product of each side in the above we get

$$ds^2\mathbf{m} \cdot \mathbf{m} = dS^2\mathbf{FM} \cdot \mathbf{FM} \rightarrow \frac{ds^2}{dS^2} = \mathbf{M} \cdot \mathbf{F^T FM}$$
$$= \mathbf{M} \cdot \mathbf{CM} \tag{2.2.2}$$

where $\mathbf{C} = \mathbf{F}^T \mathbf{F}$ is called the right-Cauchy-Green tensor. We therefore have an expression for the stretch ($\lambda = \frac{ds}{dS}$) of a line element defined as

$$\lambda^2 = \mathbf{M} \cdot \mathbf{CM} \tag{2.2.3}$$

With a similar approach we can also obtain $\mathbf{B} = \mathbf{F}^{-1}\mathbf{F}^{-T}$ which is known as the left-Cauchy-Green tensor.

One form of a strain measure can be expressed as $\frac{1}{2}\frac{ds^2 - dS^2}{dS^2}$, which is the change in length of a line element non-dimensionalzed with respect to the original length. From this expression we can obain

$$
\begin{aligned}
\frac{1}{2}\frac{ds^2 - dS^2}{dS^2} &= \frac{1}{2}\frac{ds^2}{dS^2} - \frac{dS^2}{dS^2} \\
&= \frac{1}{2}\left(\lambda^2 - 1\right) \\
&= \frac{1}{2}\left(\mathbf{M} \cdot \mathbf{CM} - 1\right) \\
&= \mathbf{M} \cdot \frac{1}{2}\left(\mathbf{C} - \mathbf{I}\right)\mathbf{M}
\end{aligned}
\tag{2.2.4}
$$

where we define the strain tensor $\mathbf{E} = \frac{1}{2}\left(\mathbf{C} - \mathbf{I}\right)$ and it is called the Lagrangian strain.

A similar approach can be adopted to define the Eulerian strain, which is expressed as $\mathbf{e} = \frac{1}{2}\left(\mathbf{I} - \mathbf{B}\right)$. We also note that the linearized strain tensor is $\epsilon_{ij} = \frac{1}{2}\left(\frac{du_i}{dx_j} + \frac{du_j}{dx_i}\right)$.

2.3 Stress Concepts

To introduce stress we define the traction vector on any surface in a body. Specifically, we define the traction in both configurations as

$$
\underbrace{\mathbf{t} = \mathbf{t}(\mathbf{x}, \mathbf{n})}_{\text{Current configuration}} \quad , \qquad \underbrace{\mathbf{T} = \mathbf{T}(\mathbf{X}, \mathbf{N})}_{\text{reference Configuration}}
\tag{2.3.1}
$$

where $\mathbf{t}$ is called the Cauchy traction vector defined as a force per unit current area and $\mathbf{T}$ is called the first Piola-Kirchhoff traction vector defined as a force per unit reference area.

The stress tensor is postulated by invoking Cauchy's stress theorem which states that there exists a unique second order tensor such that

$$
\mathbf{t} = \boldsymbol{\sigma}\mathbf{n}, \qquad \mathbf{T} = \mathbf{PN}
\tag{2.3.2}
$$

where $\boldsymbol{\sigma}$ is the *Cauchy stress* defined in the current configuration and it's a symmetric tensor, the traction-stress relation in indicial notation is $t_i = \sigma_{ij} n_j$. On the other hand, $\mathbf{P}$ is the *first Piola-Kirchhoff stress* defined as a two-point tensor with one-leg in the reference configuration and the other in the current configuration, the traction-stress relation in indicial notation is $T_i = P_{iA} N_A$. The first Piola-Kirchhoff stress tensor, being a mixed tensor, is synonymous to the deformation gradient $\mathbf{F}$ in nature. Note the proof of the existence of the stress tensor is omitted, it can however be shown by utilizing Cauchy's tetrahedron concept. Additionally, assuming no body moments, the symmetry of the Cauchy stress $\boldsymbol{\sigma} = \boldsymbol{\sigma}^T$ is a direct result of the balance of angular momentum. Note also that the first Piola-Kirchhoff stress is generally not symmetric.

We can obtain relations between the Cauchy stress and the first Piola-Kirchhoff stress where,

$$\mathbf{P} = J\boldsymbol{\sigma}\mathbf{F}^{-T} \quad , \quad P_{iA} = J\sigma_{ij}F_{Aj}^{-1} \tag{2.3.3}$$

and we finally introduce another common stress tensor known as the *second Piola-Kirchhoff stress* $\mathbf{S}$ defined as

$$\mathbf{P} = \mathbf{F}\mathbf{S} \quad , \quad \boldsymbol{\sigma} = \frac{1}{J}\mathbf{F}\mathbf{S}\mathbf{F}^T \tag{2.3.4}$$

we note that $\mathbf{S}$ does not lend itself to a physical interpretation in terms of tractions. None the less, this stress tensor is defined completely in the reference configuration and is useful when defining constitutive equations. This stress tensor is symmetric in nature.

2.4 Balance Equations

In this section the basic balance equations are introduced, with special attention to conservation of mass, balance of linear momentum and balance of angular momentum.

2.4.1 Conservation of Mass

We start by considering conservation of mass, where we assume that the mass of the system remains constant. We therefore, do not consider cases where masses is added or lost from our body. Noting that the mass density $\rho_0(\mathbf{X})$ is defined as mass per reference volume and $\rho(\mathbf{x}, t)$ is mass per current volume, we have

$$m = \int_{\Omega_0} \rho_0(\mathbf{X}) dV = \int_{\Omega} \rho(\mathbf{x}, t) dv = constant > 0 \tag{2.4.1}$$

Since, we have the relationship $dv = J dV$ we can obtain the local form of conservation of mass as

$$\rho_0(\mathbf{X}) = \rho(\mathbf{x}, t) J \tag{2.4.2}$$

2.4.2 Balance of Linear Momentum

We now consider the balance of linear momentum. The linear momentum equation for a portion of a continuum body is simply

$$L(t) = \int_{\Omega} \rho \mathbf{v} dv = \int_{\Omega_0} \rho_0 \mathbf{v} dV \tag{2.4.3}$$

where $\mathbf{v}$ is the velocity vector. The balance of linear momentum then states that the total force acting on the body is equal to the time derivative of the linear momentum, we therefore obtain

$$\dot{L}(t) = \frac{d}{dt} \int_{\Omega} \rho \mathbf{v} dv = \frac{d}{dt} \int_{\Omega_0} \rho_0 \mathbf{v} dV = \mathbf{f} \tag{2.4.4}$$

where $\mathbf{f}$ are the total forces on the continuum body $\mathcal{B}$. The total forces $\mathbf{f}$ are defined as

$$
\begin{aligned}
\mathbf{f} &= \int_{\partial\Omega} \mathbf{t}\,da + \int_{\Omega} \mathbf{b}\,dv \\
&= \int_{\partial\Omega_0} \mathbf{T}\,dA + \int_{\Omega_0} \mathbf{B}\,dV
\end{aligned}
\tag{2.4.5}
$$

with $\mathbf{t}$ and $\mathbf{T}$ being the spatial and reference configuration tractions respectively. Also, $\mathbf{b}$ and $\mathbf{B}$ are the spatial and reference configuration body forces. We can now, with the help of Cauchy's Stress theorem, divergence theorem and Reynolds transport theorem, obtain a local form of the balance of linear momentum. The results for both spatial and reference configuration notation are summarized as

$$
\text{Current Configuration:} \qquad \text{div}\boldsymbol{\sigma} + \mathbf{b} = \rho\dot{\mathbf{v}}
\tag{2.4.6}
$$

$$
\text{Reference Configuration:} \qquad \text{Div}\mathbf{P} + \mathbf{B} = \rho_0\dot{\mathbf{v}}
\tag{2.4.7}
$$

where div and Div refer to the divergence operator with respect to x_i and X_A respectively. These equations are the general equations of motions for a continuum body.

2.4.3 Balance of Angular Momentum

The angular momentum of a portion of a continuum about a fixed point in space is defined as

$$
\mathbf{J} = \int_{\Omega} \mathbf{r} \times \rho\mathbf{v}\,dv = \int_{\Omega_0} \mathbf{r} \times \rho_0\mathbf{v}\,dV
\tag{2.4.8}
$$

where $\mathbf{r}$ is the position vector with respect to the fixed point. The balance of angular momentum equates the time derivative of $\mathbf{J}$ to the total moment about the fixed point as

$$
\dot{\mathbf{J}} = \frac{d}{dt}\int_{\Omega} \mathbf{r} \times \rho\mathbf{v}\,dv = \frac{d}{dt}\int_{\Omega_0} \mathbf{r} \times \rho_0\mathbf{v}\,dV = \mathbf{M}
\tag{2.4.9}
$$

where $\mathbf{M}$ are the sum of moments about a fixed point defined as

$$\mathbf{M} = \int_{\partial\Omega} \mathbf{r} \times \mathbf{t}\,da + \int_{\Omega} \mathbf{r} \times \mathbf{b}\,dv$$
$$= \int_{\partial\Omega_0} \mathbf{r} \times \mathbf{T}\,dA + \int_{\Omega_0} \mathbf{r} \times \mathbf{B}\,dV \qquad (2.4.10)$$

We can reduce the balance of angular momentum equation by considering Cauchy's Theorem and divergence theorem to a statement on the symmetry of the Cauchy stress, where $\boldsymbol{\sigma} = \boldsymbol{\sigma}^T$. We note again that the first Piola-Kirchhoff stress is generally not symmetric.

2.5 Constitutive Relations

In this section a brief overview of both linear and nonlinear constitutive equations are presented. We consider only elastic materials, which are materials whose deformation depends only on the current state of stress without any concern for the deformation history. These are known as path independent materials. A special type of elastic material is a hyperelastic material, in which a free energy function $W = W(\mathbf{F})$ is postulated to exist and is defined as energy per unit reference volume. This assumption can be formulated from a balance of energy perspective[20]. Another characteristic of hyperelastic materials is that the work done on a closed system is zero. W is commonly referred to as a strain-energy function. For an in-depth review of hyperelastic materials the reader is referred to Holzapfel [20] and Ogden [21]. We note that the constitutive relation between stress and deformationa in hyperelastic materials is defined as

$$\mathbf{P} = \frac{\partial W(\mathbf{F})}{\partial \mathbf{F}} \qquad (2.5.1)$$

We can write the strain energy function in terms of different parameters. For instance, as a result of objectivity requirements we have $W(\mathbf{F}) = W(\mathbf{U})$. And we can also write

$$W(\mathbf{F}) = \hat{W}(\mathbf{C}) = \tilde{W}(\mathbf{E}) \qquad (2.5.2)$$

note that the above function are different, however for simplicity of notation we will always utilize $W(\cdot)$ as the function name, regardless of the parameters it depends on. By using the chain rule we can obtain an alternate expression for the stress such that

$$\mathbf{P} = \frac{\partial W(\mathbf{F})}{\partial \mathbf{F}} = 2\mathbf{F}\frac{\partial W(\mathbf{C})}{\partial \mathbf{C}} \tag{2.5.3}$$

Recalling that $\mathbf{P} = \mathbf{FS}$, we have that

$$\mathbf{S} = 2\frac{\partial W(\mathbf{C})}{\partial \mathbf{C}} = \frac{\partial W(\mathbf{E})}{\partial \mathbf{E}} \tag{2.5.4}$$

We also note that as a result of hyperelasticity we can define a 4th-order elasticity tensors as derivatives of the strain energy function. We focus only on obtaining the tangent for the second Piola-Kirchhoff stress. Hence, we have

$$\mathbb{C}_{ABCD} = 2\frac{\partial S_{AB}}{\partial C_{CD}} = 4\frac{\partial^2 W(\mathbf{C})}{\partial C_{AB}\partial C_{CD}} \tag{2.5.5}$$

This gives us the material tangent and it's an important quantity when dealing with non-linear finite elements. We note this is not the total tangent, which is obtained from $\frac{\partial \mathbf{P}}{\partial \mathbf{F}}$. Since, we are concerned with fiber composites special focus will be placed on orthotropic materials.

2.5.1 Linear Constitutive Relations

For linear elasticity, the general form of the strain energy function is $W = \frac{1}{2}\boldsymbol{\epsilon} \cdot \mathbb{C}\boldsymbol{\epsilon}$, where $\boldsymbol{\epsilon}$ is the small strain and $\mathbb{C}$ is the elasticity tensor for any elastic material. Recall, that small strain is defined as $\boldsymbol{\epsilon} = \frac{1}{2}\left(\frac{du_i}{dx_j} + \frac{du_j}{dx_i}\right)$. The stress is given as,

$$\boldsymbol{\sigma} = \frac{dW}{d\boldsymbol{\epsilon}} = \mathbb{C}\boldsymbol{\epsilon} \tag{2.5.6}$$

Since our interest is in unidirectional fiber composites we can specialize the form of the elasticity tensor to transversely isotropic materials, which is a subset of orthotropic materials. Figure. 2.2 shows a configuration of fibers in a matrix, the fibers are aligned

along the E_1 direction. A more general case can easily be considered.

When specializing the elasticity tensor to transverse isotropy we obtain the form shown in Eqn. 2.5.7 using Voigt notation [22].

$$
\begin{bmatrix} \sigma_{11} \\ \sigma_{22} \\ \sigma_{33} \\ \sigma_{23} \\ \sigma_{31} \\ \sigma_{12} \end{bmatrix} = \begin{bmatrix} C_{11} & C_{12} & C_{12} & 0 & 0 & 0 \\ C_{12} & C_{22} & C_{23} & 0 & 0 & 0 \\ C_{12} & C_{23} & C_{22} & 0 & 0 & 0 \\ 0 & 0 & 0 & \frac{1}{2}(C_{22} - C_{23}) & 0 & 0 \\ 0 & 0 & 0 & 0 & C_{66} & 0 \\ 0 & 0 & 0 & 0 & 0 & C_{66} \end{bmatrix} \begin{bmatrix} \epsilon_{11} \\ \epsilon_{22} \\ \epsilon_{33} \\ 2\epsilon_{23} \\ 2\epsilon_{31} \\ 2\epsilon_{12} \end{bmatrix}
$$

$$
= \begin{bmatrix} \lambda + 2\alpha + 4\mu_L - 2\mu_T + \beta & \lambda + \alpha & \lambda + \alpha & 0 & 0 & 0 \\ \lambda + \alpha & \lambda + 2\mu_T & \lambda & 0 & 0 & 0 \\ \lambda + \alpha & \lambda & \lambda + 2\mu_T & 0 & 0 & 0 \\ 0 & 0 & 0 & \mu_T & 0 & 0 \\ 0 & 0 & 0 & 0 & \mu_L & 0 \\ 0 & 0 & 0 & 0 & 0 & \mu_L \end{bmatrix} \begin{bmatrix} \epsilon_{11} \\ \epsilon_{22} \\ \epsilon_{33} \\ 2\epsilon_{23} \\ 2\epsilon_{31} \\ 2\epsilon_{12} \end{bmatrix}
$$

$$(2.5.7)$$

Note that μ_L and μ_T are the shear moduli along the fiber direction and the transverse to the fiber direction respectively. Additionally, α, λ and β are elastic constants. Their physical meaning is not very obvious, however, they can be related to the extension moduli and poissons ratio. To obtain the engineering moduli $E_{11}, E_{22}, \nu_{12}, \nu_{23}, \mu_{12}$ we must utilize the elastic compliance matrix $\mathbb{S}$, where $\mathbb{S} = \mathbb{C}^{-1}$. This implies the relationship $\boldsymbol{\epsilon} = \mathbb{S}\boldsymbol{\sigma}$. Using this relationship and conducting experiments such that $\boldsymbol{\sigma}_{11} \neq 0$ and the rest of the stress components are zero, we obtain the relations

$$\epsilon_{11} = S_{11}\sigma_{11}$$
$$\epsilon_{22} = S_{12}\sigma_{11} \qquad\qquad (2.5.8)$$
$$\epsilon_{33} = S_{12}\sigma_{11}$$

It is evident that $S_{11} = 1/E_{11}$ and since $\epsilon_{11} = -\nu_{12}\epsilon_{22}$ we have $S_{12} = -\nu_{12}/E_{11}$. Conducting
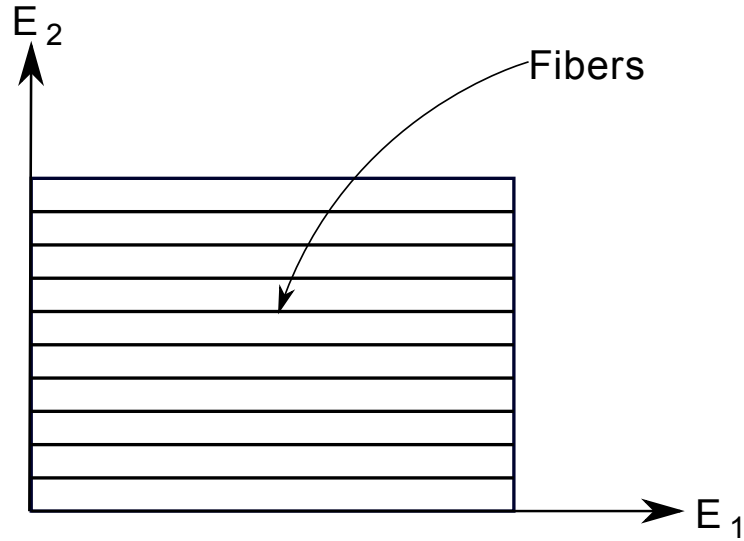
Figure 2.2: Schematics of fiber composite

similar experiments with σ_{22}, σ_{33}, etc we can obtain the form [4]

$$\mathbb{S} = \begin{bmatrix} \frac{1}{E_{11}} & -\frac{\nu_{21}}{E_{22}} & -\frac{\nu_{21}}{E_{22}} & 0 & 0 & 0 \\ -\frac{\nu_{12}}{E_{11}} & \frac{1}{E_{22}} & -\frac{\nu_{23}}{E_{22}} & 0 & 0 & 0 \\ -\frac{\nu_{12}}{E_{11}} & -\frac{\nu_{23}}{E_{22}} & \frac{1}{E_{22}} & 0 & 0 & 0 \\ 0 & 0 & 0 & \frac{1}{\mu_{23}} & 0 & 0 \\ 0 & 0 & 0 & 0 & \frac{1}{\mu_{12}} & 0 \\ 0 & 0 & 0 & 0 & 0 & \frac{1}{\mu_{12}} \end{bmatrix} \tag{2.5.9}$$

We can explicitly write the relationship between the engineering moduli and the components of the elasticity tensor. This is done by taking the inverse of $\mathbb{C}$ and relating the components to the explicit form of $\mathbb{S}$. We therefore have,

$$
\begin{aligned}
E_{11} &= \frac{-2C_{12}^2 + C_{11}(C_{22} + C_{23})}{C_{22} + C_{23}} \\
E_{22} &= -\frac{(C_{22} - C_{23})\left(-2C_{12}^2 + C_{11}(C_{22} + C_{23})\right)}{C_{12}^2 - C_{11}C_{22}} \\
\nu_{12} &= \frac{C_{12}(C_{22} - C_{23})}{C_{11}C_{22} - C_{12}^2} \\
\nu_{23} &= \frac{C_{11}C_{23} - C_{12}^2}{C_{11}C_{22} - C_{12}^2} \\
\mu_{12} &= \frac{1}{C_{66}} \\
\mu_{23} &= \frac{E_{22}}{2(1 + \nu_{23})}
\end{aligned}
\tag{2.5.10}
$$

these relations will used to determine the specific engineering moduli from the elasticity tensor that's obtained from FEM simulations.

2.5.2 Nonlinear Constitutive Relations

There a number of strain energy functions [21] that can be used in nonlinear elasticity. However, our focus will be on the simplest form, which is known as the Kirchhoff-St.Venant material model. This is an extension of Hooke's law as identified for linear elasticity. The strain energy function is defined as

$$
W(\mathbf{E}) = \frac{1}{2}\mathbf{E} : \mathbb{C} : \mathbf{E}
\tag{2.5.11}
$$

where $\mathbf{E}$ is the Lagrangian strain and $\mathbb{C}$ is the material elasticity tensor. Therefore, the second Piola-Kirchhoff stress is then defined as

$$
\mathbf{S} = \frac{\partial W}{\partial \mathbf{E}} = \mathbb{C} : \mathbf{E}
\tag{2.5.12}
$$

we make note, that this strain energy function does not satisfy the basic so called growth conditions [20]. Specifically, as $\det(\mathbf{F}) \to 0$ the stress goes to zero. This is physically unrealistic. Nonetheless, since for our interest J will generally be close to 1 this material

model can still be used and is employed for all ensuing analysis

Chapter 3

Finite Element Method

3.1 Introdution

There are two main approaches to analyze finite deformation problems using the finite element method. The first is what is known as the total lagrangian methodology and the second is known as the updated lagrangian. The adopted method in this chapter is the total lagrangian and will be briefly introduced. For a full account of developing the finite element method for both linear and non-linear problems the reader is referred to Hughes and Pister. [23], Hughes. [24], Zienkiewicz and Taylor.[25] and Belytshko et al. [26].

3.2 Total Lagrangian Formulation

This method relies on executing all calculations on the reference configuration. As such, the boundary value problem is solved in the reference configuration. The strong form is defined with reference to Chapter 2 as

$$\text{Div}\mathbf{P} + \rho_0\mathbf{b} = \rho_0\ddot{\mathbf{x}}$$

$$\mathbf{u} = \hat{\mathbf{u}} \text{ on } \Gamma_{0,\mathbf{u}}, \qquad \mathbf{T} = \hat{\mathbf{T}} \text{ on } \Gamma_{0,\mathbf{T}} \tag{3.2.1}$$

where $\Gamma_{0,\mathbf{u}} \cup \Gamma_{0,\mathbf{T}} = \Gamma$ is the boundary of the domain. Also Div refers to the divergence with respect to the reference configuration(i.e $\text{Div}\mathbf{P} = \frac{\partial P_{iA}}{\partial X_A}\mathbf{e}_i$). As noted previously, $\mathbf{P}$ is the first Piola Kirchhoff stress and is related to the Cauchy stress as $\boldsymbol{\sigma} = J^{-1}\mathbf{P}\mathbf{F}^T$.

An additional stress description is the second Piola Kirchhoff stress defined previously as $\mathbf{S} = \mathbf{F}^{-1}\mathbf{P}$.

Considering the static case, we begin by deriving the weak form of the boundary value problem defined in Eqn. 3.2.1. This is achieved by multiplying Eqn. 3.2.1 by a test function $\mathbf{v}$ and integrating. Hence,

$$\int_{\Omega_0} \mathbf{v} \cdot (\text{Div}\mathbf{P} + \rho_0 \mathbf{b})\, d\Omega_0 = 0, \qquad \forall \mathbf{v} \tag{3.2.2}$$

We consider the first term of the integral equation and rewrite it utilizing the divergence theorem, we obtain after with some manipulations that

$$
\begin{aligned}
\int_{\Omega_0} \mathbf{v} \cdot \text{Div}\mathbf{P}\, d\Omega_0 &= \int_{\Omega_0} \left(\text{Div}(\mathbf{P}^T \mathbf{v}) - \text{Grad}\mathbf{v} : \mathbf{P}^T \right) d\Omega_0 \\
&= \int_{\Omega_0} \left(\nabla_{\mathbf{X}} \cdot (\mathbf{P}^T \mathbf{v}) - \nabla_{\mathbf{X}} \mathbf{v} : \mathbf{P}^T \right) d\Omega_0 \\
&= \int_{\Gamma_0} (\mathbf{P}^T \mathbf{v}) \cdot \mathbf{N}\, d\Gamma_0 - \int_{\Omega_0} \nabla_{\mathbf{X}} \mathbf{v} : \mathbf{P}^T \mathbf{v}\, d\Omega_0 \\
&= \int_{\Gamma_0} \mathbf{v} \cdot \mathbf{P}\mathbf{N}\, d\Gamma_0 - \int_{\Omega_0} \nabla_{\mathbf{X}} \mathbf{v} : \mathbf{P}^T d\Omega_0 \\
&= \int_{\Gamma_0} \mathbf{v} \cdot \mathbf{T}\, d\Gamma_0 - \int_{\Omega_0} \nabla_{\mathbf{X}} \mathbf{v} : \mathbf{P}^T d\Omega_0
\end{aligned} \tag{3.2.3}
$$

where $\mathbf{T}$ is the Piola traction and $\mathbf{N}$ is the surface normal in the reference configuration. Plugging Eqn.3.2.3 into Eqn.3.2.2 we obtain the following result for the weak form

$$\int_{\Omega_0} \nabla_{\mathbf{X}} \mathbf{v} : \mathbf{P}^T d\Omega_0 = \int_{\Gamma_0} \mathbf{v} \cdot \mathbf{T}\, d\Gamma_0 + \int_{\Omega_0} \rho_0 \mathbf{v} \cdot \mathbf{b}\, d\Omega_0 \tag{3.2.4}$$

which must hold for all $\mathbf{v}$ and $\mathbf{v}|_{\Gamma_{0,\mathbf{u}}} = 0$. We note that in the so called weak form we no longer require the differentiability of the stress. Hence, we have weakened the smoothness of the field when compared to the strong form.

We proceed by considering hyperelastic materials which, as discussed in Chapter 2 are defined by assuming the existence of a Helmholtz free-energy function $W(\mathbf{F})$, defined per unit reference volume. In addition from Chapter 2 recall that the second Piola-Kirchhoff stress is defined as

$$\mathbf{S} = \frac{\partial W(\mathbf{E})}{\partial \mathbf{E}} \tag{3.2.5}$$

where $\mathbf{E} = \frac{1}{2}(\mathbf{C} - \mathbf{I})$ and $\mathbf{C} = \mathbf{F}^T\mathbf{F}$.

The equation we are trying to solve are nonlinear, since this is hard we resort to approximating them. Therefore, we linearize our equations of motion and utilize Newton's method to obtain a solution to the original problem. The mathematical theory for linearization as applied to the finite element method was first introduced by Hughes and Pister [23], and is the subject of the next section.

3.2.1   Linearization of the Equations of Motion

For simplicity, we start off by assuming that the tractions and body forces are not functions of the displacement. This means that no follower forces can be considered, to include these types of effects the traction would have to be linearized. Linearization is done through the Gateaux derivative, which is defined as

$$D_{\Delta\mathbf{u}}[\Psi(\mathbf{u})] = \frac{d}{dw}\Psi(\mathbf{u} + w\Delta\mathbf{u})|_{w=0} \tag{3.2.6}$$

this states that we are taking the derivative of Ψ with respect to $\mathbf{u}$ and in the direction of $\Delta\mathbf{u}$. The derivative clearly depends on the direction, and is a generalization of the directional derivative. To linearize the weak form found in Eqn. 3.2.4 we take the Gateaux derivative of the internal energy component $W_{int} = \int_{\Omega_0} \nabla_{\mathbf{X}}\mathbf{v} : \mathbf{P}^T d\Omega_0$ with respect to the displacement $\mathbf{u}$ and in the direction $\Delta\mathbf{u}$. Notice, since we are assuming that the tractions and body forces do not depend on the displacement, we do not need to linearize them. Hence we have the following statement

$$\begin{aligned}
D_{\Delta\mathbf{u}}[W_{int}(\mathbf{u})] &= D_{\Delta\mathbf{u}}\left[\int_{\Omega_0} \nabla_{\mathbf{X}}\mathbf{v} : \mathbf{P}^T d\Omega_0\right] \\
&= D_{\Delta\mathbf{u}}\left[\int_{\Omega_0} \nabla_{\mathbf{X}}\mathbf{v} : \mathbf{S}\mathbf{F}^T d\Omega_0\right] \\
&= \int_{\Omega_0} \nabla_{\mathbf{X}}\mathbf{v} : D_{\Delta\mathbf{u}}[\mathbf{S}\mathbf{F}^T] d\Omega_0 \\
&= \int_{\Omega_0} \underbrace{\nabla_{\mathbf{X}}\mathbf{v} : D_{\Delta\mathbf{u}}[\mathbf{S}(\mathbf{E}(\mathbf{u}))]\mathbf{F}^T}_{K^{mat}=\text{MATERIAL TANGENT}} + \underbrace{\nabla_{\mathbf{X}}\mathbf{v} : \mathbf{S}D_{\Delta\mathbf{u}}[\mathbf{F}(\mathbf{u})^T]}_{K^{geo}=\text{ GEOMETRIC TANGENT}} \quad d\Omega_0
\end{aligned} \tag{3.2.7}$$

We will consider each component in Eqn. 3.2.7 individually. Starting with the material tangent component we make use of the trace property that $\text{tr}(ABC) = \text{tr}(CAB)$, therefore allowing us to write

$$
\begin{aligned}
K^{mat} &= \int_{\Omega_0} \text{tr}(\nabla_{\mathbf{X}}\mathbf{v} D_{\Delta\mathbf{u}}[\mathbf{S}(\mathbf{E}(\mathbf{u}))]\mathbf{F}^T)d\Omega_0 \\
&= \int_{\Omega_0} \text{tr}(\mathbf{F}^T\nabla_{\mathbf{X}}\mathbf{v} D_{\Delta\mathbf{u}}[\mathbf{S}(\mathbf{E}(\mathbf{u}))])d\Omega_0 \\
&= \int_{\Omega_0} \mathbf{F}^T\nabla_{\mathbf{X}}\mathbf{v} : D_{\Delta\mathbf{u}}[\mathbf{S}(\mathbf{E}(\mathbf{u}))]d\Omega_0
\end{aligned}
\tag{3.2.8}
$$

Since $\mathbf{S} = \mathbf{S}(\mathbf{E}(\mathbf{u}))$ we can utilize the chain rule to obtain that $D_{\Delta\mathbf{u}}[\mathbf{S}(\mathbf{E}(\mathbf{u}))] = \frac{\partial \mathbf{S}}{\partial \mathbf{E}}D_{\Delta\mathbf{u}}[\mathbf{E}(\mathbf{u})]$, and plug this result back into Eqn 3.2.8. Recall that $\frac{\partial \mathbf{S}}{\partial \mathbf{E}} = \mathbb{C}$, which are the material properties.

We now proceed with the linearization of both the Green-Lagrange strain and the deformation gradient. We start with the deformation gradient defined as $\mathbf{F} = \frac{d\mathbf{x}}{d\mathbf{X}} = \frac{d\mathbf{u}}{d\mathbf{X}} + \mathbf{I}$ and its linearization is

$$
\begin{aligned}
D_{\Delta\mathbf{u}}F(\mathbf{u}) &= \frac{d}{dw}F(\mathbf{u} + w\Delta\mathbf{u})|_{w=0} \\
&= \frac{d}{dw}\left(\frac{d(\mathbf{u} + w\Delta\mathbf{u})}{d\mathbf{X}} + \mathbf{I}\right)|_{w=0} \\
&= \frac{d}{dw}\left(\mathbf{H} + w\frac{d\Delta\mathbf{u}}{d\mathbf{X}}\right)|_{w=0} \\
&= \frac{d\Delta\mathbf{u}}{d\mathbf{X}} = \nabla_{\mathbf{X}}\Delta\mathbf{u}
\end{aligned}
\tag{3.2.9}
$$

Now we consider the Green-Lagrange strain defined as $\mathbf{E} = \frac{1}{2}\left(\mathbf{F}^T\mathbf{F} - \mathbf{I}\right)$ and its linearization is

$$
\begin{aligned}
D_{\Delta u}[\mathbf{E}(\mathbf{u})] &= \frac{d}{dw}\mathbf{E}(\mathbf{u}+w\mathbf{\Delta u})|_{w=0} \\
&= \frac{1}{2}\frac{d}{dw}(\mathbf{F}(\mathbf{u}+\mathbf{w\Delta u})^{T}\mathbf{F}(\mathbf{u}+\mathbf{w\Delta u})-\mathbf{I})|_{w=0} \\
&= \frac{1}{2}\frac{d}{dw}\left[\left(\frac{d(\mathbf{u}+w\Delta\mathbf{u})}{d\mathbf{X}}+\mathbf{I}\right)^{T}\left(\frac{d(\mathbf{u}+w\Delta\mathbf{u})}{d\mathbf{X}}+\mathbf{I}\right)+\mathbf{I}\right] \\
&= \frac{1}{2}\left[\left(\frac{d\mathbf{u}}{d\mathbf{X}}^{T}+\mathbf{I}\right)\frac{d\Delta\mathbf{u}}{d\mathbf{X}}+\left(\frac{d\Delta\mathbf{u}}{d\mathbf{X}}\right)^{T}\left(\frac{d\mathbf{u}}{d\mathbf{X}}+\mathbf{I}\right)\right] \\
&= \frac{1}{2}\left[\mathbf{F}^{T}\nabla_{\mathbf{X}}\Delta\mathbf{u}+(\nabla_{\mathbf{X}}\Delta\mathbf{u})^{T}\mathbf{F}\right]
\end{aligned} \tag{3.2.10}
$$

With these results we can expand the complete linearized form of the internal energy, continuing on from Eqn. 3.2.8 and plugging in the result from Eqn. 3.2.10 we have the material tangent expressed as

$$
\begin{aligned}
K^{mat} &= \int_{\Omega_0}\mathbf{F}^{T}\nabla_{\mathbf{X}}\mathbf{v}:\frac{\partial\mathbf{S}}{\partial\mathbf{E}}D_{\Delta\mathbf{u}}[\mathbf{E}(\mathbf{u})]d\Omega_0 \\
&= \frac{1}{2}\int_{\Omega_0}\mathbf{F}^{T}\nabla_{\mathbf{X}}\mathbf{v}:\frac{\partial\mathbf{S}}{\partial\mathbf{E}}\left[\mathbf{F}^{T}\nabla_{\mathbf{X}}\Delta\mathbf{u}+(\nabla_{\mathbf{X}}\Delta\mathbf{u})^{T}\mathbf{F}\right]d\Omega_0 \\
&= \int_{\Omega_0}\mathbf{F}^{T}\nabla_{\mathbf{X}}\mathbf{v}:\frac{\partial\mathbf{S}}{\partial\mathbf{E}}sym[\mathbf{F}^{T}\nabla_{\mathbf{X}}\Delta\mathbf{u}]d\Omega_0 \\
&= \int_{\Omega_0}\mathbf{F}^{T}\nabla_{\mathbf{X}}\mathbf{v}:\frac{\partial\mathbf{S}}{\partial\mathbf{E}}[\mathbf{F}^{T}\nabla_{\mathbf{X}}\Delta\mathbf{u}]d\Omega_0
\end{aligned} \tag{3.2.11}
$$

Now we consider the geometric component of the stiffness matrix found in Eqn. 3.2.7 and plug in the result from Eqn. 3.2.9 to obtain

$$
\begin{aligned}
K^{geo} &= \int_{\Omega_0}\nabla_{\mathbf{X}}\mathbf{v}:\mathbf{S}D_{\Delta u}[\mathbf{F}(\mathbf{u})^{T}]d\Omega_0 \\
&= \int_{\Omega_0}\nabla_{\mathbf{X}}\mathbf{v}:\mathbf{S}\left(\frac{\partial\Delta\mathbf{u}}{\partial\mathbf{X}}\right)^{T}d\Omega_0 \\
&= \int_{\Omega_0}\nabla_{\mathbf{X}}\mathbf{v}:\mathbf{S}\left(\nabla_{\mathbf{X}}\Delta\mathbf{u}\right)^{T}d\Omega_0
\end{aligned} \tag{3.2.12}
$$

So our final linearized form of the balance of linear momentum equations are

$$D_{\Delta u}[W_{int}] = \int_{\Omega_0} \mathbf{F}^T \nabla_{\mathbf{X}} \mathbf{v} : \frac{\partial \mathbf{S}}{\partial \mathbf{E}} [\mathbf{F}^T \nabla_{\mathbf{X}} \Delta \mathbf{u}] d\Omega_0 + \int_{\Omega_0} \nabla_{\mathbf{X}} \mathbf{v} : \mathbf{S} (\nabla_{\mathbf{X}} \Delta \mathbf{u})^T d\Omega_0 \quad (3.2.13)$$

3.2.2 Finite Element Discretization

In this section the finite element discretization process is introduced. The domain Ω_0 of a continuum is discretized into smaller finite elements $\Omega_{0,e}$, where $\Omega_0 = \cup \Omega_{0e}$. This is illustrated in Figure. 3.1
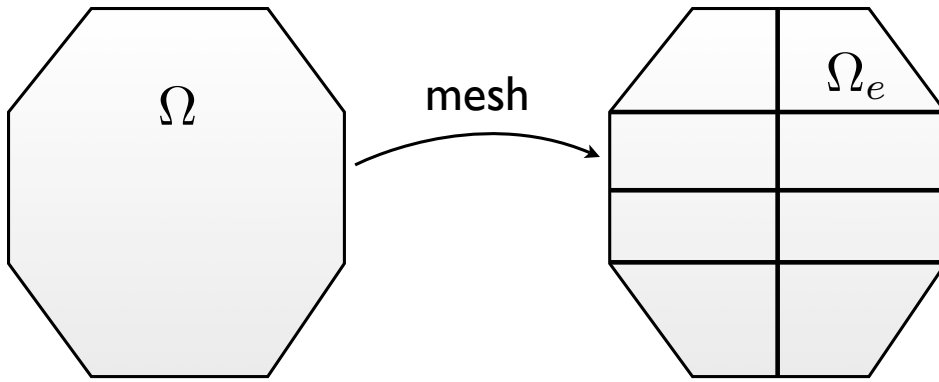
Figure 3.1: The figure shows the finite element discretization. The left image shows the global domain Ω_0 and the left part shows the mesh of the global domain with element $\Omega_{0,e}$

The motion $\mathbf{x}(\mathbf{X}, t)$ is approximated in a finite element as

$$\mathbf{x} = \mathbf{X}_I N(\mathbf{X})_I \quad (3.2.14)$$

where N_I are the shape functions, or generally speaking interpolation functions, and $\mathbf{X}_I$ are the nodal position vector at node I and summation over I is implied. We can also approximate the test function as

$$\mathbf{v} = \mathbf{b}_I N(\mathbf{X})_I$$
$$v_i = b_{iI} N_I \quad (3.2.15)$$

where b_{iI} are nodal values. From our linearized form, for simplicity of notation replace $\Delta \mathbf{u}$

with **u** and we have the following approximation for the unknown variable

$$\mathbf{u} = \mathbf{a}_I N(\mathbf{X})_I$$
$$u_i = a_{iI} N_I$$

(3.2.16)

again a_{iI} are the nodal values that we need to solve for. With this in mind we can approximate $\nabla_X \mathbf{v}$ and $\nabla_X \mathbf{u}$ in terms of the shape functions as

$$\nabla_X \mathbf{u} = \frac{\partial u_i}{\partial X_A} = \frac{\partial N_I a_{iI}}{\partial X_A}$$
$$= \frac{\partial N_I}{\partial X_A} a_{iI}$$

(3.2.17)

the same expression is obtained for the gradient of the test function **v**.

We start by considering the linearized form of W_{int} found in Eqn. 3.2.13 and plugging in the finite element approximations. In indicial notation Eqn. 3.2.13 becomes

$$D_{\Delta u}[W_{int}] = \int_{\Omega_0} F_{iA} \frac{\partial v_i}{\partial X_B} \frac{\partial S_{AB}}{\partial E_{CD}} F_{jC} \frac{\partial u_j}{\partial X_D} d\Omega_0 + \int_{\Omega_0} \frac{\partial v_i}{\partial X_A} S_{AB} \frac{\partial u_i}{\partial X_B} d\Omega_0$$

(3.2.18)

plugging in the approximations we obtain

$$D_{\Delta u}[W_{int}] = \int_{\Omega_0} F_{iA} \frac{\partial N_I}{\partial X_B} b_{iI} \frac{\partial S_{AB}}{\partial E_{CD}} F_{jC} \frac{\partial N_J}{\partial X_D} a_{jJ} d\Omega_0$$
$$+ \int_{\Omega_0} \frac{\partial N_I}{\partial X_A} b_{iI} S_{AB} \frac{\partial N_J}{\partial X_B} a_{iJ} d\Omega_0$$

(3.2.19)

then factoring out b_{iI} and a_{jJ} as common factors we get

$$D_{\Delta u}[W_{int}] = b_{iI} \left[\int_{\Omega_0} F_{iA} \frac{\partial N_I}{\partial X_B} \frac{\partial S_{AB}}{\partial E_{CD}} F_{jC} \frac{\partial N_J}{\partial X_D} d\Omega_0 \right.$$
$$\left. + \delta_{ij} \int_{\Omega_0} \frac{\partial N_I}{\partial X_A} S_{AB} \frac{\partial N_J}{\partial X_B} d\Omega_0 \right] a_{jJ}$$

(3.2.20)

Now consider the finite element approximation of the body force term and the

applied traction term to get

$$
\int_{\Gamma_0} \mathbf{v}.\mathbf{T}d\Gamma_0 + \int_{\Omega_0} \rho_0 \mathbf{v}.\mathbf{f}d\Omega_0 = \int_{\Gamma_0} v_i T_i d\Gamma_0 + \int_{\Omega_0} \rho_0 v_i f_i d\Omega_0
$$

$$
= \int_{\Gamma_0} N_I b_{iI} T_i d\Gamma_0 + \int_{\Omega_0} \rho_0 N_I b_{iI} f_i d\Omega_0 \qquad (3.2.21)
$$

$$
= b_{iI} \left[\int_{\Gamma_0} N_I T_i d\Gamma_0 + \int_{\Omega_0} \rho_0 N_I f_i d\Omega_0 \right]
$$

Lastly, we need to approximate the non-linearized internal energy and we have that

$$
W_{int} = \int_{\Omega_0} \nabla_\mathbf{X} \mathbf{v} : \mathbf{P}^T d\Omega_0 = \int_{\Omega_0} \mathbf{F}^T \nabla_\mathbf{X} \mathbf{v} : \mathbf{S} d\Omega_0
$$

$$
= \int_{\Omega_0} F_{iA} \frac{\partial v_i}{\partial X_B} S_{AB} d\Omega_0
$$

$$
= \int_{\Omega_0} F_{iA} \frac{\partial N_I}{\partial X_B} b_{iI} S_{AB} d\Omega_0 \qquad (3.2.22)
$$

$$
= b_{iI} \left[\int_{\Omega_0} F_{iA} \frac{\partial N_I}{\partial X_B} S_{AB} d\Omega_0 \right]
$$

Keeping in mind Eqn. 3.2.4 we have from Eqn. 3.2.21 and Eqn. 3.2.22 that

$$
b_{iI} \left[\int_{\Omega_0} F_{iA} \frac{\partial N_I}{\partial X_B} S_{AB} d\Omega_0 - \int_{\Gamma_0} N_I T_i d\Gamma_0 + \int_{\Omega_0} \rho_0 N_I f_i d\Omega_0 \right] = 0 \qquad (3.2.23)
$$

and since Eqn. 3.2.4 is true $\forall \mathbf{v}$ and therefore b_{iI} are arbitrary we have that

$$
\int_{\Omega_0} F_{iA} \frac{\partial N_I}{\partial X_B} S_{AB} d\Omega_0 - \int_{\Gamma_0} N_I T_i d\Gamma_0 + \int_{\Omega_0} \rho_0 N_I f_i d\Omega_0 = 0 \qquad (3.2.24)
$$

this in turn allows us to neglect the b_{iI} from the linearized form of the internal energy and hence we have what are known as the internal forces,

$$
\mathbf{f}_{int} = \left[\int_{\Omega_0} F_{iA} \frac{\partial N_I}{\partial X_B} \frac{\partial S_{AB}}{\partial E_{CD}} F_{jC} \frac{\partial N_J}{\partial X_D} d\Omega_0 + \delta_{ij} \int_{\Omega_0} \frac{\partial N_I}{\partial X_A} S_{AB} \frac{\partial N_J}{\partial X_B} d\Omega_0 \right] a_{jJ} \qquad (3.2.25)
$$

we can proceed to use these approximation for an iterative procedure of the Newton type.

3.2.3 Newton's Method

Newton's method is commonly used to solve a set of non-linear equations, similar to the ones obtained from the balance of linear momentum defined in Eqn. 3.2.4. The general statement for solving a nonlinear function $\boldsymbol{\psi} = 0$ according to Newton's method is

$$\boldsymbol{\psi}^{k+1} = \boldsymbol{\psi}^k + \frac{\partial \boldsymbol{\psi}}{\partial \mathbf{u}}\Big|^k d\mathbf{u}^k = 0 \tag{3.2.26}$$

where k is the iteration counter and the tangent stiffness is defined as $\mathbf{K}_T = -\frac{\partial \boldsymbol{\psi}}{\partial \mathbf{u}}$, we obtain that the general algorithm

$$\mathbf{K}_T^k d\mathbf{u}^k = \boldsymbol{\psi}^k \tag{3.2.27}$$

and $\mathbf{u}^{k+1} = \mathbf{u}^k + d\mathbf{u}^k$. For the set of equations from the finite element discretization, our $\boldsymbol{\psi}$ function is

$$\boldsymbol{\psi} = \int_{\Omega_0} F_{iA} \frac{\partial N_I}{\partial X_B} S_{AB} d\Omega_0 - \int_{\Gamma_0} N_I T_i d\Gamma_0 + \int_{\Omega_0} \rho_0 N_I f_i d\Omega_0 = 0 \tag{3.2.28}$$

and the tangent stiffness is then

$$\mathbf{K}_T = \underbrace{\int_{\Omega_0} F_{iA} \frac{\partial N_I}{\partial X_A} \frac{\partial S_{AB}}{\partial E_{CD}} F_{jC} \frac{\partial N_J}{\partial X_D} d\Omega_0}_{\mathbf{K}^{mat}} + \underbrace{\delta_{ij} \int_{\Omega_0} \frac{\partial N_I}{\partial X_A} S_{AB} \frac{\partial N_J}{\partial X_B} d\Omega_0}_{\mathbf{K}^{geo}} \tag{3.2.29}$$

and plugging everything into Eqn. 3.2.26, we obtain the following

$$\int_{\Omega_0} F_{iA}^k \frac{\partial N_I}{\partial X_B} S_{AB}^k d\Omega_0 - \int_{\Gamma_0} N_I T_i^k d\Gamma_0 + \int_{\Omega_0} \rho_0 N_I f_i^k d\Omega_0 =$$
$$\left[\int_{\Omega_0} F_{iA}^k \frac{\partial N_I}{\partial X_A} \frac{\partial S_{AB}^k}{\partial E_{CD}^k} F_{jC}^k \frac{\partial N_J}{\partial X_D} d\Omega_0 + \delta_{ij} \int_{\Omega_0} \frac{\partial N_I}{\partial X_A} S_{AB}^k \frac{\partial N_J}{\partial X_B} d\Omega_0 \right] du_{jJ}^k \tag{3.2.30}$$

which allows us to solve for the displacement increment du_{jJ}^k.

3.2.4 Isoparametric Elements

We now explicity identify the shape function $N(\mathbf{X})_I$ by defining a master element over which all calculations are conducted. This makes the process systematic. We express $N(\mathbf{X})_I = N(\mathbf{X}(\boldsymbol{\zeta})_I = \hat{N}(\boldsymbol{\zeta})_I$, with $\boldsymbol{\zeta}$ being a local coordinate system of the master element. A pictorial description is shown in Figure. 3.2
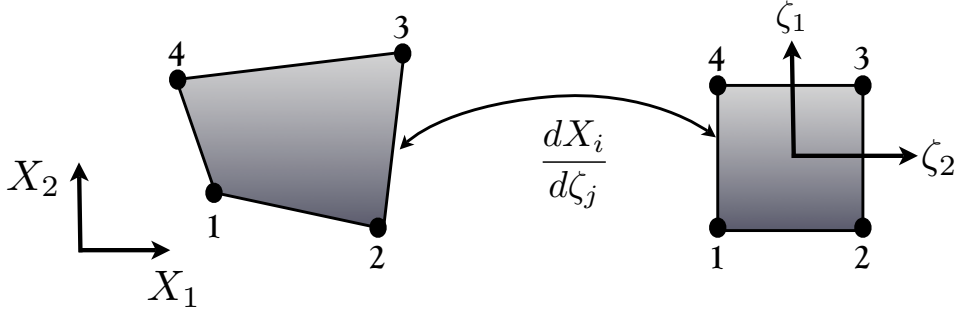
Figure 3.2: Isoparametric mapping in two dimensions for a 4 node quadrilaterial. The left part shows the true mesh, while the right part shows the master element over which all calculations are conducted. The two are related through $\frac{dX_i}{d\zeta_j}$, which is a deformation gradient

An element is called isoparametric, if the shape functions for interpolating the position vectors $\mathbf{X}$ is the same as that for interpolating $\mathbf{u}$. We will limit our discussion to these types of elements. Note that $d\mathbf{X} = \tilde{\mathbf{F}}d\boldsymbol{\zeta}$, with $\tilde{\mathbf{F}} = \frac{dX_A}{d\zeta_j}$ being the mapping from the master element to the reference mesh.

The master element shape functions form a nodal basis. For a 8 nodded three dimensional brick element we can construct the following shape functions

$$
\begin{aligned}
&N_1 = \frac{1}{8}(1+\zeta_1)(1-\zeta_2)(1-\zeta_3) \qquad N_2 = \frac{1}{8}(1+\zeta_1)(1+\zeta_2)(1-\zeta_3) \\
&N_3 = \frac{1}{8}(1-\zeta_1)(1+\zeta_2)(1-\zeta_3) \qquad N_4 = \frac{1}{8}(1-\zeta_1)(1-\zeta_2)(1-\zeta_3) \\
&N_5 = \frac{1}{8}(1+\zeta_1)(1-\zeta_2)(1+\zeta_3) \qquad N_6 = \frac{1}{8}(1+\zeta_1)(1+\zeta_2)(1+\zeta_3) \\
&N_7 = \frac{1}{8}(1-\zeta_1)(1+\zeta_2)(1+\zeta_3) \qquad N_8 = \frac{1}{8}(1-\zeta_1)(1-\zeta_2)(1+\zeta_3)
\end{aligned}
\tag{3.2.31}
$$

Since, the master element shape functions are defined we can use the chain rule
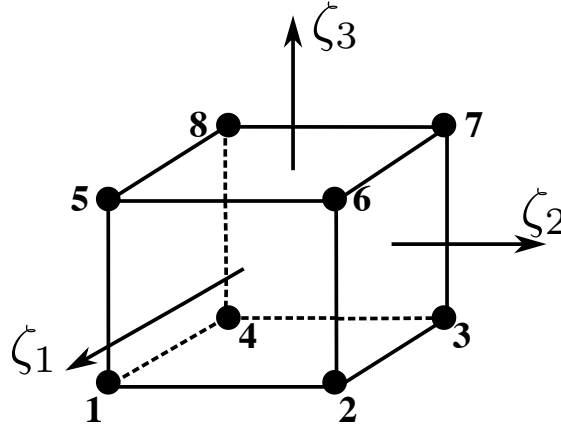
Figure 3.3: This is a 8 nodded brick showing the master element number scheme along with the local coordinate system(ζ_i).

to rewrite the gradient of the shape functions as

$$\frac{\partial N_I}{\partial X_A} = \frac{\partial N_I}{\partial \zeta_i} \frac{\partial \zeta_i}{\partial X_A} \tag{3.2.32}$$

where $\frac{\partial N_I}{\partial \zeta_i}$ can be explicitly computed from Eqn. 3.2.31. This makes the computations much easier as we keep track of one set of shape functions and all calculations are conducted on that master element.

3.3 Dynamic Finite Elements with Explicit integration

In this section, we maintain the dynamic character of the balance of linear momentum and setup an explicit time integration scheme. Again, the balance of linear momentum equation in referential form was given in Eqn. 3.2.1 and is restated below

$$\text{Div}\mathbf{P}^T + \rho_0\mathbf{f} = \rho\ddot{\mathbf{x}} \tag{3.3.1}$$

from this equation we reformulate the weak form and apply a finite element discretization in the spatial dimension and finite difference method in time. Again, we start by multiplying the BLM by the test function $\mathbf{v}$ and integrating, we have

$$\int_{\Omega_0} \mathbf{v} \cdot \left(\text{Div} \mathbf{P}^T + \rho_0 \mathbf{f} \right) d\Omega_0 - \int_{\Omega_0} \mathbf{v} \cdot \rho_0 \ddot{\mathbf{x}} d\Omega_0 = 0 \tag{3.3.2}$$

Thus, the weak form of the equations becomes,

$$\int_{\Omega_0} \nabla_{\mathbf{X}} \mathbf{v} : \mathbf{P}^T d\Omega_0 - \int_{\Gamma_0} \mathbf{v} \cdot \mathbf{T} d\Gamma_0 - \int_{\Omega_0} \rho_0 \mathbf{v} \cdot \mathbf{f} d\Omega_0 + \int_{\Omega_0} \rho_0 \mathbf{v} \cdot \ddot{\mathbf{x}} d\Omega_0 = 0 \tag{3.3.3}$$

We now have the acceleration term in the weak form. We can recast the acceleration term using a finite difference approximation, such that

$$
\begin{aligned}
\dot{u}(t + \Delta t) &= \frac{u(t + \Delta t) - u(t)}{\Delta t} \\
\dot{u}(t) &= \frac{u(t) - u(t - \Delta t)}{\Delta t}
\end{aligned}
\tag{3.3.4}
$$

and the acceleration is then

$$
\begin{aligned}
\ddot{u} &= \frac{\dot{u}(t + \Delta t) - \dot{u}(t)}{\Delta t} \\
&= \frac{\frac{u(t+\Delta t)-u(t)}{\Delta t} - \frac{u(t)-u(t-\Delta t)}{\Delta t}}{\Delta t} \\
&= \frac{u(t + \Delta t) - 2u(t) + u(t - \Delta t)}{\Delta t^2} \\
&= \frac{u^{L+1} - 2u^L + u^{L-1}}{\Delta t^2}
\end{aligned}
\tag{3.3.5}
$$

For an explicit scheme we have the general formula $y(t + dt) = f(y(t))$, in other words our function calculation depends only on values that are already knows, hence plugging the time discretization into the weak form we obtain

$$\int_{\Omega_0} \nabla_{\mathbf{X}} \mathbf{v} : (\mathbf{P}^T)^L d\Omega_0 - \int_{\Gamma_0} \mathbf{v} \cdot \mathbf{T}^L d\Gamma_0 - \int_{\Omega_0} \rho_0 \mathbf{v} \cdot \mathbf{f}^L d\Omega_0 + \int_{\Omega_0} \rho_0 \mathbf{v} \cdot \frac{\mathbf{x}^{L+1} - 2\mathbf{x}^L + \mathbf{x}^{L-1}}{\Delta t^2} d\Omega_0 = 0 \tag{3.3.6}$$

Using the previously described finite element discretization in the static case of

$u_i = a_{iI}N_I$ and $v = b_{iI}N_I$ and plugging back into the weak form we get

$$\int_{\Omega_0}\frac{\partial v_i}{\partial X_A}P_{jA}^L\Omega_0 - \int_{\Gamma_0}v_iT_i^Ld\Gamma_0 - \int_{\Omega_0}\rho_0v_if_i^Ld\Omega_0 + \int_{\Omega_0}\rho_0v_i\frac{x_i^{L+1}-2x_i^L+x_i^{L-1}}{\Delta t^2}d\Omega_0 =$$
$$\int_{\Omega_0}b_{iI}\frac{\partial N_I}{\partial X_A}P_{jA}^L\Omega_0 - \int_{\Gamma_0}b_{iI}N_IT_i^Ld\Gamma_0 - \int_{\Omega_0}\rho_0b_{iI}N_If_i^Ld\Omega_0$$
$$+ \int_{\Omega_0}\rho_0b_{iI}N_I\frac{a_{iJ}^{L+1}N_J-2a_{iJ}^LN_J+a_{iJ}^{L-1}N_J}{\Delta t^2}d\Omega_0 = 0$$

$$(3.3.7)$$

extracting the b_{iI} term we have the form

$$\int_{\Omega_0}\frac{\partial N_I}{\partial X_A}P_{jA}^L\Omega_0 - \int_{\Gamma_0}N_IT_i^Ld\Gamma_0 - \int_{\Omega_0}\rho_0N_If_i^Ld\Omega_0$$
$$+ \frac{a_{iJ}^{L+1}-2a_{iJ}^L+a_{iJ}^{L-1}}{\Delta t^2}\int_{\Omega_0}\rho_0N_IN_Jd\Omega_0 = 0$$

$$(3.3.8)$$

We can now define the mass matrix as $\mathbf{M} = \int_{\Omega_0}\rho_0N_IN_Jd\Omega_0$ and the following expression ensues

$$\int_{\Omega_0}\frac{\partial N_I}{\partial X_A}P_{jA}^L\Omega_0 - \int_{\Gamma_0}N_IT_i^Ld\Gamma_0 - \int_{\Omega_0}\rho_0N_If_i^Ld\Omega_0 + \frac{M_{IJ}}{\Delta t^2}(a_{iJ}^{L+1}-2a_{iJ}^L+a_{iJ}^{L-1}) = 0$$

$$(3.3.9)$$

rearranging the system we obtain the following expression for the displacement update

$$a_{iJ}^{L+1} = \left(\frac{M_{IJ}}{\Delta t^2}\right)^{-1}\left(-\int_{\Omega_0}\frac{\partial N_I}{\partial X_A}P_{jA}^L\Omega_0 + \int_{\Gamma_0}N_IT_i^Ld\Gamma_0 + \int_{\Omega_0}\rho_0N_If_i^Ld\Omega_0\right) + 2a_{iJ}^L - a_{iJ}^{L-1}$$

$$(3.3.10)$$

The algorithm in Eqn. 3.3.10 is suitable only for constant time step. However, for most purposes the time step will be changing due to deformation(Consequence of finding the critical time step). The only difference in the derivation arises from this modification

$$\dot{u}(t + \Delta t) = \frac{u(t + \Delta t) - u(t)}{\Delta t^L}$$

$$\dot{u}(t) = \frac{u(t) - u(t - \Delta t)}{\Delta t^{L-1}}$$

(3.3.11)

plugging this expression back into the acceleration we obtain the following algorithm

$$
\begin{aligned}
a_{iJ}^{L+1} &= \left(\frac{M_{IJ}}{(\Delta t^L)^2}\right)^{-1}\left(-\int_{\Omega_0}\frac{\partial N_I}{\partial X_A}P_{jA}^L\Omega_0 + \int_{\Gamma_0}N_I T_i^L d\Gamma_0 + \int_{\Omega_0}\rho_0 N_I f_i^L d\Omega_0\right) \\
&\quad + \Delta t^L \dot{u}^L + a_{iJ}^{L-1} \\
&= \left(\frac{M_{IJ}}{(\Delta t^L)^2}\right)^{-1}\left(-\int_{\Omega_0}\frac{\partial N_I}{\partial X_A}P_{jA}^L\Omega_0 + \int_{\Gamma_0}N_I T_i^L d\Gamma_0 + \int_{\Omega_0}\rho_0 N_I f_i^L d\Omega_0\right) \\
&\quad + \Delta t^L\left(\frac{a_{iJ}^L - a_{iJ}^{L-1}}{\Delta t^{L-1}}\right) + a_{iJ}^{L-1}
\end{aligned}
$$

(3.3.12)

3.3.1 Diagonal Mass Matrix Estimation

The mass matrix $\mathbf{M}$ needs to be computed from $\mathbf{M} = \int_{\Omega_0}\rho_0 N_I N_J d\Omega_0$. However, computing this with regular gauss quadrature will result in a non-diagonal matrix. This means that we must find $\mathbf{M}^{-1}$ in a general setting. However, to avoid this expensive calculation we can build the mass matrix as a diagonal matrix if we use the nodal positions for the quadrature rule. This is done using the trapezoidal rule with quadrature points at $\zeta = \pm 1$ and weights $w = 1$. Hence, the integration can be estimated as

$$
\begin{aligned}
\mathbf{M} &= \int_{\Omega_0}\rho_0 N_I N_J d\Omega_0 \\
&= \int_{\Omega_0}\rho_0 N_I N_J J d\Omega_0 \\
&= \int_{-1}^{1}\int_{-1}^{1}\int_{-1}^{1}\rho_0 N_I N_J J d\zeta_1 d\zeta_2 d\zeta_3 \\
&= \sum_{i=1}^{2}\sum_{j=1}^{2}\sum_{k=1}^{2}\rho_0 w_i w_j w_k N(\zeta_1^i.\zeta_2^j, \zeta_3^k)_I N(\zeta_1^i.\zeta_2^j, \zeta_3^k) J
\end{aligned}
$$

(3.3.13)

Since the integration is over the nodal positions only diagonal terms appear in the matrix.

This makes the inverse trivial to compute.

3.3.2 Stability of Explicit Integration

Generally speaking explicit schemes are conditionally stable. To maintain stability the CFL condition must be satisfied, refer to Cook et al [27] for details. This is stated as

$$\frac{\Delta t c}{L} \leq 1 \tag{3.3.14}$$

where L is defined as the characteristic length of an element and $c = \sqrt{E/\rho}$ is the wave speed, with ρ being the current density and E the Young's modulus. The equation can be rearranged to define the critical time step as

$$\Delta t_{crit} \leq \frac{L}{c} \tag{3.3.15}$$

This calculation is conducted over each element in the analysis and the final time step is the smallest Δt_{crit} over all the elements. The characteristic length is defined as the shortest length in an element, this will result in a conservative critical time step.

Chapter 4

Homogenization Techniques

In this chapter the average material properties of fiber composites are determined using homogenization techniques. There has been extensive work in this field which includes the contributions of Aboudi [2], Nemat-Nasser [1], Christensen [4], C.T.Sun [28] and Zohdi [29]. The methods include both analytical approaches to obtaining bounds on the material properties to numerical experiments using the Finite Element Method. The above references have focused on homogenization for linear elasticity. There have also been advances on the front of homogenization in finite elasticity with works from Temizer [30], Wriggers [31], Khisaeva [32] and Kanit et al. [33]. The focus of this chapter will be on linear elastic materials with special attention to fiber composites. Although our focus is on fiber composites, the numerical approaches are valid for any set of particle morphologies. Numerical homogenization for isotropic macroscopic material properties for various particle morphologies has been analyzed by Temizer [34].

4.1 Homogenization in Linear Elasticity

Typically materials have multiple constituents in them, i.e they are heterogeneous. However, at sufficiently low magnification we see a uniform material. For example, in the case of metals on the macroscopic scale we do not see the microscopic grains. When material tests are conducted on for example, a sample of aluminum, the results are the material properties in an average sense. These average properties are essential to engineering design. To illustrate the effect of homogenization Figure 4.1 shows an illustration of the expected

response in a one dimensional test. The first test includes the micro-constituents and we find that the displacement response is non-uniform due to variation of the material properties. On the other hand, the second test is of a homogenized material and we find the displacement response to be smooth throughout the body.
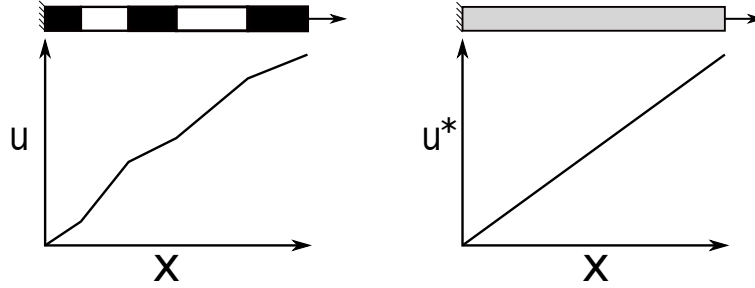
Figure 4.1: This figure qualitatively shows the response of heterogeneous material on the left and a material with homogeneous material properties on the right

When thinking of homogenization we can identify two boundary value problems, the first identified with the exact material properties $\mathbb{C}(x)$ defined in the weak sense as

$$\text{Find } \mathbf{u} \in H^1(\Omega), \mathbf{u}|_{\Gamma_u} = \mathbf{d}, \text{where } \forall \mathbf{v} \in H^1(\Omega)$$

$$\int_\Omega \nabla \mathbf{u} : \mathbb{C}(x) : \nabla \mathbf{v} d\Omega = \int_\Omega \mathbf{f}.\mathbf{v} d\Omega + \int_{\Gamma_t} \mathbf{t}.\mathbf{v} d\Gamma \qquad (4.1.1)$$

where, $\mathbf{t} = \boldsymbol{\sigma}\mathbf{n}$ on Γ_t. Numerically resolving this problem is not tractable. Therefore through the process of homogenization we solve an approximate problem with homogenized material properties $\mathbb{C}^*$ under the same boundary conditions as the heterogenous boundary value problem such that

$$\text{Find } \mathbf{u}^* \in H^1(\Omega), \mathbf{u}^*|_{\Gamma_u} = \mathbf{d}, \text{where } \forall \mathbf{v} \in H^1(\Omega)$$

$$\int_\Omega \nabla \mathbf{u}^* : \mathbb{C}^* : \nabla \mathbf{v} d\Omega = \int_\Omega \mathbf{f}.\mathbf{v} d\Omega + \int_{\Gamma_t} \mathbf{t}.\mathbf{v} d\Gamma \qquad (4.1.2)$$

hence, we must identify $\mathbb{C}^*$ which is referred to as the effective, homogenized or macroscopic material properties. We note also that H^1 denotes the Hilbert space in which the finite

element solution exists. The corresponding norm in this space is identified as $||\mathbf{u}||_{H^1} = \int_\Omega \frac{\partial \mathbf{u}}{\partial \mathbf{x}} : \frac{\partial \mathbf{u}}{\partial \mathbf{x}} d\Omega + \int_\Omega \mathbf{u} \cdot \mathbf{u} d\Omega$.

4.2 Identification of a Representative Volume Element

To obtain a relation between the micro-macro scales we must take a sample that is representative of the micro-constituents, this sample is known as a representative volume element (RVE) and can be thought of as a continuum material point. There are a number of definitions for an RVE. However, a typical definition starts by expressing a separation of scales between the micro and macro ranges. To this end, the characteristic lengths of the components are first identified as

1. Structural Scale: L_1

2. Representative Volume Element(RVE) scale: L_2

3. Micro-constituent scale: L_3

we then require that $L_1 >> L_2$ and $L_2 >> L_3$, as illustrated in Figure. 4.2. The size differences between the characteristic lengths allows us to identify a uniform material at every point. In turn, this is a requirement on the size of the RVE, meaning that stress-strain response for a given RVE must be independent of the microstructural variations in the structural scale. Hence, the RVE is statistically representative and therefore we can take a sample from anywhere in the structural scale.

With an RVE identified we can calculate the homogenized properties through a relationship between averages where we have

$$\langle \boldsymbol{\sigma} \rangle = \mathbb{C}^* : \langle \boldsymbol{\epsilon} \rangle \tag{4.2.1}$$

and the notation $\langle \cdot \rangle = \frac{1}{\Omega} \int_\Omega \cdot d\Omega$ indicates the average over a volume Ω. In this case the stress and strain are computed over the RVE and are averaged to obtain the relationship identified in Eqn. 4.2.1. This is the fundamental basis behind statistical homogenization.
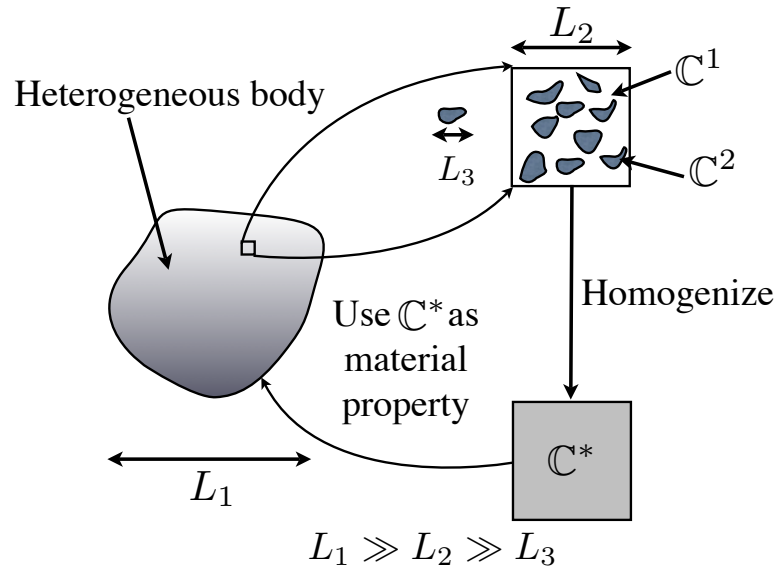
Figure 4.2: Homogenization process and description of separation of scales showing that $L_1 \gg L_2 \gg L_3$. Also $\mathbb{C}^1$ is the matrix material property while $\mathbb{C}^2$ is the fiber/particle material property and $\mathbb{C}^*$is the homogenized material property

4.3   Micro-Macro Energy Balance

The micro-macro energy balance states that average energy of the heterogenous material is equal to the energy of the homogenous material. This is mathematically stated as

$$\langle \boldsymbol{\sigma} : \boldsymbol{\epsilon} \rangle = \langle \boldsymbol{\sigma} \rangle : \langle \boldsymbol{\epsilon} \rangle \tag{4.3.1}$$

This is known as Hill's condition. Further details and proof of the energy balance is found in Hill [35] and Huet [36]. To satisfy the condition in Eqn. 4.3.1 the following boundary conditions are used

1. Linear displacement

$$\mathbf{u}|_{\delta\Omega} = \mathcal{E}.\mathbf{x} \tag{4.3.2}$$

2. Constant traction

$$\mathbf{t}|_{\delta\Omega} = \mathcal{L}.\mathbf{n} \tag{4.3.3}$$

where $\mathcal{E}, \mathcal{L}$ are constant strain and stress tensors. Note, that when using these special boundary conditions Eqn 4.3.1 is satisfied regardless of the size of the RVE. Since either of these conditions can be used to obtain the macroscopic response we note that depending on the size of the RVE, each test would give a different result that bounds the real effective property. Hence, from Huet [36] we have the following conditions

$$\langle \boldsymbol{\sigma} \rangle = \mathbb{C}_\epsilon : \langle \boldsymbol{\epsilon} \rangle, \qquad \text{Linear displacement} \tag{4.3.4}$$

$$\langle \boldsymbol{\sigma} \rangle = \mathbb{C}_\sigma : \langle \boldsymbol{\epsilon} \rangle, \qquad \text{Constant traction} \tag{4.3.5}$$

and the following bound is obtained

$$\mathbb{C}_\sigma \leq \mathbb{C}^* \leq \mathbb{C}_\epsilon \tag{4.3.6}$$

we refer to $\mathbb{C}_\epsilon$ and $\mathbb{C}_\sigma$ as the apparent macroscopic properties. While $\mathbb{C}^*$ is referred to the effective, homogenized or macroscopic properties. Moreover, as illustrated in Figure. 4.3 as the RVE size increases the results from both tests converge to the same value. This is another definition of an RVE, which states that the appropriate size of the RVE is obtained when the material response from both constant traction and linear displacement boundary conditions are equivalent.

4.4 Average Strain-Stress Theorem

In this section we briefly state the average stress/strain theorem. The theorem is straightforward and a full derivation can be found in Zohdi [29]. We start by considering a heterogeneous body loaded uniformly on its boundary by Eqn. 4.3.2. The result states that for a perfectly bonded material that $\langle \boldsymbol{\epsilon} \rangle_\Omega = \mathcal{E}$. A similar statement can be shown when the boundary condition defined by Eqn. 4.3.3 is used. Specifically, the result states that under these boundary condition the average stress $\langle \boldsymbol{\sigma} \rangle_\Omega = \mathcal{L}$. Therefore, these boundary
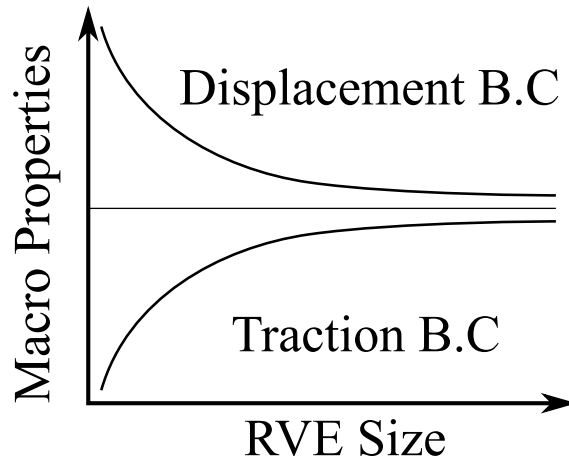
Figure 4.3: Effect of Boundary Condition type on homogenization. Specifically showing that traction boundary conditions produce a lower bound on the material properties, while displacement boundary conditions produce an upper bound with the two approaching the real effective property as the RVE size increases.

conditions are also sometimes called homogenous boundary condition because when applied on a uniform/homogeneous body the stress/strain response is homogeneous(the same at every material point).

4.5 Analytical Bounds

Our interest is to derive the average properties of the elasticity tensor such that

$$\langle \boldsymbol{\sigma} \rangle = \mathbb{C}^* \langle \boldsymbol{\epsilon} \rangle \tag{4.5.1}$$

where, $\mathbb{C}^*$ is the effective elasticity tensor.

In the general case when the material is fully anisotropic a full set of 6 tests are necessary. Each test will recover a column of material properties. Depending on whether we use constant strain or constant stress the average properties will be different. These two different boundary conditions will result into bounds on the effective material properties. They are generally known as Voigt-Reuss bounds. Voigt assumed that the strain field is constant, $\langle \boldsymbol{\epsilon} \rangle = \boldsymbol{\epsilon}_0$, in a representative volume element. Hence, $\langle \boldsymbol{\sigma} \rangle = \langle \mathbb{C} \boldsymbol{\epsilon} \rangle = \langle \mathbb{C} \rangle \boldsymbol{\epsilon}_0$. On the other hand, Reuss assumed that the stress field is constant in an RVE, $\langle \boldsymbol{\sigma} \rangle = \boldsymbol{\sigma}_0$, hence,

we have the relation that $\langle \boldsymbol{\epsilon} \rangle = \langle \mathbb{C}^{-1} \boldsymbol{\sigma} \rangle = \langle \mathbb{S} \rangle \boldsymbol{\sigma}_0$. Therefore, $\langle \mathbb{C} \rangle = \langle \mathbb{S} \rangle^{-1}$. The following bounds [36] are therefore obtained

$$\langle \mathbb{S} \rangle^{-1} \leq \mathbb{C}^* \leq \langle \mathbb{C} \rangle \tag{4.5.2}$$

we note that inequality is a measure of the eigenvalues, where the difference in the eigenvalues of $\mathbb{C}^* - \langle \mathbb{S} \rangle^{-1} \geq 0$ and $\langle \mathbb{C} \rangle - \mathbb{C}^* \geq 0$. We note that these bounds are generally not accurate. For a macroscopically anisotropic material with isotropic constituents the predicted bounds would be isotropic. This is obviously a weakness of these analytical results when our interest is fiber composites.

We now consider the Hashin-Rosen bounds which are described in detail in Hashin and Rosen. [37] and in Christensen. [4]. These bounds generally provide much tighter bounds than the Voigt-Reuss bounds. They also produce macroscopically transversely isotropic effective bounds. The results are obtained using the minimum theories of elasticity and presume $\mu_1 > \mu_2$ and $\kappa_1 > \kappa_2$, where κ is the bulk modulus of the given phase defined as $\kappa = \frac{-1}{3} \frac{E\mu}{E - 2\mu}$. The bounds are summarized in Eqns. 4.5.3-4.5.7

$$K_2 + \frac{v_1}{1/(K_1 - K_1) + v_2/(K_2 + \mu_2)} \leq K_{23} \leq K_1 + \frac{v_2}{1/(K_2 - K_1) + v1/(K_1 + \mu_1)} \tag{4.5.3}$$

$$\mu_2 + \frac{v_1}{1/(\mu_1 - \mu_2) + v_2(K_2 + 2\mu_2)/2\mu_2(K_2 + \mu_2)}$$
$$\leq \mu_{23} \leq \mu_1 + \frac{v_2}{1/(\mu_2 - \mu_1) + v_1(K_1 + 2\mu_1)/2\mu_1(K_1 + \mu_1)} \tag{4.5.4}$$

$$\mu_2 + \frac{v_1}{1/(\mu_1 - \mu_2) + v_2/2\mu_2} \leq \mu_{12} \leq \mu_1 + \frac{v_2}{1/(\mu_2 - \mu_1) + v_1/2\mu_1} \tag{4.5.5}$$

$$\frac{v_1 v_2}{v_1/K_2 + v_2/K_1 + 1/\mu_2} \leq \frac{E_{11} - v_1 E_1 - v_2 E_2}{4(\nu_1 - \nu_2)^2} \leq \frac{v_1 v_2}{v_1/K_2 + v_2/K_1 + 1/\mu_1} \tag{4.5.6}$$

$$\frac{v_1 v_2}{v_1/K_2 + v_2/K_1 + 1/\mu_2} \leq \frac{\nu_{12} - v_1\nu_1 - v_2\nu_2}{(\nu_1 - \nu_2)(1/K_2 - 1/K_1)} \leq \frac{v_1 v_2}{v_1/K_2 + v_2/K_1 + 1/\mu_1} \quad (4.5.7)$$

where $K = \kappa + \frac{1}{3}\mu$, $K_{23} = \frac{1}{2}(C_{22} + C_{23})$ and we also have the follow relationship for E_{22} as

$$E_{22} = \frac{4\mu_{23}K_{23}}{K_{23} + \mu_{23} + 4\nu_{12}^2\mu_{12}K_{23}/E_{11}} \quad (4.5.8)$$

4.6 Numerical RVE Size

We now focus on numerical homogenization. Although analytical bounds exist to obtain effective properties, they are generally not very accurate. To obtain better estimates on the effective properties, we utilize numerical techniques as described in Chapter 3. Using the finite element methods allows considerable freedom in understanding various effects that are not captured through analytical methods. For example, the effect of various micro-constituent geometries on the effective properties can be explored, also anisotropic micro-constituents can be added. To obtain the size of an RVE we must be able to find the pointwise strain/stress fields in a sample of material. In addition, the boundary conditions applied on the RVE are those which satisfy hills condition. Since in the limit, the macroscopic property $\mathbb{C}^*$ is independent of the type of applied boundary condition, we explain the numerical process with attention to the linear displacement boundary conditions. We begin by assuming a small RVE size with some set number of micro-constituents and extracting the macroscopic property $\mathbb{C}_\epsilon^I$, where I denotes the RVE size. The sample size is subsequently increased by adding more micro-constituents and obtaining a new approximation $\mathbb{C}_\epsilon^{I+1}$. The process of increasing the size of the RVE is illustrated in Figure. 4.4. We can then define the converged macroscopic property when

$$\frac{||\mathbb{C}_\epsilon^{I+1} - \mathbb{C}_\epsilon^I||}{||\mathbb{C}_\epsilon^I||} \leq TOL \quad (4.6.1)$$

Once we have a converged result we can assume that $\mathbb{C}^* \approx \mathbb{C}_\epsilon$. This same process is applicable to the case of constant traction boundary conditions.
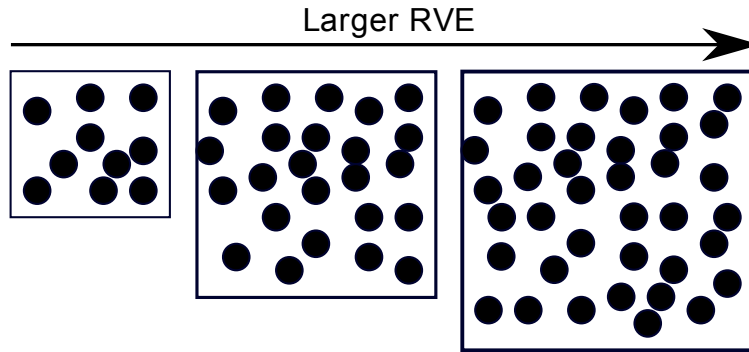
Figure 4.4: Increasing the size of the RVE by including more fibers in the domain

4.7 Ensemble Averaging

When considering random fibers, for a given sample size, we can create different realizations or instances of that size. Therefore, to quantify the randomness it is important to consider multiple samples with different random orientations and average the results. This is known as ensemble averaging and is illustrated in Figure. 4.5 . We mathematically define the ensemble average when considering linear displacement boundary conditions as

$$\langle\langle\mathbb{C}_\epsilon\rangle\rangle^N = \frac{1}{N}\sum_{i=1}^{N}\mathbb{C}_\epsilon^i \tag{4.7.1}$$
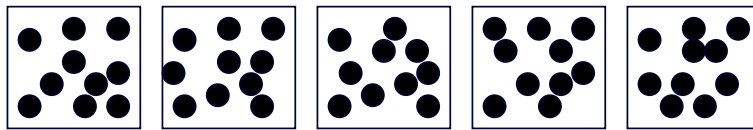
Figure 4.5: Different samples for same number of fibers. Note the different realizations of the fiber positions

where N is the number of samples. We can also set a convergence parameter for the ensemble average such that

$$\frac{||\langle\langle\mathbb{C}_\epsilon\rangle\rangle^{N+1} - \langle\langle\mathbb{C}_\epsilon\rangle\rangle^N||}{||\langle\langle\mathbb{C}_\epsilon\rangle\rangle^N||} \leq TOL \tag{4.7.2}$$

we note that for a small RVE size with few micro-constituents the variation between samples is larger than that of a large RVE. Hence we usual require more samples for a converged ensemble average when looking at smaller RVEs.

Chapter 5

Numerical Experiments in Homogenization

In this chapter a summary of the results we have obtained from homogenization of random unidirectional fibers in linear elasticity is presented. Particularly, we explore the issues involved in ensemble averaging and identification of the RVE size. These numerical experiments are conducted for different volume fractions and the resulting homogenized properties are compared to some of the analytical bounds described in the previous chapter. We also make a note of the computational cost at the different volume fractions.

5.1 Finite Element Considerations

The finite element method was introduced in Chapter. 3. In this section some issues concerning the modeling of RVE's will be considered. In particular, we are trying to model a sample of a heterogeneous material and in this case fibers inside a matrix. Since, the material is heterogeneous the accuracy of the mesh is essential to capture the material jumps. Figure. 5.1 illustrates an approach to obtain higher accuracy when there are material jumps for a noncomforming uniform mesh. A nonconforming uniform mesh is used for simplicity. However, ideally a material specific (conforming) mesh would be desirable. The idea states that if an element contains multiple materials, the number of gauss points is increased to better capture the material jumps. In elements, where the material is uniform the minimum number of gauss points is used.
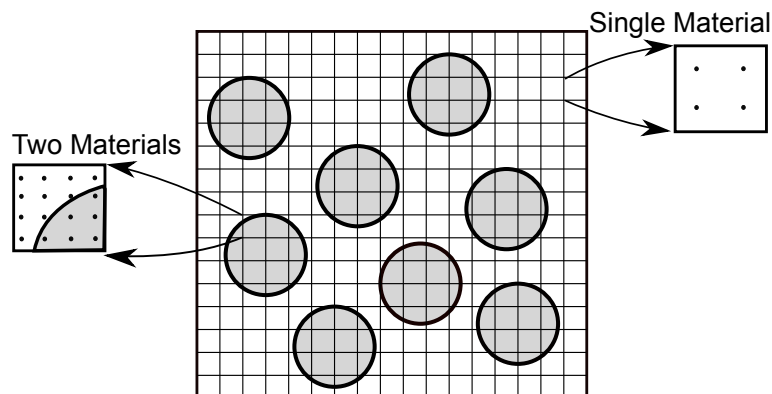
Figure 5.1: This is a schematic of an RVE with fiber showing the mesh along with the variation of Gauss points depending on element location. Specifically, if the element is in one material then less gauss points are used while if the element is shared by the fiber and matrix then more gauss points are used to better sample the region.

5.2 RVE Setup

In this section a description of setting up three dimensional RVEs is summarized. To create an RVE, unidirectional fibers are randomly distributed inside a cube as shown in Figure. 5.2. Figure. 5.3 shows a cross section of two sets of random fiber positions. The specific parameters that dictate the size of the RVE include the fiber volume fraction $\nu_f = \frac{\Omega_f}{\Omega}$, where Ω_f is the total volume of the fiber phase and Ω is total volume of the RVE. Also, the number of random fibers in the matrix, N and the radius of the fiber, r. Given, ν_f, N and r the length of on side of the RVE cube can be calculated such that

$$L = \sqrt{\frac{N\pi r^2}{\nu_f}} \tag{5.2.1}$$

This gives the required length of the RVE as a function of $\{\nu_f, N, r\}$. For the simulations conducted in this chapter, the material properties of the matrix and fiber were chosen to be aluminum and boron, respectively. Table. 5.1 summarizes the properties of these materials. Additionally, the radius of the boron fibers are assumed to be $r = 150e^{-6}m$. With this setup for the RVE, we can proceed in doing some analysis.

Table 5.1: Material Properties for Aluminum and Boron

Material	E(GPa)	ν
Aluminum	70	0.3
Boron	400	0.3
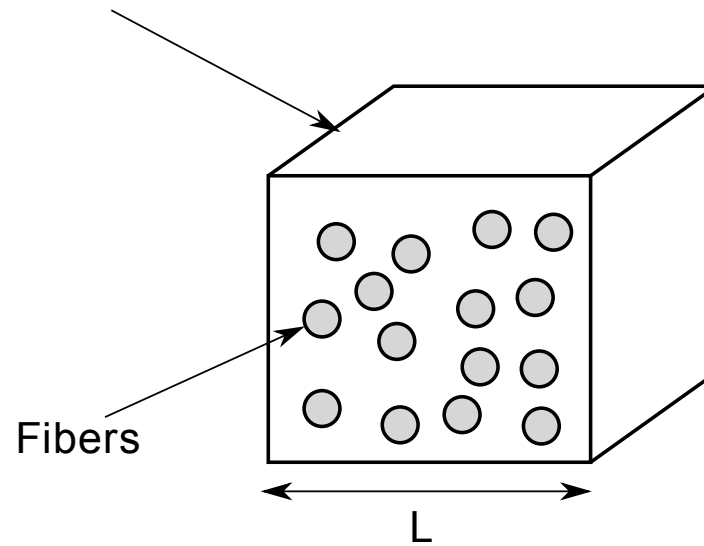
Figure 5.2: Schematic of RVE with randomly positioned unidirectional fibers
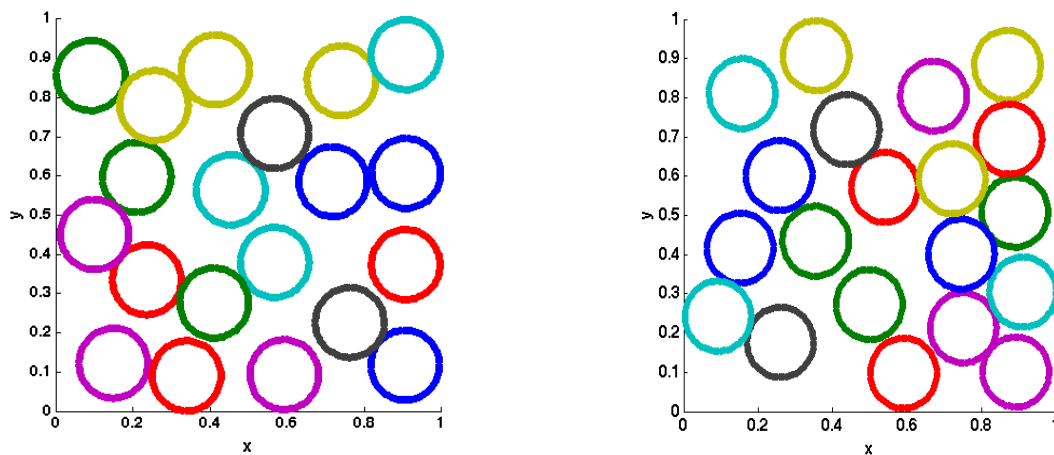
Figure 5.3: Two realizations with random unidirectional fiber position using N = 20 fibers

5.3 Mesh Convergence Study

A convergence study is conducted to determine the number of elements required across a single fiber to produce converged material properties. This is achieved by starting with a small number of elements and continuously refining the mesh until no variation in the results is observed. For these studies , as discussed in Chapter 4, ensemble averaging is used to get average material properties. Determining the number of nodes across a fiber instead of a over the entire RVE simplifies doing other simulations. This is mainly because, once the number of fibers are known in an RVE and given the needed number of nodes across a fiber the total mesh size of the RVE and then be calculated.
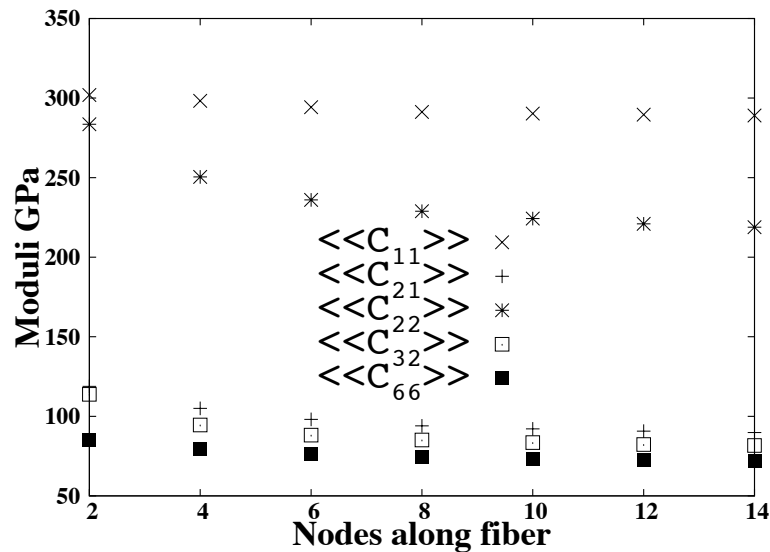
Figure 5.4: This plot shows convergence of the five independent material properties in the elasticity tensor for a transversely isotropic material as a function of the number of nodes along a fiber. Each data point is the ensemble average of 5 samples

This convergence analysis is conducted on an RVE with six fibers with linear displacement boundary conditions imposed. Details on the boundary conditions are left for the next section. There was no real reason behind using six fibers. Note this study is merely to understand how many elements are needed to get converged numerical results, with no concern to whether this RVE is truly representative. From this study, Figure. 5.4 shows the ensemble average from 5 samples at each node set. The plots are of the 5 independent material constants in the elasticity tensor. It is observed that eight nodes across a fiber is

enough to capture the essential properties. With this in mind, this will be the standard number of nodes used for all ensuing numerical experiments.

5.4 Extracting Material Properties

There are two ways to conduct the numerical experiments to obtain material properties. First, we make no assumptions on the material symmetries and therefore, conduct six independent tests that satisfy Hill's criteria. In the second analysis, since out model consists of unidirectional fibers, we can assume transverse isotropy and therefore conduct only three tests to obtain the five material constants. However, we emphasis that for each of the three tests we are determining a column of material properties in the elasticity tensor. Therefore, although we are assuming transverse isotropy we will get some non-zero terms in locations that are otherwise zero. We will discuss this issue in detail in the ensuing sections. It is clear that conducting three tests will be computationally efficient. Eqn. 5.4.1 shows the three different displacement boundary conditions specified to extract the material constants for the three test case. We note that we will only consider displacement boundary conditions for extracting the material properties and determining the size of the RVE. The size experiments will discussed in the upcoming section.

$$\mathbf{u}|_\Omega = \begin{bmatrix} \mathcal{E}_{11} & 0 & 0 \\ 0 & 0 & 0 \\ 0 & 0 & 0 \end{bmatrix} \begin{bmatrix} X_1 \\ X_2 \\ X_3 \end{bmatrix}, \mathbf{u}|_\Omega = \begin{bmatrix} 0 & 0 & 0 \\ 0 & \mathcal{E}_{22} & 0 \\ 0 & 0 & 0 \end{bmatrix} \begin{bmatrix} X_1 \\ X_2 \\ X_3 \end{bmatrix}, \mathbf{u}|_\Omega = \begin{bmatrix} 0 & 0 & \mathcal{E}_{13} \\ 0 & 0 & 0 \\ \mathcal{E}_{13} & 0 & 0 \end{bmatrix} \begin{bmatrix} X_1 \\ X_2 \\ X_3 \end{bmatrix} \quad (5.4.1)$$

We now compare the results from both of these methods. For each scenario, an RVE with thirty fibers with a fiber volume fraction $v_f = 0.5$ is used and a total of ten samples are taken and ensemble averaged. The applied boundary conditions are of the displacement type with component values $\mathcal{E}_{ij} = 0.00001$. The elasticity tensors from both the three tests and six tests are summarized in Eqns. 5.4.2-5.4.3 respectively. The first thing to note is that as mentioned, although we assumed transverse isotropy and conducted three tests, we will not get the exact form of the elasticity tensor defined in Eqn. 2.5.7. For instance, we have non-zero terms in locations that should be zero as can be seen in Eqn. 5.4.2. This is seen when looking at the components C_{41}, C_{42}, C_{43} and C_{56}. Again

the reason these values appear is that for each test, we obtain components for an entire column. Moreover, we show that as the RVE size increases they become negligible. The other subtlety is that the components C_{12} and C_{13} are close but not exactly equal. This can be attributed to the randomness of the fibers and the current size of the RVE.

When comparing the results from the two types of tests, we notice that there are slight differences in some of the terms. This is particularly obvious in the fourth column. Specifically, the component C_{44} is different between the two sets of tests. When conducting three tests, we must calculate the value of C_{44} using the assumption that the material is transversely isotropic therefore, $C_{44} = 0.5(C_{22} - C_{23})$. On the other hand with six tests this comes out of the FEM computation. This is the biggest difference between the two results. It is then reasonable to simply conduct three tests and assume transverse isotropy for this type of RVE configuration. Clearly, this will result in computational savings and is the assumed method for the remaining chapter.

$$\langle\langle \mathbb{C}_\epsilon \rangle\rangle = \begin{bmatrix} 288.394 & 88.683 & 89.116 & 0.192 & 0.000 & 0.000 \\ 88.683 & 213.904 & 81.705 & 0.044 & 0.0000 & 0.000 \\ 89.116 & 81.705 & 213.904 & 0 & 0.000 & 0 \\ 0.192 & 0.044 & 0 & 66.099 & 0.000 & 0 \\ 0.000 & 0.0000 & 0.000 & 0.0000 & 69.081 & 0.121 \\ 0.000 & 0.000 & 0 & 0 & 0.121 & 69.081 \end{bmatrix} \tag{5.4.2}$$

thirty fibers three tests

$$\langle\langle \mathbb{C}_\epsilon \rangle\rangle = \begin{bmatrix} 288.394 & 88.683 & 89.115 & 0.192 & 0.000 & 0.000 \\ 88.683 & 213.904 & 81.705 & 0.044 & 0.000 & 0.000 \\ 89.116 & 81.705 & 215.346 & 0.597 & 0.000 & 0.000 \\ 0.192 & 0.044 & 0.597 & 63.106 & 0.0000 & 0.000 \\ 0.000 & 0.000 & 0.000 & 0.0000 & 69.081 & 0.121 \\ 0.000 & 0.000 & 0.000 & 0.0000 & 0.121 & 68.594 \end{bmatrix} \tag{5.4.3}$$

thirty fibers six tests

5.5   RVE Size and Ensemble Averaging Results

5.5.1   Ensemble Averaging

The numerical experiments are conducted on RVE's with random unidirectional fiber positions. It's important to quantify the effect the randomness has on the overall mechanical properties. For this analysis, two sets of RVE's are considered. The first consists of two fibers and the second consists of thirty fibers. The volume fraction is set to $\nu_f = 0.5$ and the fibers are made of boron while the matrix is aluminum. The effect the size of the RVE has on the ensemble averaging will be examined. We will assume that that overall macroscopic response is transversely isotropic. Therefore, only three tests are necessary to extract the material constants.

In particular, consider the Figures. 5.5-5.8. These plots show how the ensemble average converges with increasing sample size. In addition, the standard deviation of the results are shown in Table. 5.2. The first column of figures shows the raw data $\mathbb{C}_\epsilon$ and the ensemble average $\langle\langle\mathbb{C}_\epsilon\rangle\rangle$ and the second column is the relative error of the ensemble average defined as

$$error = \frac{||\langle\langle\mathbb{C}_\epsilon\rangle\rangle^{N+1} - \langle\langle\mathbb{C}_\epsilon\rangle\rangle^N||}{||\langle\langle\mathbb{C}_\epsilon\rangle\rangle^N||} \tag{5.5.1}$$

where N refer to the number of samples used in the averaging. For the case of two fibers, 200 samples were computed and since the error drops down quickly only the first 100 points are considered in the plot of the error as shown in Figure.5.5-5.6. For all the independent material constants, the ensemble average stabilizes after about 15 samples. It's interesting to note that even with a small number of fibers, the variation in the material properties is not large, this is a consequence of the high volume fraction.

Now, for the case with thirty fibers, 50 samples were taken and the plots of the results are shown in Figure. 5.7-5.8. The same basic results are observed when compared to the case with two fibers. The error of the ensemble average drops rapidly and stabilizes after approximately 10 samples. In both cases, for two fibers and thirty fibers, the error drops down to almost the same value.

The summary of the material properties for the RVE with two fibers and thirty
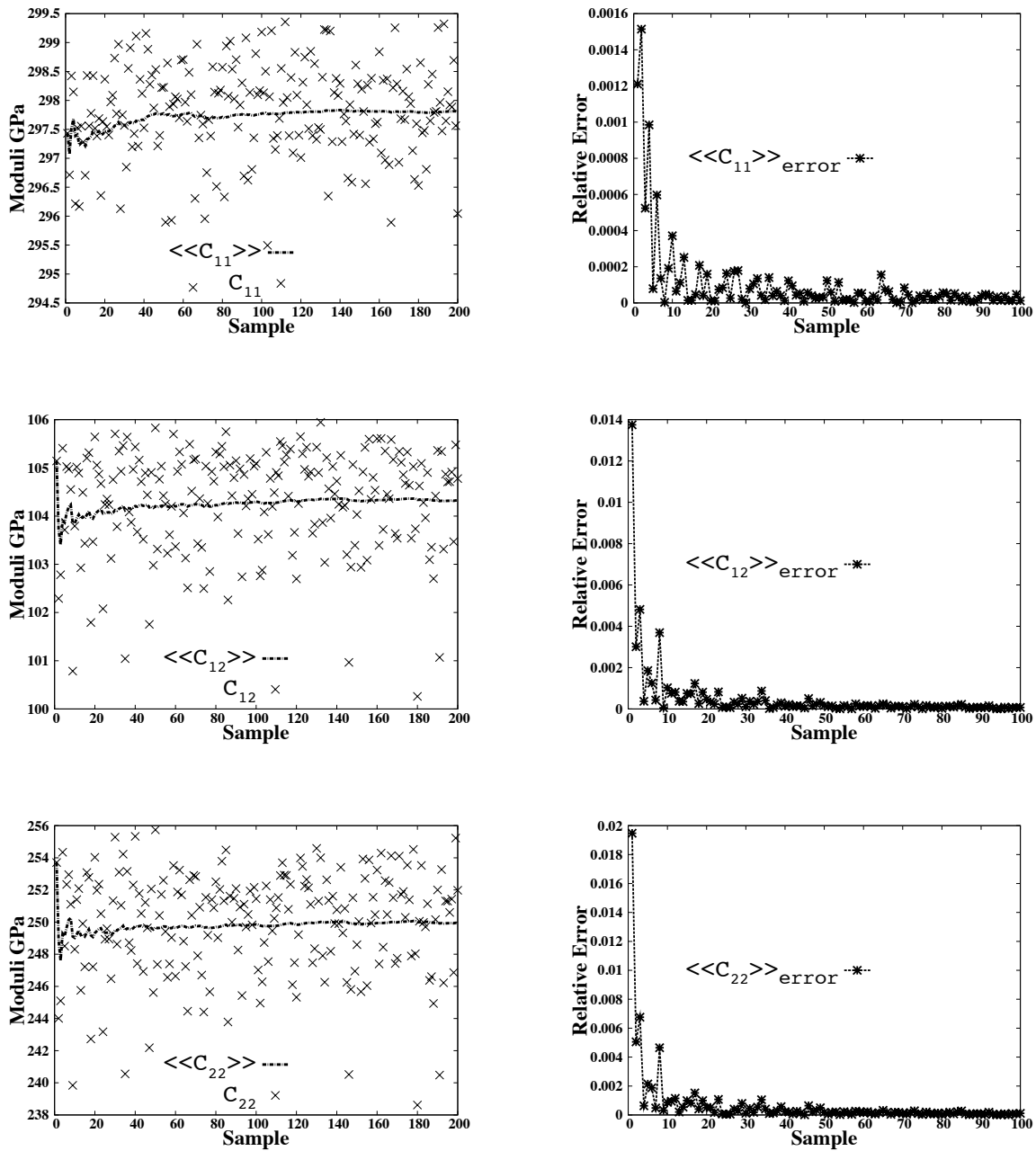
Figure 5.5: The ensemble averaging results are shown on the left column and the relative error is shown on the right column. These results are for simulations with N = 2 and for 200 samples. This set of plots shows the convergence of the components of the individual material properties C_{11}, C_{12} and C_{22}
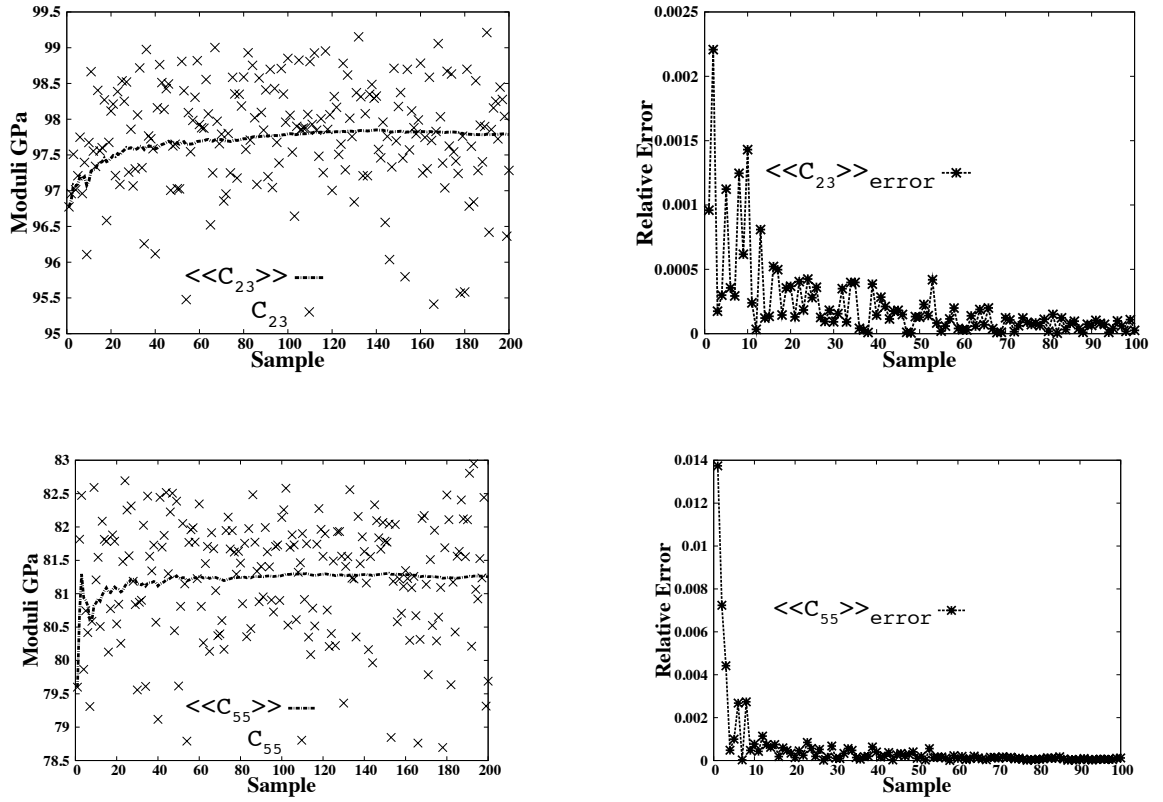
Figure 5.6: The ensemble averaging results are shown on the left column and the relative error is shown on the right column. These results are for simulations with N = 2 and for 200 samples. This set of plots shows the convergence of the components of the individual material properties C_{23} and C_{55}

Table 5.2: Standard deviation of the data is summarized for both $N = 2$ and $N = 30$

Material Constant	Standard deviation	
	N = 2	N = 30
C_{11}	0.8278	0.3285
C_{12}	1.0658	1.1402
C_{22}	3.2553	3.5600
C_{23}	0.7461	0.7959
C_{55}	0.8792	1.1725
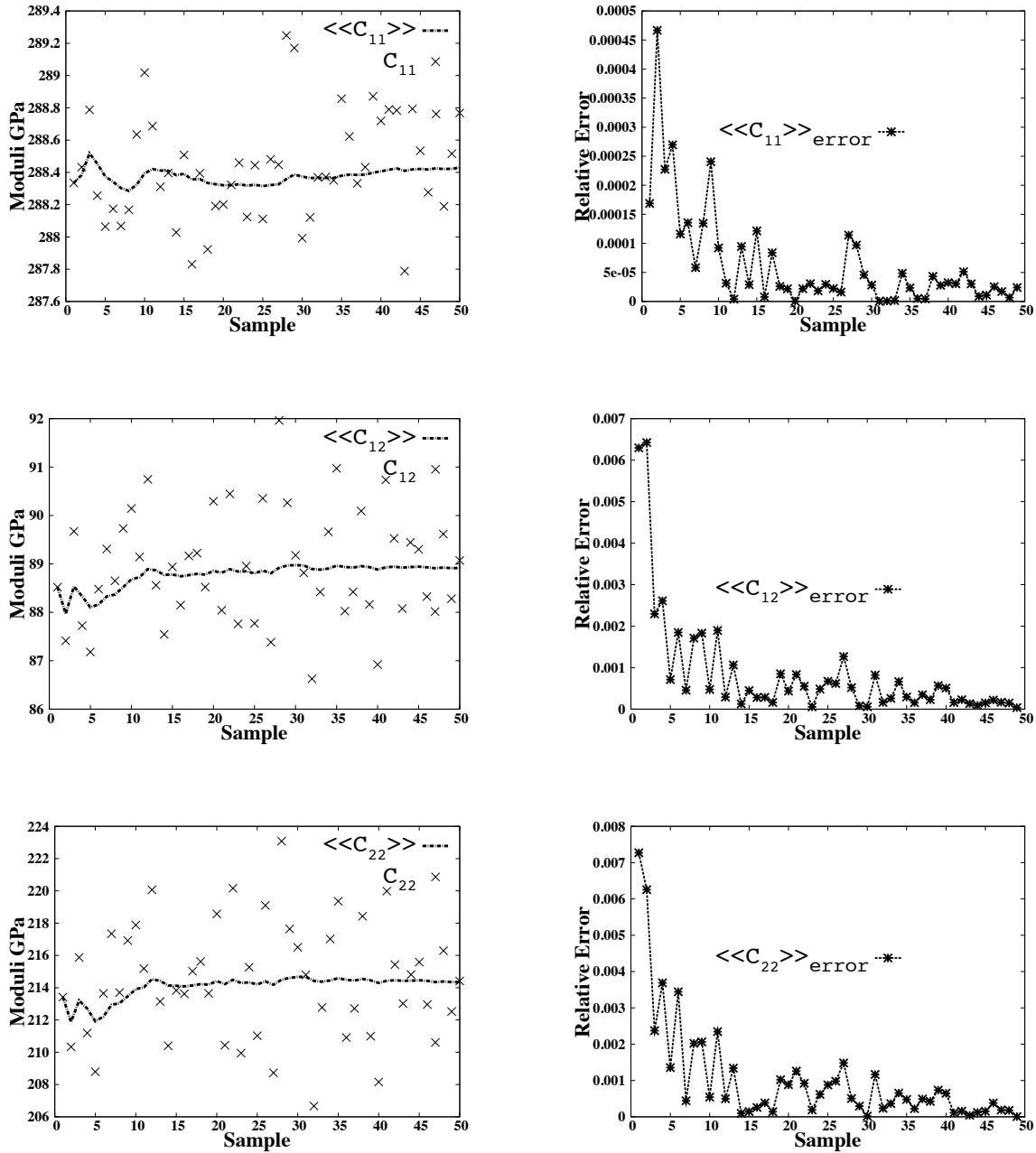
Figure 5.7: The ensemble averaging results are shown on the left column and the relative error is shown on the right column. These results are for simulations with N = 30 and for 50 samples. This set of plots shows the convergence of the components of the individual material properties C_{11}, C_{12} and C_{22}
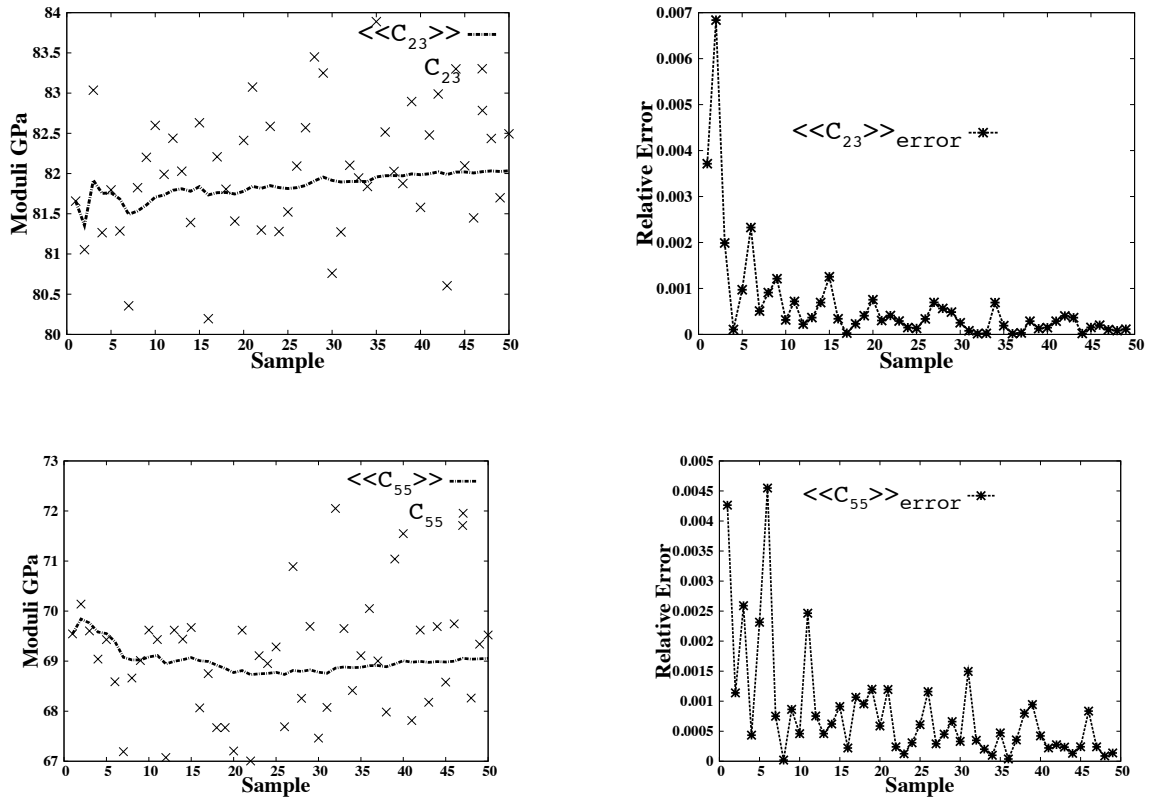
Figure 5.8: The ensemble averaging results are shown on the left column and the relative error is shown on the right column. These results are for simulations with N = 30 and for 50 samples. This set of plots shows the convergence of the components of the individual material properties C_{23} and C_{55}

fibers are shown respectively in the elasticity tensor $\langle\langle \mathbb{C}_\epsilon \rangle\rangle$ in Eqn. 5.5.2-5.5.3.

$$\underbrace{\langle\langle \mathbb{C}_\epsilon \rangle\rangle}_{\text{two fibers}} = \begin{bmatrix} 297.804 & 104.324 & 104.253 & -0.379 & 0.0000 & 0.0000 \\ 104.326 & 249.961 & 97.786 & -0.649 & 0.0000 & 0.0000 \\ 104.253 & 97.783 & 249.961 & 0 & -0.002 & 0 \\ -0.379 & -0.649 & 0 & 76.088 & 0.0000 & 0 \\ 0.0000 & 0.0000 & -0.002 & 0.0000 & 81.252 & -0.237 \\ 0.0000 & 0.0000 & 0 & 0 & -0.237 & 81.252 \end{bmatrix} \tag{5.5.2}$$

$$\underbrace{\langle\langle \mathbb{C}_\epsilon \rangle\rangle}_{\text{thirty fibers}} = \begin{bmatrix} 288.429 & 88.916 & 89.204 & 0.096 & 0.0000 & 0.0000 \\ 88.915 & 214.351 & 82.035 & 0.164 & 0.0000 & 0.0000 \\ 89.204 & 82.035 & 214.351 & 0 & -0.001 & 0 \\ 0.096 & 0.164 & 0 & 66.158 & 0.0000 & 0 \\ 0.0000 & 0.0000 & -0.001 & 0.0000 & 69.056 & 0.076 \\ 0.0000 & 0.0000 & 0 & 0 & 0.076 & 69.056 \end{bmatrix} \tag{5.5.3}$$

We note that the ensemble averaging has no effect on the accuracy of the material properties, notice the difference in the material constants in Eqns. 5.5.2-5.5.3. Including more samples in the simulation with N=2 will not cause the apparent elasticity tensor to approach the effective properties. This should be expected, since the RVE with thirty fibers certainly represents the composite more accurately. Experiments on the size of the RVE will be conducted in the next section. As noted in the previous section, the overall apparent material properties are not strictly transversely isotropic. However, the values of the material constants C_{14}, C_{15}, C_{56} are very small and their value becomes smaller when including more microstructure, as evidenced when looking at Eqns. 5.5.2-5.5.3 . If we look at the distribution of 200 samples for 24 fibers we see the variation of these components of the material properties is about zero, as shown in Figures. 5.9. The effect of these anisotropic terms can be neglected since they are small and their variation occurs around zero. It is important to note that these terms occur only for random fibers. If we situated the fibers in a periodic manner these terms would be identically zero.
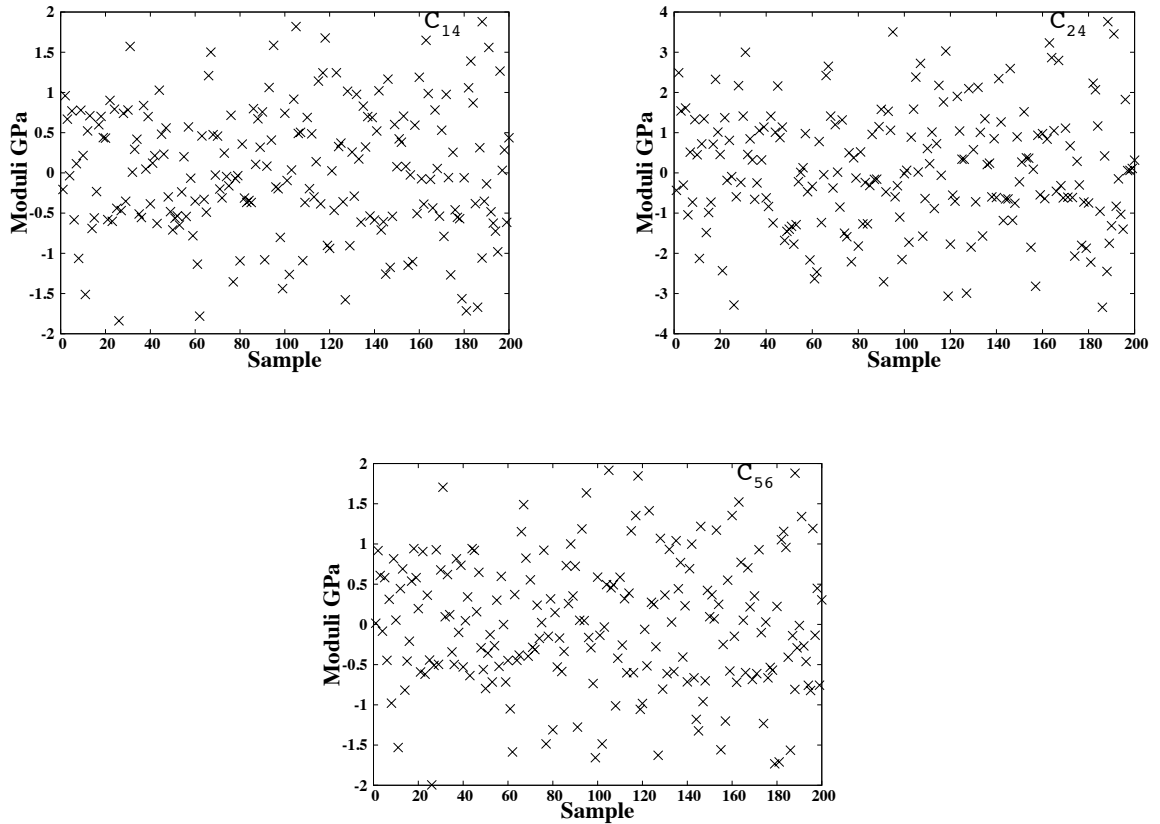
Figure 5.9: These plots show the material properties of C_{14}, C_{24}, C_{56} for 200 samples for N = 24. These components of the material properties fluctuate around zero and therefore can be neglected since as their ensemble average would approach zero as we include more samples

5.5.2 RVE Size Determination

In this section, as previously noted, an analysis of the size of the RVE is conducted. The main purpose is to asses the required size in order to obtain accurate homogenized material properties. The analysis is conducted for a variety of fiber volume fractions and the converged material properties will be compared to analytical homogenization bounds. The considered volume fractions are $\nu_f = [0.1, 0.3, 0.5]$. It should be noted that for $\nu_f > 0.5$ the packing of fibers in the RVE becomes exceedingly difficult for constant cross sectional area fibers, therefore, these conditions are avoided. The parameters for the RVE sizes along with the finite element degrees of freedom for each volume fraction are summarized in Tables. 5.3-5.5, we note that the number of degrees of freedom (DOF)is proportional to L^3 the volume of the RVE. Additionally Figure. 5.10 shows the stress contours of the RVEs at the different volume fraction. We note that for smaller fiber volume fractions, from a computational point of view, we are unable to increase the RVE size as much as when using higher fiber volume fractions. This is because we are using a non-conforming mesh with a constant mesh size. Notice, that for 26 fibers with $\nu_f = 0.5$ and $\nu_f = 0.1$ we needed $397,953$ degrees of freedom with a RVE characteristic length $L = 0.0019$ and $4,444,632$ degrees of freedom respectively with an RVE characteristic length $L = 0.0043$. This issue clearly highlights the advantage of using a conforming mesh as the mesh can be changed adaptively in this case.

The results for the tests are shown in Figures. 5.11-5.13, where again for each RVE size an ensemble average was conducted. The figures show the convergence of the five independent material constants. We notice how as we increase the RVE size the results initially abruptly change and then stabilize to some value. The final elasticity tensors at the largest RVE size for each fiber volume fraction case is summarized in Eqns. 5.5.4-5.5.6. Notice we neglect the terms in the elasticity tensor that fluctuate around zero as described in Chapter. 5.5.1, which gives us a purely transversely isotropic response.

Table 5.3: Table summarizes the RVE size results for $\nu_f = 0.5$, L is the length of a side in the RVE and DOF stands for degrees of freedom used.

Test	Number Fibers	L (m)	DOF
1	2	0.0005	2,197
2	10	0.0012	89,373
3	18	0.0016	222,264
4	26	0.0019	397,953
5	34	0.0022	585,336
6	42	0.0024	786,432
7	50	0.0027	1,029,000
8	58	0.0029	1,316,928
9	66	0.0031	1,594,323
10	74	0.0032	1,908,168
11	82	0.0034	2,235,961

Table 5.4: Table summarizes the RVE size for $\nu_f = 0.3$, L is the length of a side in the RVE and DOF stands for degrees of freedom used.

Test	Number Fibers	L (m)	DOF
1	2	0.00068	17,496
2	10	0.0015	192,000
3	18	0.0020	472,392
4	26	0.0025	862,488
5	34	0.0028	1,265,625
6	42	0.0031	1,715,361
7	50	0.0034	2,260,713
8	58	0.0037	2,823,576
9	64	0.0039	3,278,181

Table 5.5: Table summarizes the RVE size for $\nu_f = 0.1$, L is the length of a side in the RVE and DOF stands for degrees of freedom used.

Test	Number Fibers	L (m)	DOF
1	2	0.0012	89,373
2	10	0.0026	1,029,000
3	18	0.0036	2,572,125
4	26	0.0043	4,444,632

(a) $\nu_f = 0.5$ and $N = 82$

(b) $\nu_f = 0.3$ and $N = 64$

(c) $\nu_f = 0.1$ and $N = 26$
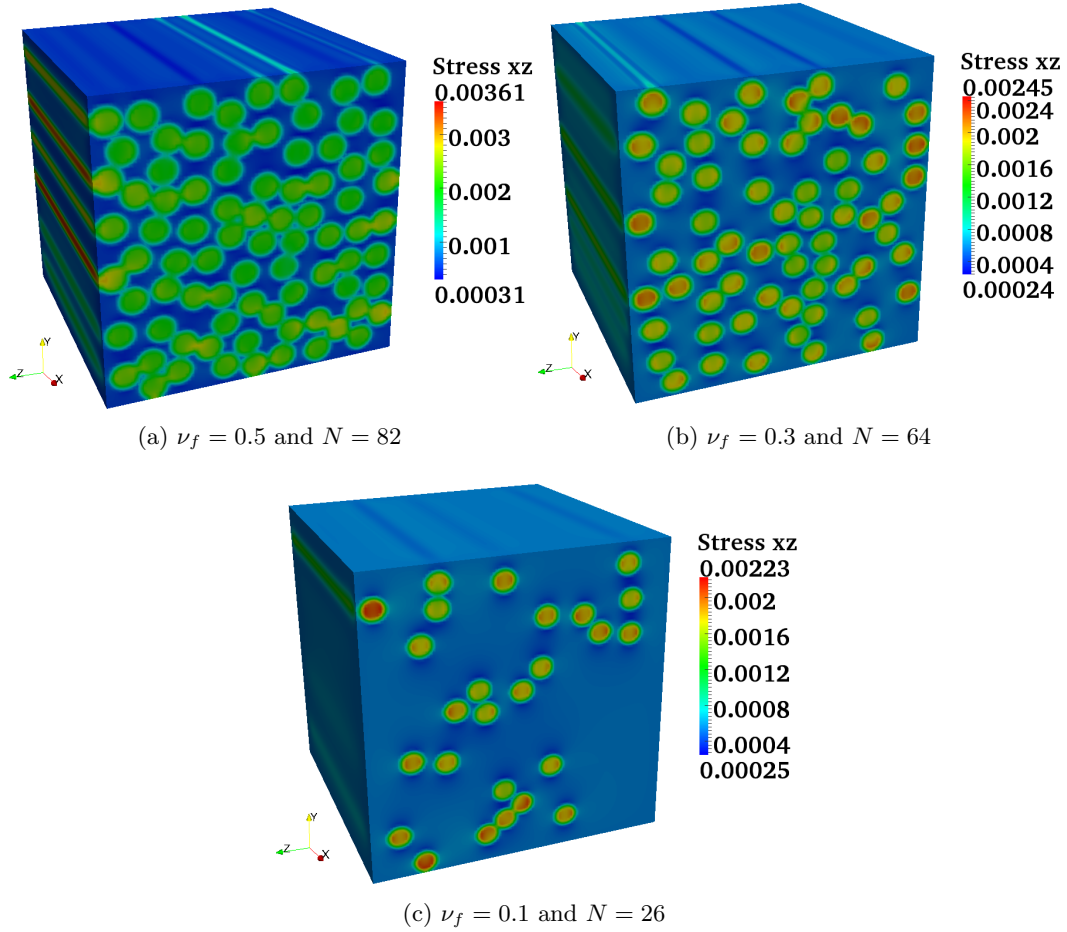
Figure 5.10: Stress contours of σ_{xz} for RVEs at the different volume fractions
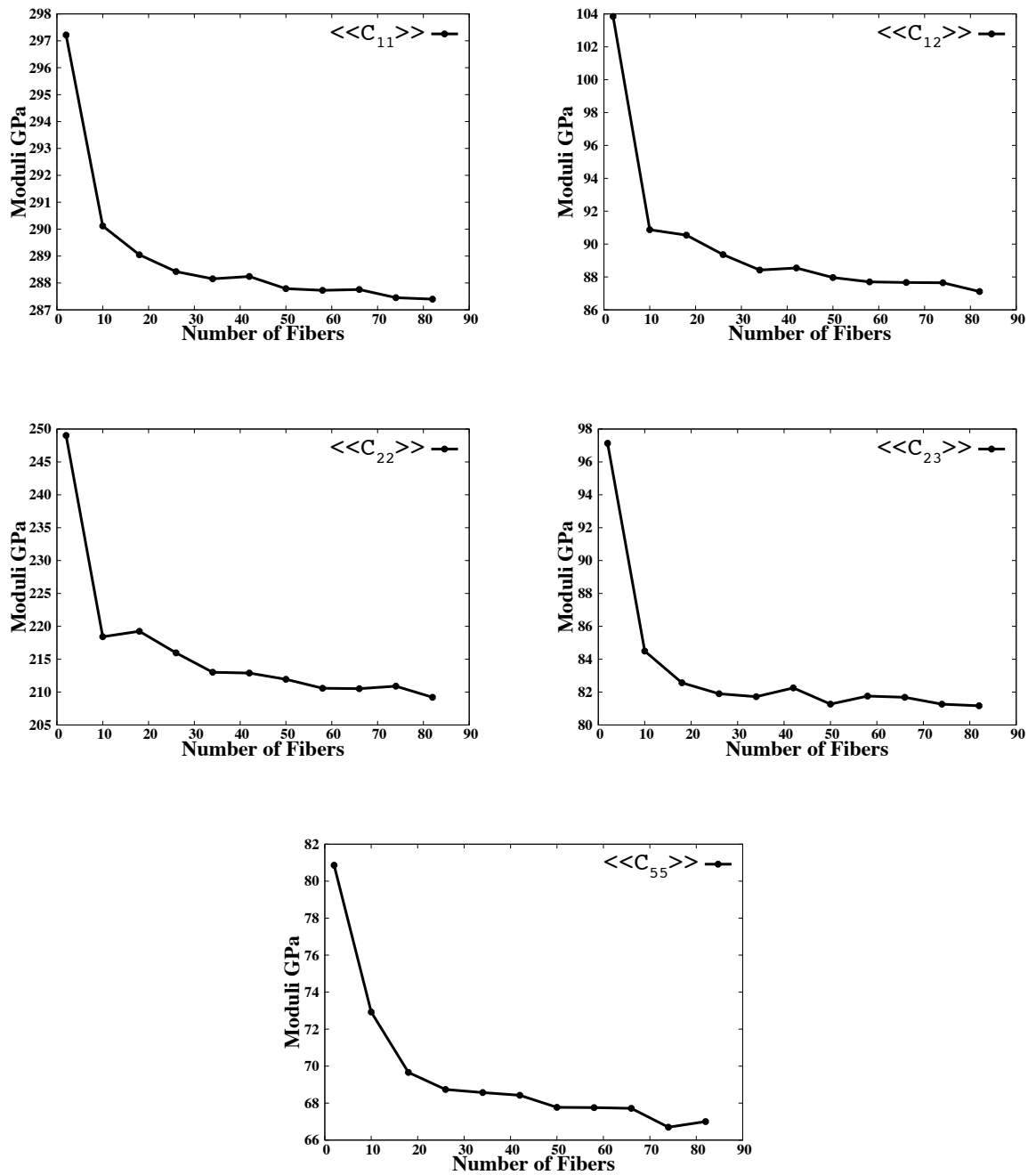
Figure 5.11: Effect of RVE size on properties for $\nu_f = 0.5$. The plots show how the five independent material properties change as a function of the RVE size. The properties converge after a certain RVE size.

$$
\underbrace{\langle\langle \mathbb{C}_\epsilon \rangle\rangle}_{\nu_f=0.5} =
\begin{bmatrix}
287.397 & 87.115 & 87.466 & 0 & 0 & 0 \\
87.115 & 209.215 & 81.167 & 0 & 0 & 0 \\
87.466 & 81.167 & 209.215 & 0 & 0 & 0 \\
0 & 0 & 0 & 64.024 & 0 & 0 \\
0 & 0 & 0 & 0 & 67.002 & 0 \\
0 & 0 & 0 & 0 & 0 & 67.002
\end{bmatrix}
\tag{5.5.4}
$$

$$
\underbrace{\langle\langle \mathbb{C}_\epsilon \rangle\rangle}_{\nu_f=0.3} =
\begin{bmatrix}
205.972 & 61.719 & 61.419 & 0 & 0 & 0 \\
61.719 & 147.066 & 58.665 & 0 & 0 & 0 \\
61.419 & 58.665 & 147.066 & 0 & 0 & 0 \\
0 & 0 & 0 & 44.200 & 0 & 0 \\
0 & 0 & 0 & 0 & 45.689 & 0 \\
0 & 0 & 0 & 0 & 0 & 45.689
\end{bmatrix}
\tag{5.5.5}
$$

$$
\underbrace{\langle\langle \mathbb{C}_\epsilon \rangle\rangle}_{\nu_f=0.1} =
\begin{bmatrix}
130.594 & 46.031 & 45.995 & 0 & 0 & 0 \\
46.031 & 108.075 & 45.361 & 0 & 0 & 0 \\
45.995 & 45.361 & 108.075 & 0 & 0 & 0 \\
0 & 0 & 0 & 31.357 & 0 & 0 \\
0 & 0 & 0 & 0 & 32.083 & 0 \\
0 & 0 & 0 & 0 & 0 & 32.083
\end{bmatrix}
\tag{5.5.6}
$$

5.6 Comparison with Analytical Bounds

In this section we compare the results from the numerical RVE experiments to the Voigt-Reuss bounds and the Hashin-Rosen bounds described in Chapter.4.5. The converged elasticity tensor results for each fiber volume fraction are used to extract traditional material constants as described in Chapter. 2. We look at the results for E_{11}, E_{22}, μ_{12}, μ_{23} and ν_{12} which are shown in Figure. 5.14. We observe that for E_{11} the numerical RVE results match the upper bound exactly and for ν_{12} the bounds are all equivalent with the numerical results matching. On the other hand, the numerical results for the remaining components lie in
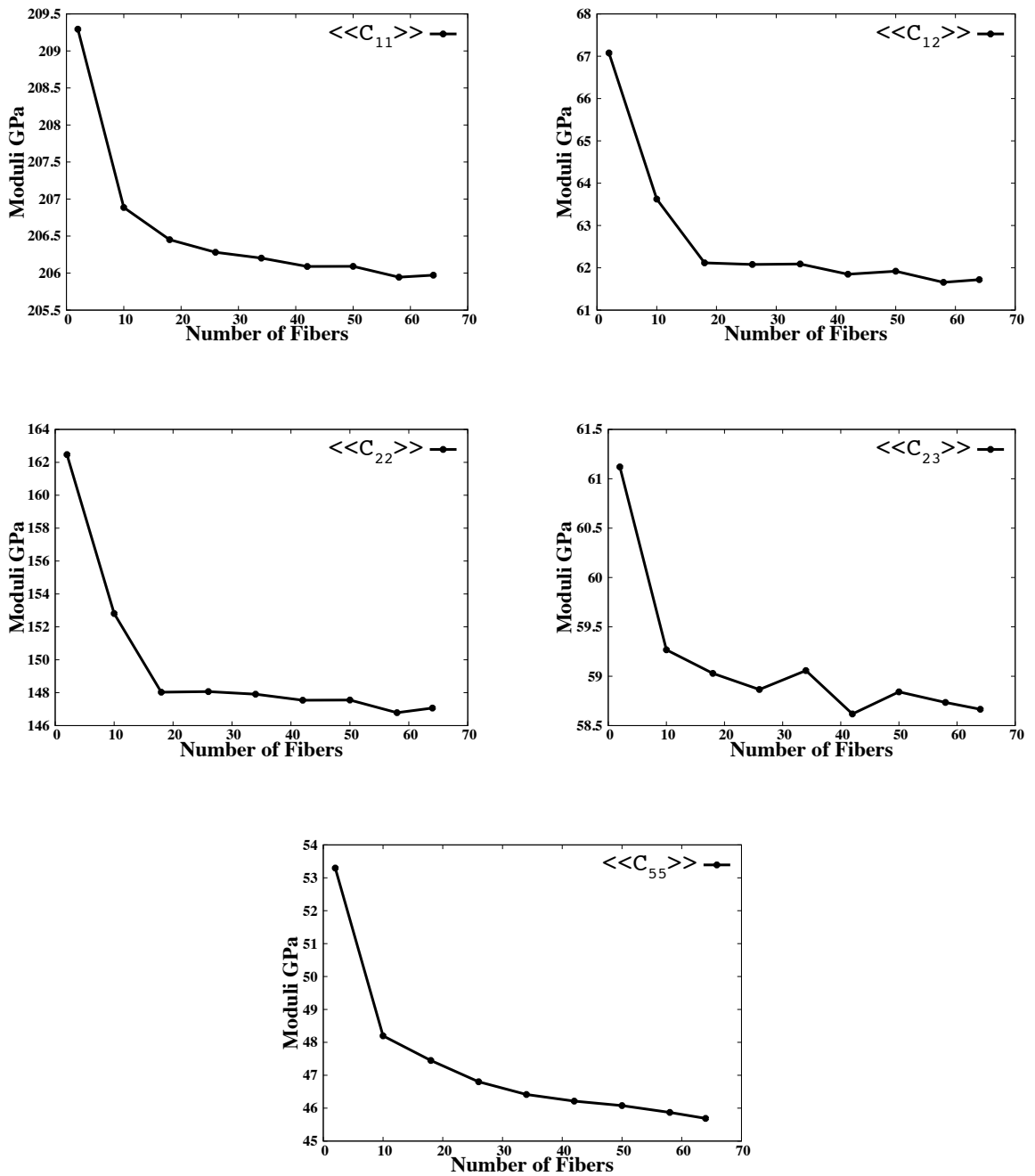
Figure 5.12: Effect of RVE size on properties for $\nu_f = 0.3$. The plots show how the five independent material properties change as a function of the RVE size. The properties converge after a certain RVE size.
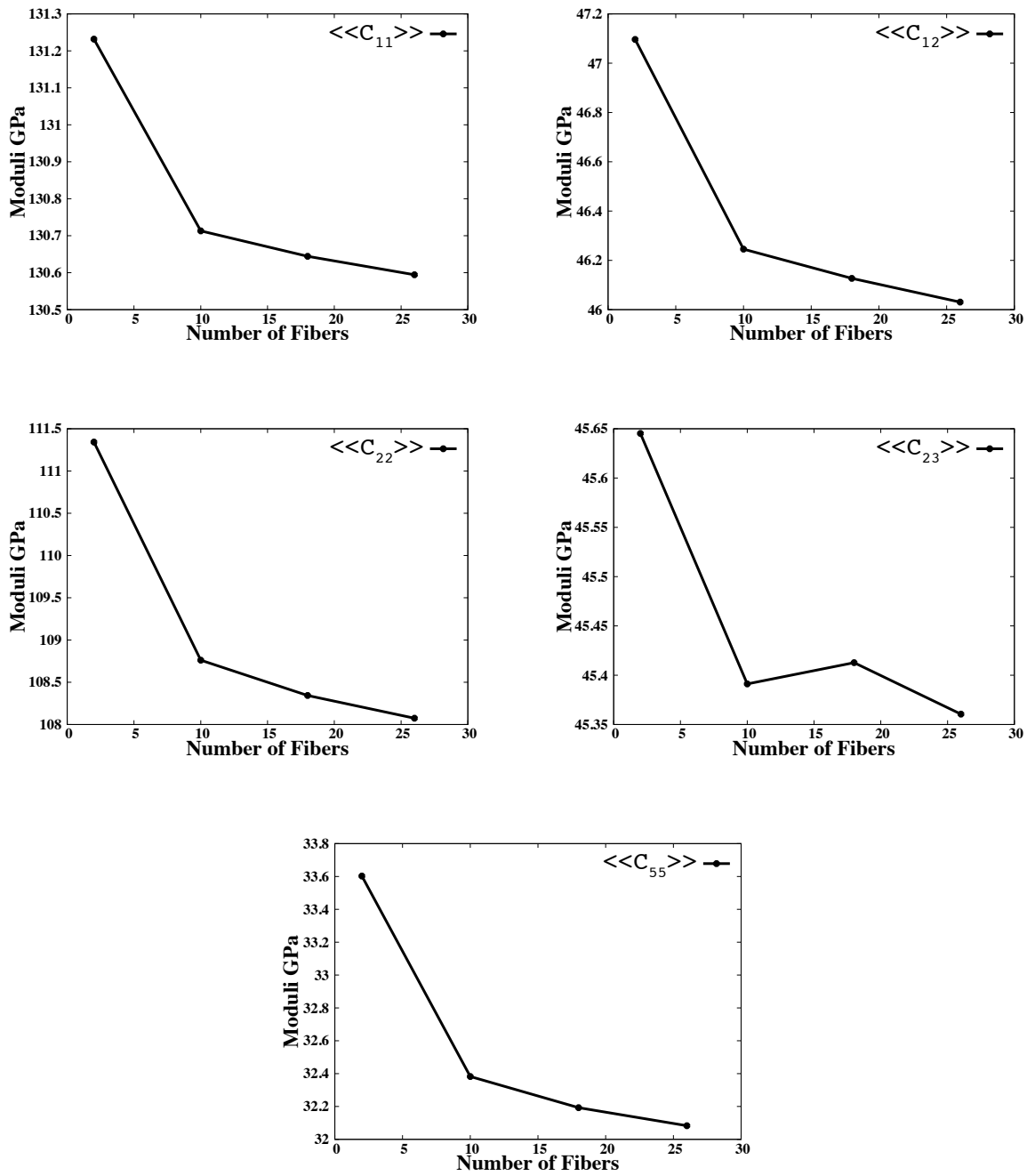
Figure 5.13: Effect of RVE size on properties for $\nu_f = 0.1$. The plots show how the five independent material properties change as a function of the RVE size. The properties converge after a certain RVE size.

between the tighter bounds of Hashin-Rosen. This clearly shows the advantage of using numerical techniques to obtain the elasticity tensor as opposed to relying on analytical bounds.
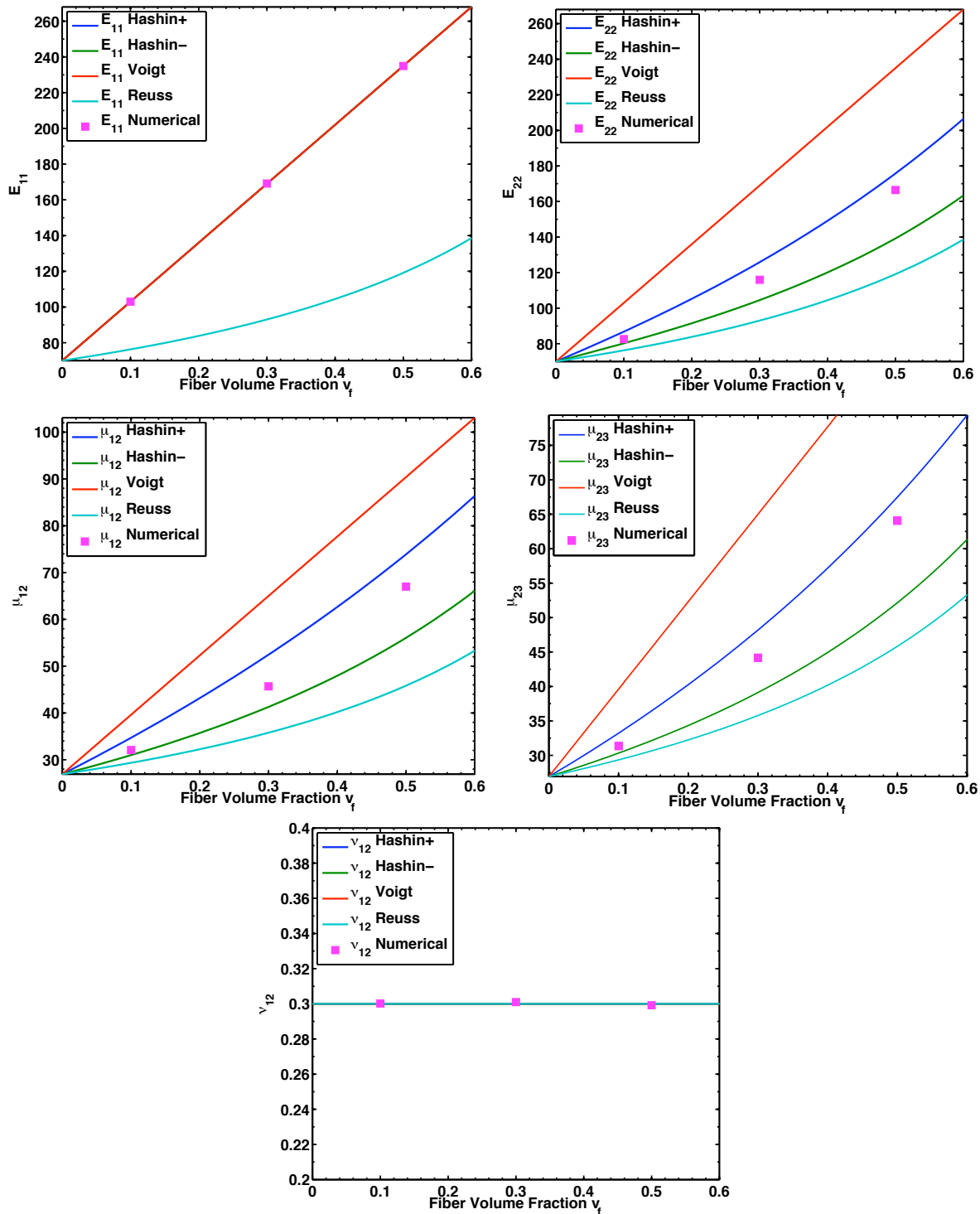
Figure 5.14: Analytical bounds and numerical results for the five independent material constants at different volume fractions. The material constants are in the form typical in Engineering(Young's modulus E_{11},E_{22}, Poison's ratio ν_{12} and shear modulus μ_{12}, μ_{23}). The analytical bounds include the Voigt-Reuss bounds and the Hashin-Rosen bounds. The Hashin-Rosen bounds are specifically for transversely isotropic materials and are clearly tighter than the traditional Voigt-Reuss bounds.

Chapter 6

Multiscale Modeling Introduction

In this chapter a description of the multiscale modeling analysis is presented for linear elasticity. Many of the traditional approaches for multiscale modeling have been based on asymptotic methods as described in Bensoussan. [5]. This approach relies on the assumption that the solution and microstructure are periodic. It allows for the the extraction of the macroproperties and provides a connection between the scales simultaneously. For further details the reader is referred to Zienkiewicz and Taylor. [38], Chung et al. [8], Ghosh et al. [10] and Fish et al. [6]. The disadvantages with this method is the dependence on the existence of a periodic structure which is generally not true for heterogeneous materials. These methods and others rely on RVE's being defined and solved at each gauss point, which can be extremely expensive.

Therefore, we want a method that is computationally efficient while being able to effectively account for the microstructural effects. Since solving the true heterogeneous problem is intractable, we start by first homogenizing as an independent process as described in Chapter. 4. We will assume that we know the microstructure a priori, this can be periodic or random. In our specific case, we will limit our interest to the analysis fiber composites. Hence, the position of the fibers in the matrix are known. The structure is then broken into subdomains that include the microstructural details. This is illustrated in Figure. 6.1. The method will then allow us to choose the subdomains that need to be included in the solution space. To this end error bounds that define a modeling error, in an a posterior setting, are derived from residual techniques in an analogous fashion to what has been done for error analysis in the finite element solution. For a complete review of error

analysis in the finite element method the reader is referred to Ainsworh and Oden. [39]. This initial bound illustrates the sources of error however, it's not suitable for computations. Therefore, for further analysis use is made of error bounds derived in Zohdi et al. [16]. These bounds are extended for use under finite deformations.
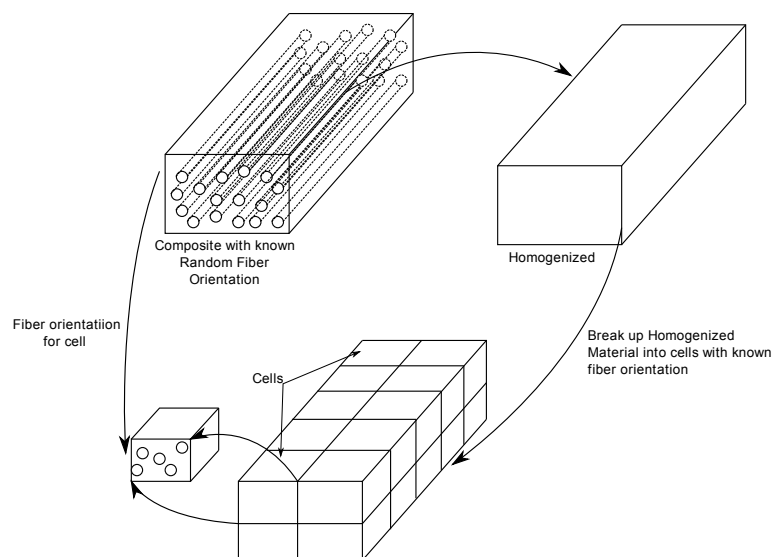
Figure 6.1: Schematic of multiscale approach showing the true heterogeneous body with fibers and then a homogenized body. The homogenized material is shown to be broken up in subdomains(cells) with fiber information based on the original heterogeneous body

6.1 Mathematical Setup: Global Problem

6.1.1 Setting Up The Exact Heterogeneous Boundary Value Problem

We start first by defining the exact boundary value problem with a known microstructure. The governing equations for the linear elastostatic case in the weak form are

$$\text{Find } \mathbf{u} \in H^1(\Omega), \mathbf{u}|_{\Gamma_u} = \mathbf{d}, \text{where } \forall \mathbf{v} \in H^1(\Omega), \mathbf{v}|_{\Gamma_u} = 0$$

$$\mathcal{B}(\mathbf{u}, \mathbf{v}) = \mathcal{F}(\mathbf{v}) \tag{6.1.1}$$

This defines the weak form of the balance of linear momentum, note we make use of the bilinear form for simplicity. Specifically, we have

$$\mathcal{B}(\mathbf{u}, \mathbf{v}) = \int_{\Omega} \nabla \mathbf{u} : \mathbb{C} : \nabla \mathbf{v} d\Omega \quad , \quad \mathcal{F}(\mathbf{v}) = \int_{\Omega} \mathbf{f} \cdot \mathbf{v} d\Omega + \int_{\Gamma_t} \mathbf{t} \cdot \mathbf{v} d\Gamma \tag{6.1.2}$$

Consider $\mathbf{u}$ to be the exact solution of the boundary value problem with a known microstructure and spatially varying material properties $\mathbb{C}(\mathbf{x})$. Since this is not computationally or analytically tractable, we resort to homogenization.

6.1.2 Setting Up The Exact and Numerical Homogenous Boundary Value Problem

The homogenized solution is characterized by a spatially constant material property $\mathbb{C}^*$ with solution $\mathbf{u}^*$. This can be characterized by the weak form or the principle of virtual work as

$$\text{Find } \mathbf{u}^* \in H^1(\Omega), \mathbf{u}^*|_{\Gamma_u} = \mathbf{d}, \text{where } \forall \mathbf{v} \in H^1(\Omega), \mathbf{v}|_{\Gamma_u} = 0$$
$$\mathcal{B}^*(\mathbf{u}^*, \mathbf{v}) = \mathcal{F}(\mathbf{v}) \tag{6.1.3}$$

with the bilinear forms defined as

$$\mathcal{B}^*(\mathbf{u}^*, \mathbf{v}) = \int_{\Omega} \nabla \mathbf{u}^* : \mathbb{C}^* : \nabla \mathbf{v} d\Omega, \quad \mathcal{F}(\mathbf{v}) = \int_{\Omega} \mathbf{f} \cdot \mathbf{v} d\Omega + \int_{\Gamma_t} \mathbf{t} \cdot \mathbf{v} d\Gamma \tag{6.1.4}$$

Solving this analytically would also be very difficult, we therefore resort to the finite element method and approximate the solution $\mathbf{u}^*$ as $\mathbf{u}^{*,h}$, which has a weak form as follows

$$\text{Find } \mathbf{u}^{*,h} \in H_u^1(\Omega) \subset H^1(\Omega), \mathbf{u}^{*,h}|_{\Gamma_u} = \mathbf{d}, \text{where } \forall \mathbf{v}^h \in H_v^1(\Omega) \subset H^1(\Omega), \mathbf{v}^h|_{\Gamma_u} = 0$$
$$\mathcal{B}^*(\mathbf{u}^{*,h}, \mathbf{v}^h) = \mathcal{F}(\mathbf{v}^h) \tag{6.1.5}$$

Specifically, the expression of the bilinear forms are

$$\mathcal{B}^*(\mathbf{u}^{*,h}, \mathbf{v}^h) = \int_\Omega \nabla \mathbf{u}^{*,h} : \mathbb{C}^* : \nabla \mathbf{v}^h d\Omega, \ \ \mathcal{F}(\mathbf{v}^h) = \int_\Omega \mathbf{f} \cdot \mathbf{v}^h d\Omega + \int_{\Gamma_t} \mathbf{t} \cdot \mathbf{v}^h d\Gamma \quad (6.1.6)$$

When approximating our initial problem defined in Eqn. 6.1.1 with Eqn. 6.1.5, we must estimate the error to obtain an understanding of the accuracy of our homogenized solution relative to the exact problem that includes the microstructure. The error analysis is presented in the next section and involves using the residuals from the balance of linear momentum or the local form of the weak equations that are solved using FEM.

6.1.3 Modeling Error Analysis

Consider the two boundary value problems shown in Figure. 6.2 and whose governing equations were described in Eqns. 6.1.1-6.1.3. In conducting the error analysis we are trying to approximate the following

$$\text{error} = ||\mathbf{u} - \mathbf{u}^{*,h}||_{E(\Omega)} \quad (6.1.7)$$

where $|| \cdot ||_{E(\Omega)}$ is the energy norm defined as

$$|| \cdot ||_{E(\Omega)}^2 = \int_\Omega \nabla(\cdot) : \mathbb{C} : \nabla(\cdot) d\Omega \quad (6.1.8)$$

Note, that the above error can be deconstructed into two parts. The first part is an error on the modeling component and the second part is an error on the numerical component. In other words we have

$$||\mathbf{u} - \mathbf{u}^{*,h}||_{E(\Omega)} = ||\mathbf{u} - \mathbf{u}^* + \mathbf{u}^* - \mathbf{u}^{*,h}||_{E(\Omega)}$$
$$\leq \underbrace{||\mathbf{u} - \mathbf{u}^*||_{E(\Omega)}}_{\text{Modeling Error}} + \underbrace{||\mathbf{u}^* - \mathbf{u}^{*,h}||_{E(\Omega)}}_{\text{Numerical Error}} \quad (6.1.9)$$

where our main interest here is to understand the modeling error. The numerical error component has been discussed in detail in the literature with a comprehensive review found

in Ainsworth and Oden. [39].

$$\text{div}(\boldsymbol{\sigma}) + \mathbf{f} = 0$$
$$\mathbf{t} = \mathbf{t}_a \ \text{ on } \ \Gamma_{\mathbf{t}}$$
$$\mathbf{u} = \mathbf{u}_a \ \text{ on } \ \Gamma_{\mathbf{u}}$$

$$\text{div}(\boldsymbol{\sigma}^*) + \mathbf{f} = 0$$
$$\mathbf{t}^* = \mathbf{t}_a \ \text{ on } \ \Gamma_{\mathbf{t}}$$
$$\mathbf{u}^* = \mathbf{u}_a \ \text{ on } \ \Gamma_{\mathbf{u}}$$
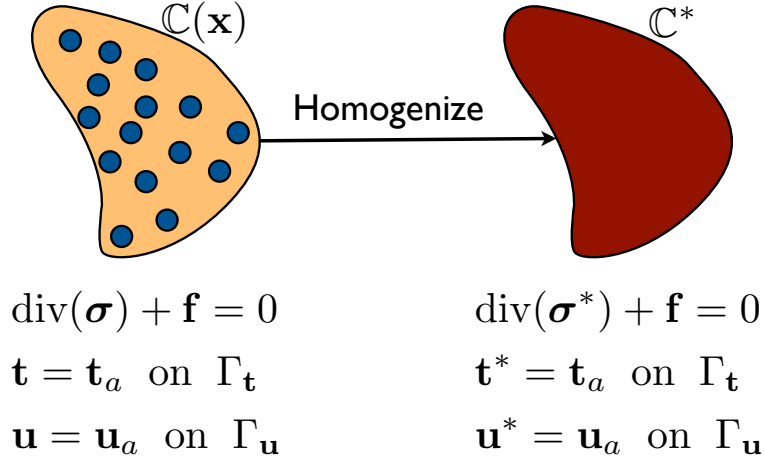
Figure 6.2: Schematic of both the heterogeneous and homogenous bodies with their corresponding boundary value problem

To better understand the modeling error component, we take the solution from the homogenized system($\mathbf{u}^*$) and calculate the small strain tensor, $\boldsymbol{\epsilon}^*$ and then define a stress $\boldsymbol{\sigma}^m = \mathbb{C} : \boldsymbol{\epsilon}^*$. We can also define the traction as $\mathbf{t}^m = \boldsymbol{\sigma}^m \mathbf{n}$. Note the stress is computed with the exact material properties, not the homogenized properties that were used to solve Eqn. 6.1.3. We can now check to see how well this stress state satisfies both the local form of the balance of linear momentum and the traction boundary condtion, specifically

$$\text{div}(\boldsymbol{\sigma}^m) + \mathbf{f} = \mathbf{r}^m$$
$$\mathbf{t} - \mathbf{t}^m = \hat{\mathbf{t}} \quad \text{on} \quad \Gamma_t \tag{6.1.10}$$

where $\mathbf{r}^m$ is the residual and $\hat{\mathbf{t}}$ is the mismatch in the traction boundary condition. Note that as $\boldsymbol{\epsilon}^* \to \boldsymbol{\epsilon}$, $\mathbf{r}^m \to 0$.. Therefore, we can interpret $\mathbf{r}^m$ and $\hat{\mathbf{t}}$ as the error between the heterogeneous solution and the homogenous solution. Particularly, it is an estimate on the modeling error. To add mathematical rigor to this interpretation, we derive a relationship between the modeling error defined in Eqn. 6.1.9 and Eqn. 6.1.10. To start we subtract the balance of linear momentum portion of Eqn. 6.1.10 from the local form of Eqn . 6.1.1, which is $\text{div}(\boldsymbol{\sigma}) + \mathbf{f} = 0$ with $\mathbf{t} = \mathbf{t}_a$ on Γ_t and $\mathbf{u} = \mathbf{u}_a$ on Γ_u. The result is

$$\text{div}(\boldsymbol{\sigma} - \boldsymbol{\sigma}^m) + \mathbf{r}^m = 0$$
$$\text{div}(\mathbb{C} : (\boldsymbol{\epsilon} - \boldsymbol{\epsilon}^*)) + \mathbf{r}^m = 0 \qquad (6.1.11)$$
$$\text{div}(\hat{\boldsymbol{\sigma}}) + \mathbf{r}^m = 0$$

Then we multiply Eqn. 6.1.11 by the test function $\mathbf{v}$ used to get the weak forms in Eqn. 6.1.1-6.1.3 and integrate over the volume, such that

$$\int_{\Omega} (\text{div}(\hat{\boldsymbol{\sigma}}) + \mathbf{r}^m) \cdot \mathbf{v} d\Omega = 0 \qquad (6.1.12)$$

We utilize the divergence theorem and obtain the form

$$\int_{\Omega} \nabla \mathbf{v} : \mathbb{C} : \nabla(\mathbf{u} - \mathbf{u}^*) d\Omega = \int_{\Gamma_t} \hat{\mathbf{t}} \cdot \mathbf{v} d\Gamma + \int_{\Omega} \mathbf{r}^m \cdot \mathbf{v} d\Omega \qquad (6.1.13)$$

We note that on Γ_u, as previously stated $\mathbf{v} = 0$. Additionally, $\hat{\mathbf{t}} = \mathbf{t} - \mathbf{t^m} = (\boldsymbol{\sigma} - \boldsymbol{\sigma^m})\mathbf{n}$. Observe that the difference between these two traction's is not zero. This is specifically because, $\mathbf{t}$ is the imposed traction while $\mathbf{t}^m$ is the arising traction due to the mismatch between the solutions $\mathbf{u}$ and $\mathbf{u}^*$. Consider the case when $\mathbf{v} = \mathbf{u} - \mathbf{u}^*$ we obtain

$$\begin{aligned}
\int_{\Omega} \nabla \mathbf{v} : \mathbb{C} : \nabla(\mathbf{u} - \mathbf{u}^*) d\Omega &= \int_{\Omega} \nabla(\mathbf{u} - \mathbf{u}^*) : \mathbb{C} : \nabla(\mathbf{u} - \mathbf{u}^*) d\Omega \\
&= B(\mathbf{u} - \mathbf{u}^*, \mathbf{u} - \mathbf{u}^*) \\
&= ||\mathbf{u} - \mathbf{u}^*||_E^2 \\
&= \int_{\Gamma_t} \hat{\mathbf{t}} \cdot (\mathbf{u} - \mathbf{u}^*) d\Gamma + \int_{\Omega} \mathbf{r}^m \cdot (\mathbf{u} - \mathbf{u}^*) d\Omega
\end{aligned} \qquad (6.1.14)$$

We now have the modeling error described in terms of the residual $\mathbf{r}^m$ and the mismatch in the tractions. We further simplify this expression by considering the Cauchy-Schwarty inequality, leading to the following

$$\|\mathbf{u} - \mathbf{u}^*\|_E^2 = \int_{\Gamma_t} \hat{\mathbf{t}} \cdot (\mathbf{u} - \mathbf{u}^*) d\Gamma + \int_\Omega \mathbf{r}^m \cdot (\mathbf{u} - \mathbf{u}^*) d\Omega$$
$$\leq \|\mathbf{r}^m\|_{L_2(\Omega)} \|\mathbf{u} - \mathbf{u}^*\|_{L_2(\Omega)} + \|\mathbf{t} - \mathbf{t}^m\|_{L_2(\Gamma_t)} \|\mathbf{u} - \mathbf{u}^*\|_{L_2(\Gamma_t)} \tag{6.1.15}$$

We note that $\|\cdot\|_{L_2(\Omega)} = \int_\Omega (\cdot) \cdot (\cdot) d\Omega$ and is called the L_2 norm. In Eqn. 6.1.15, we have an expression for the modeling error that states that as $\mathbf{r}^m \to 0$ and the jump in tractions $\hat{\mathbf{t}} \to 0$ then the difference in the heterogenous and homogeneous solution is zero.

However, we note that error estimates derived depend on the analytical solutions. Since we cannot calculate these solutions we refer to the FEM solution of the homogenized problem. This is detailed in the next section.

6.1.4 Modeling Error Calculation on a Finite Element

We now extend our error definition in Eqn. 6.1.15 to be calculated on a finite element. Recall that the finite element solution of the homogenized boundary value problem was defined in Eqn. 6.1.5, with solution $\mathbf{u}^{*,h}$. To calculate our modeling error we utilize an expression that includes the numerical solution of the homogenized boundary value problem. This can be expressed as,

$$\|\mathbf{u} - \mathbf{u}^{*,h}\|_{E(\Omega)}^2 = \int_\Omega \nabla(\mathbf{u} - \mathbf{u}^{*,h}) : \mathbb{C} : \nabla(\mathbf{u} - \mathbf{u}^{*,h}) d\Omega \tag{6.1.16}$$

Recall this is the total error defined in Eqn. 6.1.16. It includes both the modeling an numerical error. Neglecting body load effects and referring to Ainsworth and Oden. [39] we can express on an element basis the total error as

$$B(\mathbf{u} - \mathbf{u}^{*,h}, \mathbf{v}) = B(\mathbf{e}, \mathbf{v}) = B(\mathbf{u}, \mathbf{v}) - B(\mathbf{u}^{*,h}, \mathbf{v})$$
$$= \mathcal{F}(\mathbf{v}) - B(\mathbf{u}^{*,h}, \mathbf{v})$$
$$= \sum_K^{Ne} \left\{ \int_{\partial K \cap \Gamma_t} \mathbf{t} \cdot \mathbf{v} d\Gamma - \int_K \nabla \mathbf{u}^{*,h} : \mathbb{C} : \nabla \mathbf{v} d\Omega \right\} \tag{6.1.17}$$

where K a finite element and ∂K is the boundary of the element. We can restructure the

last term in the above equation by utilizing $\nabla(\mathbb{C} : \nabla\mathbf{u}^{*,h} \cdot \mathbf{v}) = \nabla\boldsymbol{\sigma}^{m,h} \cdot \mathbf{v} + \boldsymbol{\sigma}^{m,h} : \nabla\mathbf{v} = \nabla\boldsymbol{\sigma}^{m,h} \cdot \mathbf{v} + \nabla\mathbf{u}^{*,h} : \mathbb{C} : \nabla\mathbf{v}$. Therefore, Eqn. 6.1.17 becomes

$$B(\mathbf{e}, \mathbf{v}) = \sum_K^{Ne} \left\{ \int_{\partial K \cap \Gamma_t} \mathbf{t} \cdot \mathbf{v} d\Gamma - \int_K \left(\nabla(\mathbb{C} : \nabla\mathbf{u}^{*,h} \cdot \mathbf{v}) - \nabla\boldsymbol{\sigma}^{m,h} \cdot \mathbf{v} \right) d\Omega \right\} \qquad (6.1.18)$$

upon utilizing the divergence theorem we obtain

$$\begin{aligned} B(\mathbf{e}, \mathbf{v}) &= \sum_K^{Ne} \left\{ \int_{\partial K \cap \Gamma_t} \mathbf{t} \cdot \mathbf{v} d\Gamma - \int_{\partial K} \mathbb{C} : \nabla\mathbf{u}^{*,h} \cdot \mathbf{v} \cdot \mathbf{n}_K + \int_K \nabla\boldsymbol{\sigma}^{m,h} \cdot \mathbf{v} d\Omega \right\} \\ &= \sum_K^{Ne} \left\{ \int_{\partial K \cap \Gamma_t} \mathbf{t} \cdot \mathbf{v} d\Gamma - \int_{\partial K} \boldsymbol{\sigma}^{m,h} \mathbf{n}_K \cdot \mathbf{v} d\Gamma + \int_K \nabla\boldsymbol{\sigma}^{m,h} \cdot \mathbf{v} d\Omega \right\} \qquad (6.1.19) \\ &= \sum_K^{Ne} \left\{ \int_{\partial K \cap \Gamma_t} \mathbf{t} \cdot \mathbf{v} d\Gamma - \int_{\partial K} \mathbf{t}^{m,h}(\mathbf{n}_K) \cdot \mathbf{v} d\Gamma + \int_K \nabla\boldsymbol{\sigma}^{m,h} \cdot \mathbf{v} d\Omega \right\} \end{aligned}$$

We can break the integral on ∂K into two parts. One for elements in the interior of the domain Ω and the other on the boundary $\partial \Omega$ such that

$$B(\mathbf{e}, \mathbf{v}) = \sum_K^{Ne} \left\{ \int_{\partial K \cap \Gamma_t} \left(\mathbf{t} - \mathbf{t}^{m,h}(\mathbf{n}_K) \right) \cdot \mathbf{v} d\Gamma - \int_{\partial K / \Gamma_t} \mathbf{t}^{m,h}(\mathbf{n}_K) \cdot \mathbf{v} d\Gamma + \int_K \nabla \cdot \boldsymbol{\sigma}^{m,h} \cdot \mathbf{v} d\Omega \right\}$$
$$(6.1.20)$$

This form gives an expression for the total error, all the terms inside the integral are known except for $\mathbf{v}$. We will come to this later. First we can rearrange the second term by breaking up the element surface integral over the sum of the individual surface integrals. For instance, in a three dimensional brick element there are 6 surfaces hence,

$$\int_{\partial K / \Gamma_t} \mathbf{t}^{m,h}(\mathbf{n}_K) \cdot \mathbf{v} d\Gamma = \sum_{\gamma=1}^{6} \left(\int_\gamma \mathbf{t}^{m,h}(\mathbf{n}_K) \cdot \mathbf{v} d\gamma \right) \qquad (6.1.21)$$

Since each surface is shared by two elements we can calculate a jump in the traction's over each element surface where we have

$$\sum_{K}^{Ne} \int_{\partial K/\Gamma_t} \mathbf{t}^{m,h}(\mathbf{n}_K) \cdot \mathbf{v} d\Gamma = \sum_{K}^{Ne} \sum_{\gamma=1}^{6} \left(\int_\gamma \frac{1}{2} \left(\mathbf{t}^{m,h}(\mathbf{n}_K) + \mathbf{t}^{m,h}(\mathbf{n}_J) \right) \cdot \mathbf{v} d\gamma \right)$$

$$= \sum_{K}^{Ne} \sum_{\gamma=1}^{6} \left(\int_\gamma \frac{1}{2} [\mathbf{t}^{m,h}] \cdot \mathbf{v} d\gamma \right) \qquad (6.1.22)$$

$$= \sum_{K}^{Ne} \int_{K/\Gamma_t} \frac{1}{2} [\mathbf{t}^{m,h}] \cdot \mathbf{v} d\Gamma$$

where element K and J share surface γ_i and $[\cdot]$ indicates the jump . We can utilize the Cauchy-Schwarty inequality and obtain

$$B(\mathbf{e}, \mathbf{v}) \leq \sum_{K}^{Ne} \left\{ ||\mathbf{t} - \mathbf{t}^{m,h}(\mathbf{n}_K)||_{L_2(\partial K \cap \Gamma_t)} ||\mathbf{v}||_{L_2(\partial K \cap \Gamma_t)} \right. $$
$$\left. + ||[\mathbf{t}^{m,h}]||_{L_2(\partial K/\Gamma_t)} ||\mathbf{v}||_{L_2(\partial K/\Gamma_t)} + ||\nabla \cdot \boldsymbol{\sigma}^{m,h}||_{L_2(K)} ||\mathbf{v}||_{L_2(K)} \right\} \qquad (6.1.23)$$

replacing $\mathbf{v}$ with $\mathbf{e}$ we have

$$||\mathbf{u} - \mathbf{u}^{*,h}||_E^2 = B(\mathbf{e}, \mathbf{e})$$
$$\leq \sum_{K}^{Ne} \left\{ ||\mathbf{t} - \mathbf{t}^{m,h}(\mathbf{n}_K)||_{L_2(\partial K \cap \Gamma_t)} ||\mathbf{e}||_{L_2(\partial K \cap \Gamma_t)} \right. \qquad (6.1.24)$$
$$\left. + ||[\mathbf{t}^{m,h}]||_{L_2(\partial K/\Gamma_t)} ||\mathbf{e}||_{L_2(\partial K/\Gamma_t)} + ||\nabla \cdot \boldsymbol{\sigma}^{m,h}||_{L_2(K)} ||\mathbf{e}||_{L_2(K)} \right\}$$

We would like norms of the error on the right hand side to be moved to the left side. To accomplish this we must find bounds from above on these terms with respect to the energy norm. This can be done by utilizing some aspects of functional analysis of which a thorough discussion is presented in Oden and Demkowicz. [40]. We will utilize some key concepts to achieve the desired bound. Specifically, there are two norms that need to be bounded. The first is $|| \cdot ||_{L_2(\Omega)}$ which is L_2 defined in the domain Ω. The second is $|| \cdot ||_{L_2(\Gamma)}$ which is the L_2 norm defined on the boundary of the domain Γ.

Consider the first norm, we can utilize the properties of the bilinear form to obtain an upper bound. The properties are

1. B is continuous such that there is a constant $C > 0$

$$B(\mathbf{u}, \mathbf{v}) \leq C||\mathbf{u}||||\mathbf{v}|| \quad \mathbf{u}, \mathbf{v} \in H^m(\Omega)$$

2. B is coercive or ellipitic such that there is a contant $\alpha > 0$

$$B(\mathbf{u}, \mathbf{u}) \geq \alpha||\mathbf{u}||^2 \quad \forall \mathbf{u} \in H^m(\Omega)$$

By utilizing the coercivity property for case when $\mathbf{u} \in H^1(\Omega)$ we have

$$
\begin{aligned}
||\mathbf{u}||_E^2 = B(\mathbf{u}, \mathbf{u}) &\geq \alpha||\mathbf{u}||_{H^1(\Omega)}^2 \\
&= \alpha(||\mathbf{u}||_{L_2(\Omega)}^2 + ||\mathbf{u}'||_{L_2(\Omega)}^2) \\
&\geq \alpha||\mathbf{u}||_{L_2(\Omega)}^2
\end{aligned}
\tag{6.1.25}
$$

Therefore, we have the following upper bound on the error $||\mathbf{e}||_{L_2(\Omega)} \leq \frac{1}{\sqrt{\alpha}}||\mathbf{e}||_{E(\Omega)}$. The first question might be, what is the constant α? To approach this, we consider the fact that for linear elasticity the elasticity tensory $\mathbb{C}$ is positive definite and the energy is always greater than or equal to zero. Specifically, we have the following property on $\mathbb{C}$ $\forall \boldsymbol{\epsilon}$ there exists two constants $\alpha_L, \alpha_U \geq 0$

$$\alpha_L \boldsymbol{\epsilon} : \boldsymbol{\epsilon} \leq \boldsymbol{\epsilon} : \mathbb{C}(x)\boldsymbol{\epsilon} \leq \alpha_u \boldsymbol{\epsilon} : \boldsymbol{\epsilon} \tag{6.1.26}$$

because $\mathbb{C}$ is positive definite, it can readily be seen that from Eqn. 6.1.26 we have the following inequality

$$||\mathbf{e}||_{E(\Omega)}^2 \geq \alpha_L||\nabla \mathbf{e}||_{L_2(\Omega)}^2 \tag{6.1.27}$$

and considering the Poincare inequality $||\mathbf{e}||_{L_2(\Omega)}^2 \leq C_1||\nabla \mathbf{e}||_{L_2(\Omega)}^2$ we can obtain

$$\frac{1}{C_1}||\mathbf{e}||_{L_2(\Omega)}^2 \leq ||\nabla \mathbf{e}||_{L_2(\Omega)}^2 \leq \frac{1}{\alpha_L}||\mathbf{e}||_{E(\Omega)}^2 \tag{6.1.28}$$

and hence, we have

$$||\mathbf{e}||^2_{E(\Omega)} \geq \frac{\alpha_L}{C_1}||\mathbf{e}||^2_{L_2(\Omega)} \tag{6.1.29}$$

This is the bound we obtained using the ellipticity property, the only advantage is this clarifies the meaning of the constant α, where C_1 is a length scale of the body and α_L can be obtained exactly by starting with the lower bound statement on the elasticity tensor and rearranging to get

$$\begin{aligned}0 &\leq \boldsymbol{\epsilon} : (\mathbb{C}(x) - \alpha_L \mathbf{I})\,\boldsymbol{\epsilon} \\ &= \boldsymbol{\epsilon} : \mathbf{B}\boldsymbol{\epsilon}\end{aligned} \tag{6.1.30}$$

Hence, $\mathbf{B}$ must be positive semidefinite and therefore, it's eigenvalues must be nonnegative. We can therefore solve for α_L that satisfies this condition.

Now we consider the second norm in $L_2(\Gamma)$ on the boundary and find an upper bound in the energy norm on the open set defining the domain Ω. To construct this bound we utilize the trace theorem that is commonly used in functional analysis. The theorem is described extensively in [40],[41] and a proof is found in [41]. It states

Theorem 6.1.1 Trace Theorem. *Let Ω be bounded and assume Ω has a piecewise smooth boundary. Also, suppose Ω satisfies the cone condition. Then there exists a bounded linear mapping*

$$\gamma : H^1(\Omega) \to L_2(\Gamma), \quad ||\gamma(\nu)||_{L_2(\Gamma)} \leq C||\nu||_{H^1(\Omega)} \tag{6.1.31}$$

We can now use this theorem along with coercivity property such that

$$\begin{aligned}||\mathbf{e}||_{L_2(\Gamma)} &\leq C||\mathbf{e}||_{H^1(\Omega)} \\ &\leq \frac{C}{\sqrt{\alpha}}||\mathbf{e}||_{E(\Omega)}\end{aligned} \tag{6.1.32}$$

Hence, we have the bound $||\mathbf{e}||_{L_2(\Gamma)} \leq \frac{C}{\sqrt{\alpha}}||\mathbf{e}||_{E(\Omega)}$. We now obtain the following bound on

the error as

$$
||\mathbf{u} - \mathbf{u}^*||^2_{E(\Omega)} = B(\mathbf{e}, \mathbf{v})
$$

$$
\leq \sum_{K}^{Ne} \Big\{ ||\mathbf{t} - \mathbf{t}^{m,h}(\mathbf{n}_K)||_{L_2(\partial K \cap \Gamma_t)} ||\mathbf{e}||_{L_2(\partial K \cap \Gamma_t)}
$$

$$
+ ||[\mathbf{t}^{m,h}]||_{L_2(\partial K / \Gamma_t)} ||\mathbf{e}||_{L_2(\partial K / \Gamma_t)} + ||\nabla \cdot \boldsymbol{\sigma}^{m,h}||_{L_2(K)} ||\mathbf{e}||_{L_2(\Omega)} \Big\} \qquad (6.1.33)
$$

$$
\leq \sum_{K}^{Ne} \Big\{ ||\mathbf{t} - \mathbf{t}^{m,h}(\mathbf{n}_K)||_{L_2(\partial K \cap \Gamma_t)} \frac{C}{\sqrt{\alpha}} ||\mathbf{e}||_{E(K)}
$$

$$
+ ||[\mathbf{t}^{m,h}]||_{L_2(\partial K / \Gamma_t)} \frac{C}{\sqrt{\alpha}} ||\mathbf{e}||_{E(K)} + ||\nabla \cdot \boldsymbol{\sigma}^{m,h}||_{L_2(K)} \frac{1}{\sqrt{\alpha}} ||\mathbf{e}||_{E(K)} \Big\}
$$

Applying the cauchy-schwartz inequality again gives us the following

$$
||\mathbf{e}||^2_{E(\Omega)} \leq \sqrt{\sum_{K}^{Ne} \frac{C^2}{\alpha} ||\mathbf{t} - \mathbf{t}^{m,h}(\mathbf{n}_K)||^2_{L_2(\partial K \cap \Gamma_t)} \sum_{K}^{Ne} ||\mathbf{e}||^2_{E(K)}}
$$

$$
+ \sqrt{\sum_{K}^{Ne} \frac{C^2}{\alpha} ||[\mathbf{t}^{m,h}]||^2_{L_2(\partial K / \Gamma_t)} \sum_{K}^{Ne} ||\mathbf{e}||^2_{E(K)}} + \sqrt{\sum_{K}^{Ne} \frac{1}{\alpha} ||\nabla \cdot \boldsymbol{\sigma}^{m,h}||^2_{L_2(K)} \sum_{K}^{Ne} ||\mathbf{e}||^2_{E(K)}}
$$

$$
(6.1.34)
$$

Now takeing out the common factor $\sum_{K}^{Ne} ||\mathbf{e}||^2_{E(K)}$ and noting that $\sum_{K}^{Ne} ||\mathbf{e}||^2_{E(K)} = ||\mathbf{e}||^2_{E(\Omega)}$ we get

$$
||\mathbf{e}||_{E(\Omega)} \leq \sqrt{\sum_{K}^{Ne} \frac{C^2}{\alpha} ||\mathbf{t} - \mathbf{t}^{m,h}(\mathbf{n}_K)||^2_{L_2(\partial K \cap \Gamma_t)}}
$$

$$
(6.1.35)
$$

$$
+ \sqrt{\sum_{K}^{Ne} \frac{C^2}{\alpha} ||[\mathbf{t}^{m,h}]||^2_{L_2(\partial K / \Gamma_t)}} + \sqrt{\sum_{K}^{Ne} \frac{1}{\alpha} ||\nabla \cdot \boldsymbol{\sigma}^{m,h}||^2_{L_2(K)}}
$$

To get a more desirable expression we can proceed by using the identity $(\sqrt{a} + \sqrt{b})^2 \leq 2(a+b)$ and we obtain

$$\|\mathbf{e}\|_{E(\Omega)} \leq \sqrt{\sum_K^{Ne} \frac{C^2}{\alpha} \|\mathbf{t} - \mathbf{t}^{m,h}(\mathbf{n}_K)\|^2_{L_2(\partial K \cap \Gamma_t)}}$$

$$+ \sqrt{\sum_K^{Ne} \frac{C^2}{\alpha} \|[\mathbf{t}^{m,h}]\|^2_{L_2(\partial K/\Gamma_t)}} + \sqrt{\sum_K^{Ne} \frac{1}{\alpha} \|\nabla \cdot \boldsymbol{\sigma}^{m,h}\|^2_{L_2(K)}}$$

$$\leq \sqrt{\frac{2C^2}{\alpha} \sum_K^{Ne} \|\mathbf{t} - \mathbf{t}^{m,h}(\mathbf{n}_K)\|^2_{L_2(\partial K \cap \Gamma_t)} + \frac{2C^2}{\alpha} \sum_K^{Ne} \|[\mathbf{t}^{m,h}]\|^2_{L_2(\partial K/\Gamma_t)}}$$

$$+ \sqrt{\sum_K^{Ne} \frac{1}{\alpha} \|\nabla \cdot \boldsymbol{\sigma}^{m,h}\|^2_{L_2(K)}}$$

$$\leq \left(\frac{4C^2}{\alpha} \sum_K^{Ne} \|\mathbf{t} - \mathbf{t}^{m,h}(\mathbf{n}_K)\|^2_{L_2(\partial K \cap \Gamma_t)} + \frac{4C^2}{\alpha} \sum_K^{Ne} \|[\mathbf{t}^{m,h}]\|^2_{L_2(\partial K/\ \Gamma_t)} \right.$$

$$\left. + \frac{2}{\alpha} \sum_K^{Ne} \|\nabla \cdot \boldsymbol{\sigma}^{m,h}\|^2_{L_2(K)} \right)^{1/2} \tag{6.1.36}$$

Hence we have the final form as,

$$\|\mathbf{e}\|^2_{E(\Omega)} \leq \frac{2}{\alpha} \left(\sum_K^{Ne} 2C^2 \|\mathbf{t} - \mathbf{t}^{m,h}(\mathbf{n}_K)\|^2_{L_2(\partial K \cap \Gamma_t)} + 2C^2 \|[\mathbf{t}^{m,h}]\|^2_{L_2(\partial K/\ \Gamma_t)} \right.$$

$$\left. + \|\nabla \cdot \boldsymbol{\sigma}^{m,h}\|^2_{L_2(K)} \right) \tag{6.1.37}$$

We now have a form of the error over a finite element that can be calculated from information we know. However, C and α are not known and they can be very hard to calculated. Nonetheless, this bound give insight about the sources of error. We have three terms that contribute to the error, they are 1) $\|\mathbf{t} - \mathbf{t}^{m,h}(\mathbf{n}_K)\|^2_{L_2(\partial K \cap \Gamma_t)}$ which is the difference in the applied traction and the resulting traction due to homogenization, 2) $\|\nabla \cdot \boldsymbol{\sigma}^{m,h}\|^2_{L_2(K)}$ which is the residual from the divergence of the stress resulting from the homogenized strain acting on the exact material properties and 3) $\|[\mathbf{t}^{m,h}]\|^2_{L_2(\partial K/\ \Gamma_t)}$ the jumps in tractions across the finite elements. The last source of error is not purely a modeling error, but rather a result of the finite element discretization. Recall, that the above error bound is for the total error in the system, both modeling and numerical contributions.

Finally the to get thse modeling error we must subtract the numerical error from this global term. This can be easily done, as their are many methods for calculating the numerical error defined in Eqn. 6.1.9. The finally term is

$$\underbrace{||\mathbf{u} - \mathbf{u}^*||_E}_{\text{Modeling Error}} \geq \underbrace{||\mathbf{u} - \mathbf{u}^{*,h}||_E}_{\text{Total error}} - \underbrace{||\mathbf{u}^* - \mathbf{u}^{*,h}||_E}_{\text{Numerical Error}} \tag{6.1.38}$$

As mentioned, since we cannot easily calculate the values of the constants in the bound in Eqn. 6.1.37 we utilize a different approach as described in the next section.

6.2 An Exact Upper Bound on The Modeling Error

An upper bound that is suitable for numerical studies has been presented in Zohdi et al. [16]-[17]. The form of the bound is given as

$$||\mathbf{u} - \mathbf{u}^*||_{E(\Omega)} \leq ||\mathcal{J}_0 \nabla \mathbf{u}^*||_{E(\Omega)} = \zeta \tag{6.2.1}$$

where

$$||\mathcal{J}_0 \nabla \mathbf{u}^*||^2_{E(\Omega)} = \int_\Omega (\mathbf{I} - \mathbb{C}^{-1}\mathbb{C}^*)\nabla \mathbf{u}^* : \mathbb{C}(\mathbf{I} - \mathbb{C}^{-1}\mathbb{C}^*)\nabla \mathbf{u}^* d\Omega \tag{6.2.2}$$

and $\mathcal{J}_0 = \mathbf{I} - \mathbb{C}^{-1}\mathbb{C}^*$. The proof is quite easy to show and proceeds by considering Eqn. 6.1.1 and Eqn. 6.1.3, with their respective definitions of the bilinear form. We can define an operator $\Delta\mathcal{B}(\cdot, \cdot)$ as

$$\begin{aligned} \Delta\mathcal{B}(\mathbf{u}^*, \mathbf{v}) &= \mathcal{B}(\mathbf{u}^*, \mathbf{v}) - \mathcal{B}^*(\mathbf{u}^*, \mathbf{v}) \\ &= \int_\Omega \nabla\mathbf{v} : (\mathbb{C} - \mathbb{C}^*)\nabla\mathbf{u}^* d\Omega \end{aligned} \tag{6.2.3}$$

We can now rewrite Eqn. 6.1.3 such that

$$\mathcal{B}^*(\mathbf{u}^*, \mathbf{v}) = \mathcal{B}(\mathbf{u}^*, \mathbf{v}) - \Delta\mathcal{B}(\mathbf{u}^*, \mathbf{v}) = \mathcal{F}(\mathbf{v}) = \mathcal{B}(\mathbf{u}, \mathbf{v}) \qquad (6.2.4)$$

this can be reformulated as

$$\mathcal{B}(\mathbf{u} - \mathbf{u}^*, \mathbf{v}) = -\Delta\mathcal{B}(\mathbf{u}^*, \mathbf{v}) \qquad (6.2.5)$$

Hence, letting $\mathbf{v} = \mathbf{u} - \mathbf{u}^*$ we get

$$
\begin{aligned}
||\mathbf{u} - \mathbf{u}^*||_{E(\Omega)}^2 &= -\Delta\mathcal{B}(\mathbf{u}^*, \mathbf{u} - \mathbf{u}^*) \\
&= -((\nabla(\mathbf{u} - \mathbf{u}^*), (\mathbb{C} - \mathbb{C}^*)\nabla\mathbf{u}^*) \\
&= -((\nabla(\mathbf{u} - \mathbf{u}^*), \mathbb{C}\mathbb{C}^{-1}(\mathbb{C} - \mathbb{C}^*)\nabla\mathbf{u}^*) \qquad (6.2.6) \\
&= -(\mathbb{C}^{1/2}(\nabla(\mathbf{u} - \mathbf{u}^*), \mathbb{C}^{1/2}\mathbb{C}^{-1}(\mathbb{C} - \mathbb{C}^*)\nabla\mathbf{u}^*) \\
&= -(\mathbb{C}^{1/2}(\nabla(\mathbf{u} - \mathbf{u}^*), \mathbb{C}^{1/2}\mathcal{J}_0\nabla\mathbf{u}^*)
\end{aligned}
$$

Now with the Cauchy-Schwarz inequality we get

$$
\begin{aligned}
||\mathbf{u} - \mathbf{u}^*||_{E(\Omega)}^2 &= -(\mathbb{C}^{1/2}(\nabla(\mathbf{u} - \mathbf{u}^*), \mathbb{C}^{1/2}\mathcal{J}_0\nabla\mathbf{u}^*) \\
&\leq [(\mathbb{C}^{1/2}\nabla(\mathbf{u} - \mathbf{u}^*), (\mathbb{C}^{1/2}\nabla(\mathbf{u} - \mathbf{u}^*)]^{1/2}[\mathbb{C}^{1/2}\mathcal{J}_0\nabla\mathbf{u}^*, \mathbb{C}^{1/2}\mathcal{J}_0\nabla\mathbf{u}^*]^{1/2} \quad (6.2.7) \\
&= ||\mathbf{u} - \mathbf{u}^*||_{E(\Omega)}||\mathcal{J}_0\nabla\mathbf{u}^*||_{E(\Omega)}
\end{aligned}
$$

we therefore have the proof for Eqn 7.0.7. This bound is amenable to computations and will be used to for the multiscale modeling of fiber composites.

6.3 Numerical Experiments

In this section some basic numerical experiments will be conducted to demonstrate the effectiveness of the upper bound defined in Eqn. 7.0.7. To start we will analyze two examples with different boundary conditions and various material properties. For simplicity the domain is a unit cube. The first example is a homogenous material with isotropic properties which are considered the exact material properties with solution $\mathbf{u}$. We then

construct problems with material properties that deviate from the exact material properties by some constant γ with solution $\mathbf{u}^*$. These two solutions are then compared and the errors bounds are calculated. The second example will involve comparisons between a homogeneous material and heterogeneous material with some known microstructure. Error bounds are calculated and compared to the exact error. Different homogenous material properties are explored.

6.3.1 Isotropic-Isotropic Comparisions

The purpose of these examples is to understand how good the bound in Eqn. 7.0.7 is in predicting the error. The simplest example is to consider two isotropic bodies, one that we consider to constitute the exact material with properties ($\mathbb{C}_1$) and an other with material properties that deviate from $\mathbb{C}_1$ by a constant γ. Hence, we have $\mathbb{C}_2 = \gamma\mathbb{C}_1$. Note that γ is restricted in such away that the elasticity tensor remains positive definite. This formulation allows us to solve both problems and get an exact error and compare to the one predicted by the bound in Eqn. 7.0.7. Two sets of boundary conditions are considered. The first is displacement control and the second is traction control. The mesh size for these examples is 21X21X21 as can be seen in Figure. 6.3. The material properties for $\mathbb{C}_1$ were $E = 70GPa, \nu = 0.3$, these were kept constant since they are being considered exact. The variation in material properties for $\mathbb{C}_2$ is then γE and $\gamma \nu$.

For the case of displacement control we specified at $x = 1$ that $u_x = 0.001m$, at $x = 0$ the displacements were fixed such that $\mathbf{u} = 0$ and the remaining directions are set move freely. For the case of traction control we specified at $x = 1$ that $t_x = 0.1$GPa and on $x = 0$ the displacements were fixed.

For a given set of boundary conditions t=0.1GPa and $\gamma = 1.3$ the deformed shape and the predicted error are shown in Figure. 6.4. The deformed shape is exaggerated to see the deformation.

The results from the tests are summarized in Figure. 6.5, which show both the predicted error $\frac{\zeta}{||\mathbf{u}^{*,h}||_{E(\Omega)}}$ and the exact error $\frac{||\mathbf{u}^h - \mathbf{u}^{*,h}||_{E(\Omega)}}{||\mathbf{u}^{*,h}||_{E(\Omega)}}$ vs the factor γ. The plots show that for the case of traction control the exact error and the predicted error match almost exactly, while under displacement control the predicted error is a true upper bound. The predicted error cannot distinguish between the two different boundary conditions. For the conducted tests we expect the exact error to be small under displacement control since we

are imposing the positions exactly for both cases. In fact if ν was kept constant and only young's modulus was changed the exact error would be zero. This is clearly not the case under traction control.
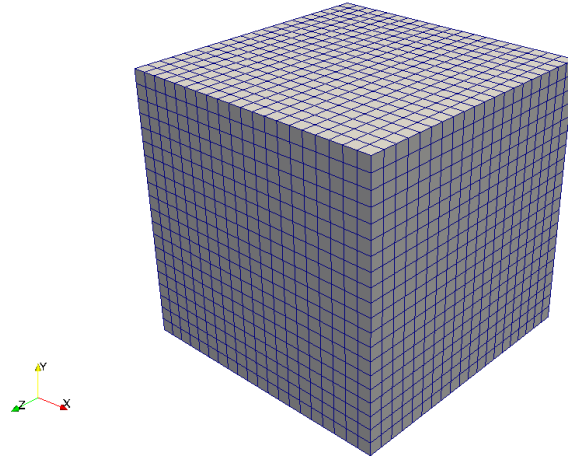
Figure 6.3: Mesh of cube used in the simulations
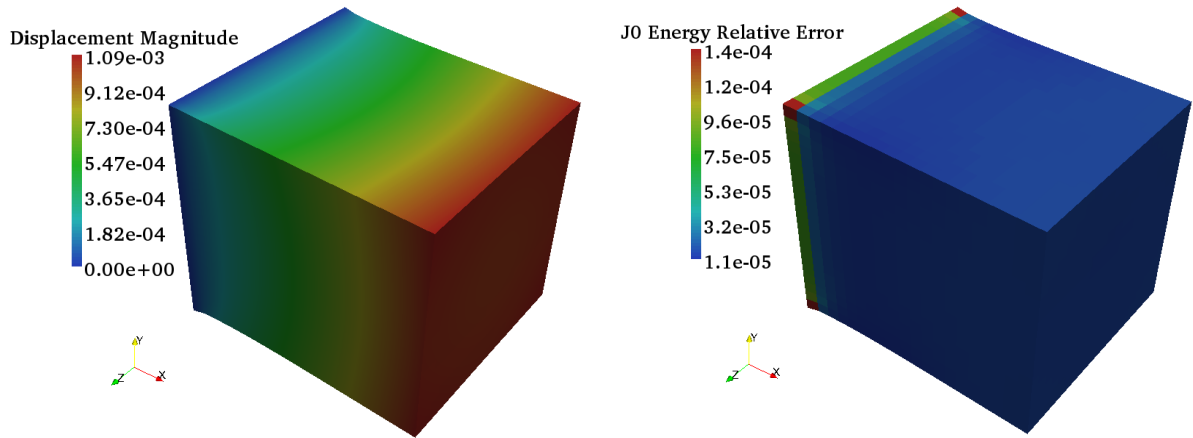
Figure 6.4: Deformed shape on the left showing the displacement contour and relative error plots $\frac{\zeta_K}{||\mathbf{u}^*||_{E(\Omega)}}$ on the right

6.3.2 Hetrogenous-Homogenous Comparisons

In these examples we consider the case of a fibrous material with a known microstructure. Using some specific homogenized properties we conduct numerical experi-
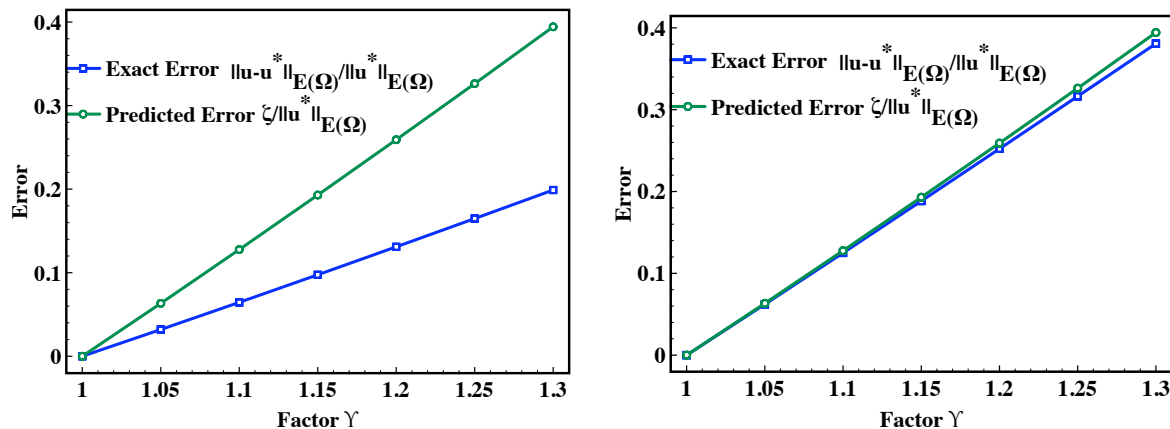
Figure 6.5: Plot of error for displacement control on the left and for traction control on the right. We note how for the traction control the predicated global error ζ is a very strict bound, on the other hand for displacement the predicated global error ζ is a true upper bound.

ments comparing the exact error to the predicted error. For simplicity the microstructure has fictitious dimensions, with a fiber radius of $0.2m$ in a square matrix material of dimension $1m$. The fiber volume fraction was assumed to be $\nu_f = 0.5$ which resulted in 4 fibers in the domain. The material properties of the heterogenous solid are summarized in Table. 6.1.

Table 6.1: Heterogeneous Material Properties

Material	E(GPa)	ν
Carbon	260	0.3
Epoxy	5	0.3

Three cases of homogenized material properties are used for comparison to understand the effect of the homogenized material property on the accuracy of the error indicator ζ. The first two cases are the Reuss-Voigt bounds as lower and upper estimates of the heterogeneous material properties. The third we use some experimental material properties for carbon-epoxy composite. These material properties are summarized in Table. 6.2. Note, that for the geometry considered the homgenized properties are not representative since the utilized microstructure does not satisfy the appropriate size conditions. Nevertheless, these will serve the purpose of understanding the error bounds behavior. The results for both the

traction and displacement control boundary conditions are summarized in Table. 6.3-6.4. Note, the boundary conditions in each case were the same as those used in the isotropic-isotropic comparison case. Figure. 6.6 shows the deformation under traction control and the relative predicted error $\frac{\zeta_K}{||\mathbf{u}^*||_{E(\Omega)}}$ element wise, where K is the element number.

Table 6.2: Homogenized Material Properties

Material	E_{11}	E_{22}	ν_{12}	ν_{23}	G_{12}
Reuss Bound	9.83	9.83	0.3	0.3	3.77
Voigt Bound	132.5	132.5	0.3	0.3	50.96
Experimental	140	10	0.3	0.3	7

We notice that the accuracy of the error indicator ζ depends on the homogenized material properties used. This can be particularly seen for the traction controlled case where when we assumed the Reuss bound the error indicator ζ was very close to the exact error on the other hand the Voigt bound and the experimental properties result in a less accurate error prediction. When compared to the displacement controlled tests we notice again that the exact errors are smaller than the ones resulting from traction control conditions, this is again because the displacements on the boundaries are the same for both solutions. This results in a loss of accuracy for the error predicator ζ under displacement control.

Table 6.3: Error for traction control

Material	$\dfrac{||\mathbf{u}^h - \mathbf{u}^{*,h}||_{E(\Omega)}}{||\mathbf{u}^{*,h}||_{E(\Omega)}}$	$\dfrac{\zeta}{||\mathbf{u}^{*,h}||_{E(\Omega)}}$
Reuss Bound	0.9319	0.9666
Voigt Bound	1.1181	3.5535
Experimental	1.1755	3.6654

Table 6.4: Error for displacement control

Material	$\dfrac{\|\mathbf{u}^h - \mathbf{u}^{*,h}\|_{E(\Omega)}}{\|\mathbf{u}^{*,h}\|_{E(\Omega)}}$	$\dfrac{\zeta}{\|\mathbf{u}^{*,h}\|_{E(\Omega)}}$
Reuss Bound	0.1055	0.9666
Voigt Bound	0.0888	3.5463
Experimental	0.1507	3.6350
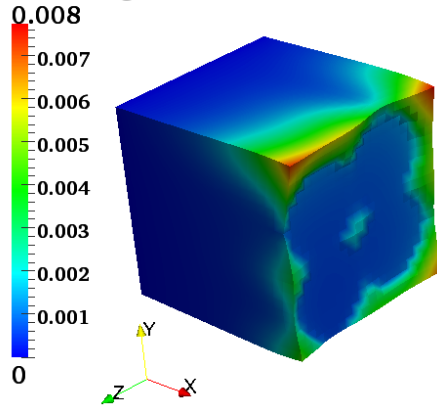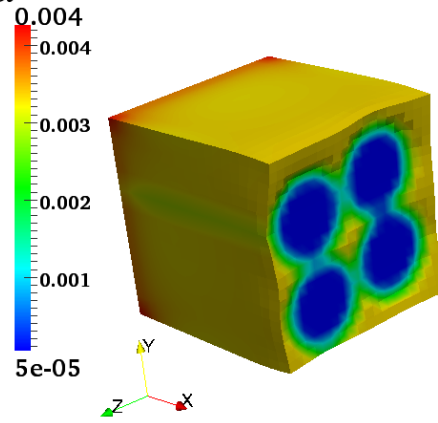
Figure 6.6: Deformed shape on the left showing the displacement contour and the relative error $\frac{\zeta_K}{\|\mathbf{u}^*\|_{E(\Omega)}}$ plot on the right for a sample with four fibers and volume fraction $\nu_f = 0.5$

Chapter 7

Multiscale Subdomain Construction

In this section we will break the entire domain into subdomains and utilize the exact error bound of Eqn. 7.0.7 to choose which subdomains to solve at the microscale. To start lets consider Figure. 7.1. The figure is a schematic of a heterogeneous solid that is partitioned into predefined non-overlapping subdomains $\Theta_k, k = 1, 2, ..., N$. It is clear that the union of the subdomains results in the global domain. We therefore, have

$$\bigcup_{k=l}^{N} \Theta_k = \Omega, \quad \Theta_k \cap \Theta_l = 0, k \neq l \tag{7.0.1}$$
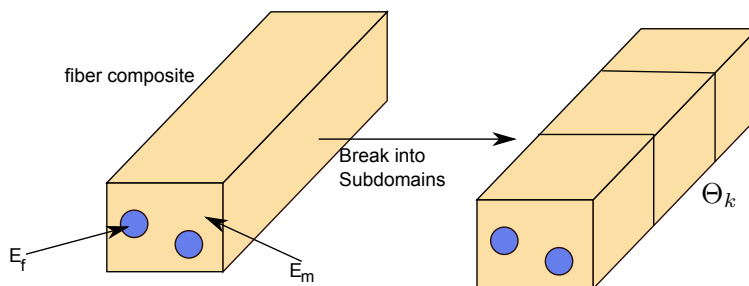
Figure 7.1: Schematic of a heterogeneous body shown being deconstructed into subdomains Θ_k, as shown on the on the right side.

As usual each subdomain has a boundary $\partial\Theta_k$ where traction and displacement boundary conditions are applied. We can now construct the local subdomain problem defined as

$$\text{Find } \tilde{\mathbf{u}} \in H^1(\Theta_k), \tilde{\mathbf{u}}|_{\partial\Theta_{k,\mathbf{u}}} = \mathbf{d}, \text{where } \forall \mathbf{v} \in H^1(\Omega) \tag{7.0.2}$$

$$\mathcal{B}(\tilde{\mathbf{u}}_k, \mathbf{v}) = \mathcal{F}(\mathbf{v}_k) \tag{7.0.3}$$

where k refers to the subdomain number and we have

$$\mathcal{B}(\tilde{\mathbf{u}}_k, \mathbf{v}) = \int_{\Theta_k} \nabla\mathbf{v}_k : \mathbb{C}\nabla\tilde{\mathbf{u}}_k d\Theta_k \tag{7.0.4}$$

and

$$\mathcal{F}(\mathbf{v}_k) = \int_{\partial\Theta_{k,\mathbf{t}}} \mathbf{t} \cdot \mathbf{v}_k d\Gamma_k + \int_{\Theta_k} \mathbf{f} \cdot \mathbf{v}_k d\Theta_k \tag{7.0.5}$$

We can now specify under what boundary conditions these local problems are solved. Specifically, for the displacement boundary conditions we impose $\tilde{\mathbf{u}}|_{\partial\Theta_{k,\mathbf{u}}} = \mathbf{u}^*|_{\partial\Theta_{k,\mathbf{u}}}$. If the global problem has traction boundary conditions specified then these are applied to subdomains whose boundary intersects with the global domain. With the local solution at hand we can now simply replace $\mathbf{u}_k^*$ with the values from $\tilde{\mathbf{u}}_k$, thus updating the homogenous solution with results from the local boundary value problem. Therefore, the global solution becomes

$$\tilde{\mathbf{u}}^* = \mathbf{u}^* + \sum_{k=1}^{N} \mathcal{E}_k(\tilde{\mathbf{u}}_k - \mathbf{u}_k^*) \tag{7.0.6}$$

where is $\mathcal{E}_k$ is an operator that takes the values in the space Θ_k and puts them into the space defined by Ω. The local subdomain error indicator is assumed to be

$$\zeta_k = ||\mathcal{J}_0\nabla\mathbf{u}_k^*||_{E(\Theta_k)} \tag{7.0.7}$$

where the global error bound $\zeta = \sqrt{\sum_{k=1}^{N} \zeta_k^2}$. We note that ζ_k is not an upper bound on the error in the subdomain.

7.1 Connecting Scales with Different Mesh Sizes

When solving the homogeneous problem it is clear that in many cases a fine mesh is not required for convergence. More specifically, the convergence does not depend on the microstructure. Therefore, in circumstances when the mesh size of the global homogenous problem is too coarse relative to the microstructure we must be able to remesh the local heterogeneous subdomains and connect the two scales together. Figure. 7.2 illustrates the scenario. Where, given a subdomain(Θ_k) and noting that the blue coarse mesh is for the homogeneous global problem and the finer red mesh is for the local scale that includes the microstructure.
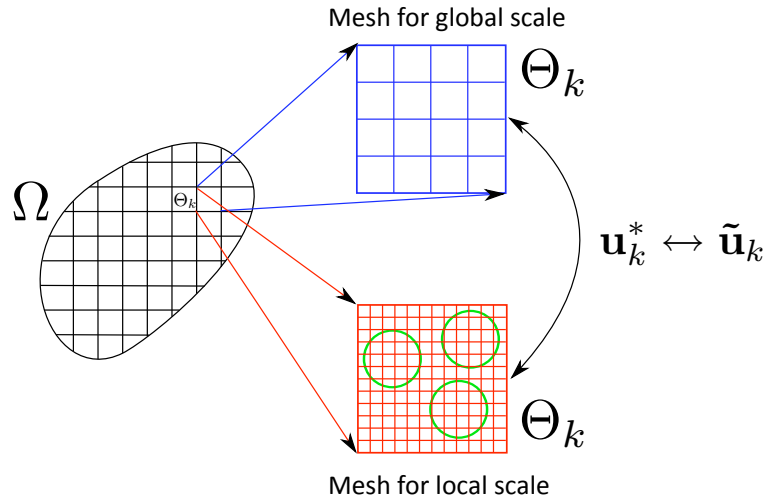
Figure 7.2: This figure shows how the two scales are related. The domain Ω in the center left is shown broken up into subdomains Θ_k. The mesh size for the homogenized body at the scale of the subdomain is show in the upper right part. On the other hand the mesh at the subdomain scale with microstructure included is shown in the bottom right part. These two meshes are related to each other.

The solution from the homogenous problem is projected onto the local problem as described in the previous section. However, since the mesh's do not match we must be able to interpolate displacement solution($\mathbf{u}_k^*$) to any specified position $\mathbf{x}$ in the subdomain.

Therefore, given a nodal position($\tilde{\mathbf{x}}$) in the local scale mesh we mush be able to identify in what element in the global scale mesh it lies and what corresponding master element coordinate($\boldsymbol{\zeta}$) value it posses. This can be achieved by finding the inverse mapping relationship. For the three-dimensional case an analytic solution is not possible, we therefore must solve the system of nonlinear equations defining the isoparametric mapping. The reader is referred to Knupp. [42], V. Murti etc . [43] and K.M.Yuan etc. [44] for an over view of various methods. These papers provide algorithms that optimize the identification of the inverse map and therefore, reduce the search time needed to find the inverse coordinates. In this work we do not try to optimize the searching process and instead use a simple algorithm. Specifically, we have the form

$$x_i = N(\boldsymbol{\zeta})_I X_{iI} \tag{7.1.1}$$

where N_I are the master element shape function which depend on $\boldsymbol{\zeta}$ and X_{iI} are the element coordinates of the global mesh. We use the Newton-Raphson method to solve this nonlinear system of equations for $\boldsymbol{\zeta}$. The algorithm is described in Algorithm. 1

Algorithm 1 Algorithm for inverse mapping

Given $\mathbf{x}_m$ find $\boldsymbol{\zeta}_m$
Set Tolerance for convergence
Guess $\boldsymbol{\zeta} = \mathbf{0}$
for k = 1,Number of Elements **do**
    Set element Coordinates X_{iI}
    while Error $\geq$ Tolerance **do**
      1. $x_i^n = N(\boldsymbol{\zeta}^n)_I X_{iI}$
      2. $\boldsymbol{\zeta}^{n+1} = \boldsymbol{\zeta}^n + (\mathbf{x}_m) - \mathbf{x}(\boldsymbol{\zeta}^n)) \left(\frac{d\mathbf{x}}{d\boldsymbol{\zeta}}\right)^{-1}_{\boldsymbol{\zeta}^n}$
      3. Check error $||\mathbf{x}_m - \mathbf{x}^{n+1}||_2$
    end while
    SET $\boldsymbol{\zeta}_m = \boldsymbol{\zeta}^{n+1}$
    if $\boldsymbol{\zeta}_m$ is in between ± 1 **then**
      Exit Loop over elements
    end if
end for

Given the master element coordinates $\boldsymbol{\zeta}$, we can now use them in the shape functions to interpolate the homogenized displacement solution $\mathbf{u}^*$ to nodal values $\tilde{\mathbf{u}}$ on the

local mesh with microstructure. This is a basic algorithm that works well, but can be very slow if local scale mesh is very fine. With this algorithm we can now connect the mesh scales together and solve problems with small microstructure. Examples will be shown in the coming sections.

7.2 Overview of Numerical Analysis

Before proceeding with the numerical analysis, the material properties used and the various numerical setups are overviewed. We start by introducing the notion of a material mismatch ratio $\kappa = \frac{E_{fiber}}{E_{matrix}}$, while Poisson's ratio ν is the same for both materials. The base material is the matrix material and we consider an epoxy with $E_{matrix} = 5GPa$. For all the ensuing analysis the mismatch ratios used are $\kappa = [5, 10, 52]$, where for $\kappa = 52$ we have carbon-fiber material properties. Clearly these are the material properties for the micro-constituents and accordingly we need to compute homogenized material properties based on procedures described in Chapters. 4-5 to solve large scale structural problems. These basic results are summarized in Section. 7.2.1. The next part of this section will explain the different numerical experiments that will be conducted and why we are interested in their analysis.

7.2.1 Extracting Homogenized Properties

The summary of the homogenization results are described in this section. The size of the RVE plots for the case of $\kappa = 52$ are show in Figure. 7.3. The moduli can then be processed by finding the compliance matrix as the inverse of the elasticity matrix. We will consider the RVE with 64 fibers to get the converged properties. The elasticity and compliance matrices are given in Eqn. 7.2.1-7.2.2. The results for the three different mismatch ratios are summarized in Table. 7.1 in the form of elastic constants. These properties will be used for the numerical simulations to obtain the homogenized response.
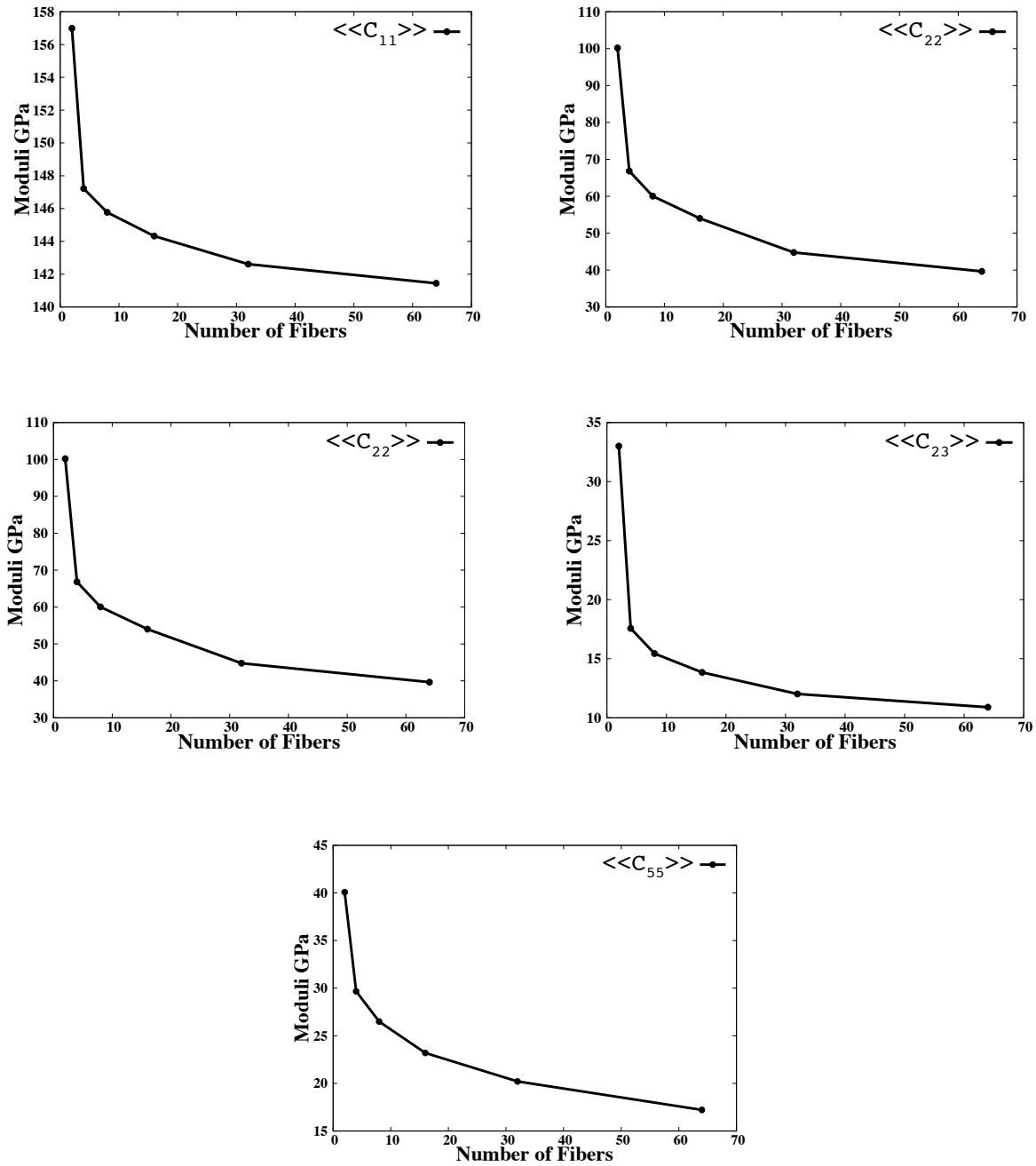
Figure 7.3: Effect of RVE size on properties for $\nu_f = 0.5$ and $\kappa = 52$. The plots show the convergence of the five independent material properties change as a function of the RVE size. This gives us the material properties for a give set of matrix/fiber material properties.

$$
\langle\langle \mathbb{C} \rangle\rangle = \underbrace{\begin{bmatrix}
141.4451 & 15.1631 & 14.6420 & 0 & 0 & 0 \\
15.1632 & 39.6500 & 10.8936 & 0 & 0 & 0 \\
14.6420 & 10.8936 & 39.6500 & 0 & 0 & 0 \\
0 & 0 & 0 & 14.3782 & 0 & 0 \\
0 & 0 & 0 & 0 & 17.2170 & 0 \\
0 & 0 & 0 & 0 & 0 & 17.2170
\end{bmatrix}}_{\text{Elasticity Matrix}}
\tag{7.2.1}
$$

$$
\langle\langle \mathbb{S} \rangle\rangle = \underbrace{\begin{bmatrix}
0.0075 & -0.0023 & -0.0022 & 0 & 0 & 0 \\
-0.0023 & 0.0280 & -0.0068 & 0 & 0 & 0 \\
-0.0022 & -0.0068 & 0.0279 & 0 & 0 & 0 \\
0 & 0 & 0 & 0.0695 & 0 & 0 \\
0 & 0 & 0 & 0 & 0.05810 & \\
0 & 0 & 0 & 0 & 0 & 0.0581
\end{bmatrix}}_{\text{Compliance Matrix}}
\tag{7.2.2}
$$

Table 7.1: Homogenized Material Properties for different mismatch ratios

Mismatch κ	5	10	52
E_{11} GPa	14.9	27.48	132.6
E_{22} GPa	11.2	15.63	35.74
ν_{12}	0.300	0.299	0.304
ν_{23}	0.2981	0.291	0.245
G_{12} GPa	4.47	6.53	17.2 GPa

7.2.2   Numerical Experiments

All the numerical experiments in this section are conducted on a thin plate. Specifically, our interest lies in assessing the following issues

1. Analysis of subdomain error indicators under different boundary conditions

(a) Where do the largest errors occur?

2. Analysis of the multiscale process and assessing

    (a) How much can we improve our solution?

    (b) How many subdomains do we need to get good improvement in solution space?

To conduct these tests, we consider a fiber microstructure that can easily be resolved through the Finite Element Method. Subsequently a more realistic fiber dimension is used to conduct the multiscale analysis, where our main interest would be to show how the procedure works for more realistic micro-structures.

7.3 Analysis of Subdomain Errors

As previously mentioned we will consider a thin plate in bending as an example to explore both the global error and the local error indicators in the subdomains. These errors indicators ζ, ζ_k will then be compared to the exact errors by solving the problem with the exact microstructure. The overall scheme will be to prescribe the micro-structural material properties, obtain the homogenized properties and then conduct the large scale simulations and predict the error. The domain is broken up into subdomains as previously described.

The plate has dimensions of $1m \times 1m \times 0.1m$ as shown in Figure. 7.4. We will consider multiple boundary conditions including, fixed along both x and y planes, fixed along x planes only and fixed along y planes only. For this analysis traction boundary conditions are applied on the surface ($z = 0.1m$). The traction is over a circular region of the plate. The region has a radius of $0.2m$ and is centered in the middle of the plate. The fibers are assumed to have a radius of $0.04m$. This will allow us to solve the complete heterogeneous problem in a time efficient manner.

7.3.1 Various Boundary Conditions on X and Y Surfaces

Since the radius of the fibers are large we can solve the hetrogenous problem to obtain the exact error and compare it to the predicted error ζ. Therefore, the solutions to both the hetrogeneous and homogeneous problems are obtained using the Finite Element Method, with solutions $\mathbf{u}^h$ and $\mathbf{u}^{*,h}$ respectivelly. For both these cases the same mesh is used. We enforce that there are at least eight elements through each fiber. For the current
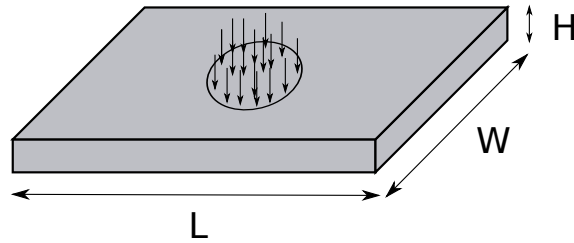
Figure 7.4: Schematic of the plate showing the circular center punch traction/displacement used for the ensuing simulations.

setup we break up the plate into $10 \times 10 \times 1$ subdomains, 10 domains in x, 10 in y and 1 in z. Given the fiber radius, our mesh over each subdomain is $9 \times 9 \times 9$ elements. We can then calculate the mesh size over the entire region from the prescribed subdomain mesh. Since this is a static problem we apply a pseudo time scheme in which the applied traction evolves such that $\mathbf{t} = -0.1 \times time - 0.1$. Also, at each time step both the exact error and the local error indicators are calculated in each subdomain.

Solving the boundary value problem for the three different boundary conditions gives us the displacement field which is shown in Figures. 7.5-7.7. The effect of the fibers can be seen from the figures on the right. When fibers are included the displacements are no longer symmetric. The error indicator ζ_k in the subdomains for the different boundary conditions are shown at each time step in Figure. 7.8-7.10. We note that the error distribution for the x-y fixed and x fixed boundary conditions are very similar, the largest errors occur on the edges defined by $x = [\pm 1, 0, 0]$. Hence, the most significant errors are along the fiber direction. This can be attributed to the high stiffness of the fibers. On the other hand when observing the results from the y-fixed boundary conditions we notice the largest errors occur in the center of the plate. The plate is allowed to move in the fiber direction.

When conducting these numerical tests and looking at the error in each subdomain it's important to understand that there is no guarantee that the predicted error is in fact an upper bound in the given domain. For this reason we plot the local error indicator ζ_k in each subdomain vs the exact error in each subdomain, with Figure. 7.11 illustrating the results. These plots are for the three different boundary conditions at time step $time = 0$. The red line indicates the exact error line. It is observed that for these examples all the subdomain errors are above the line. Hence, they are upper bounds. Note, this is not
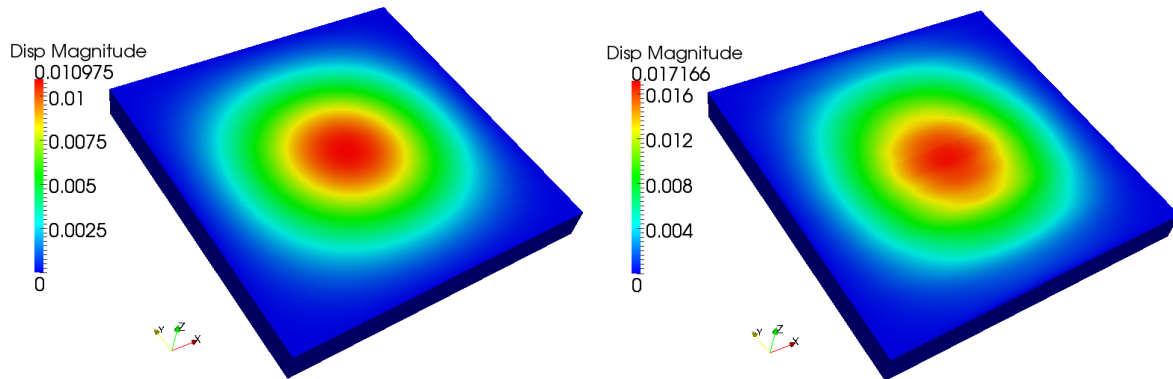
Figure 7.5: Displacement of 1) Homogeneous body on the left, 2) Hetrogeneous body on the right with x-y fixed boundary conditions
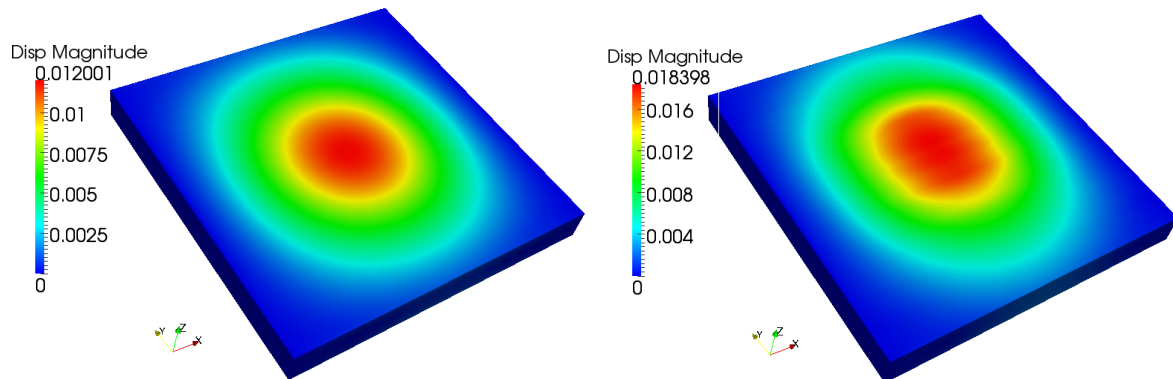
Figure 7.6: Displacement of 1) Homogeneous body on the left, 2) Hetrogeneous body on the right with x fixed boundary conditions
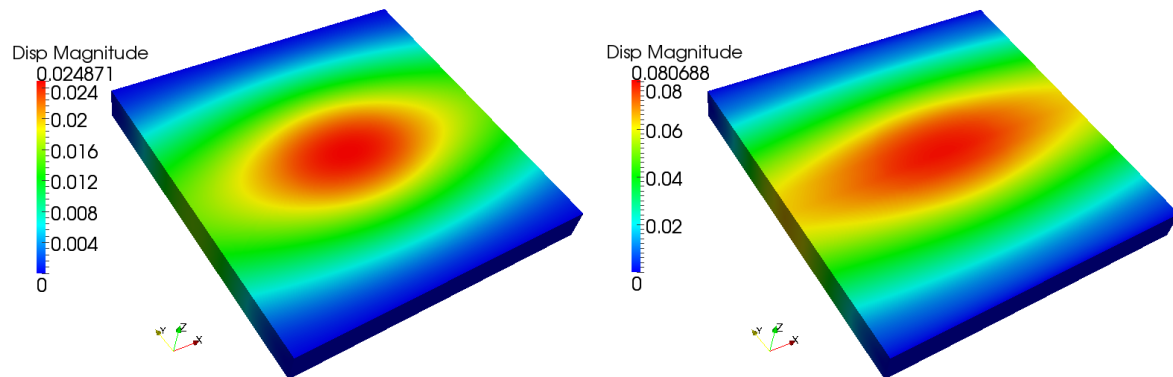
Figure 7.7: Displacement of 1) Homogeneous body on the left, 2) Hetrogeneous body on the right with y fixed boundary conditions
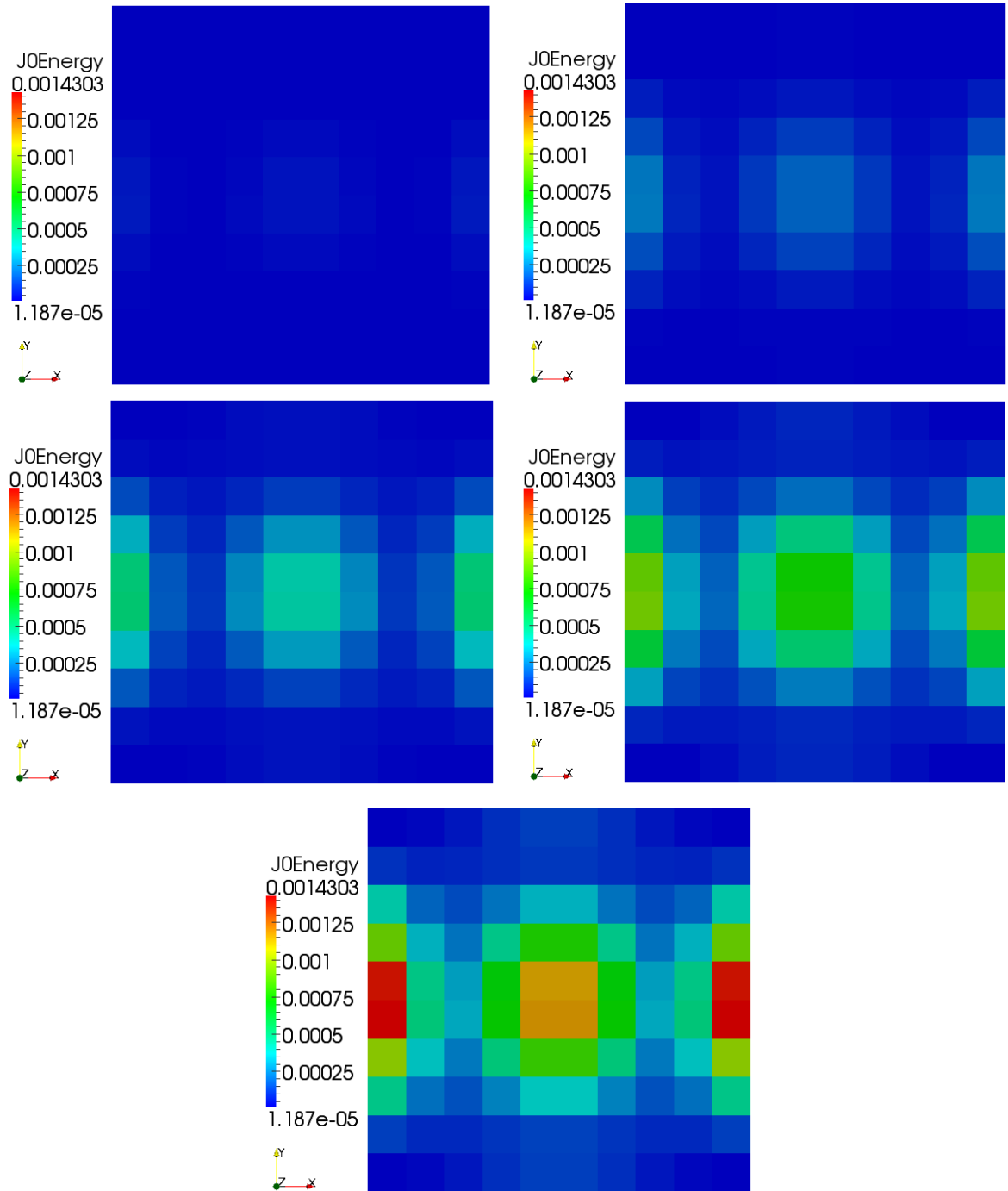
Figure 7.8: Plots showing ζ_k error indicator at each loading time for fixed x and y surfaces as a function of the loading. The loading increasing going from left to right
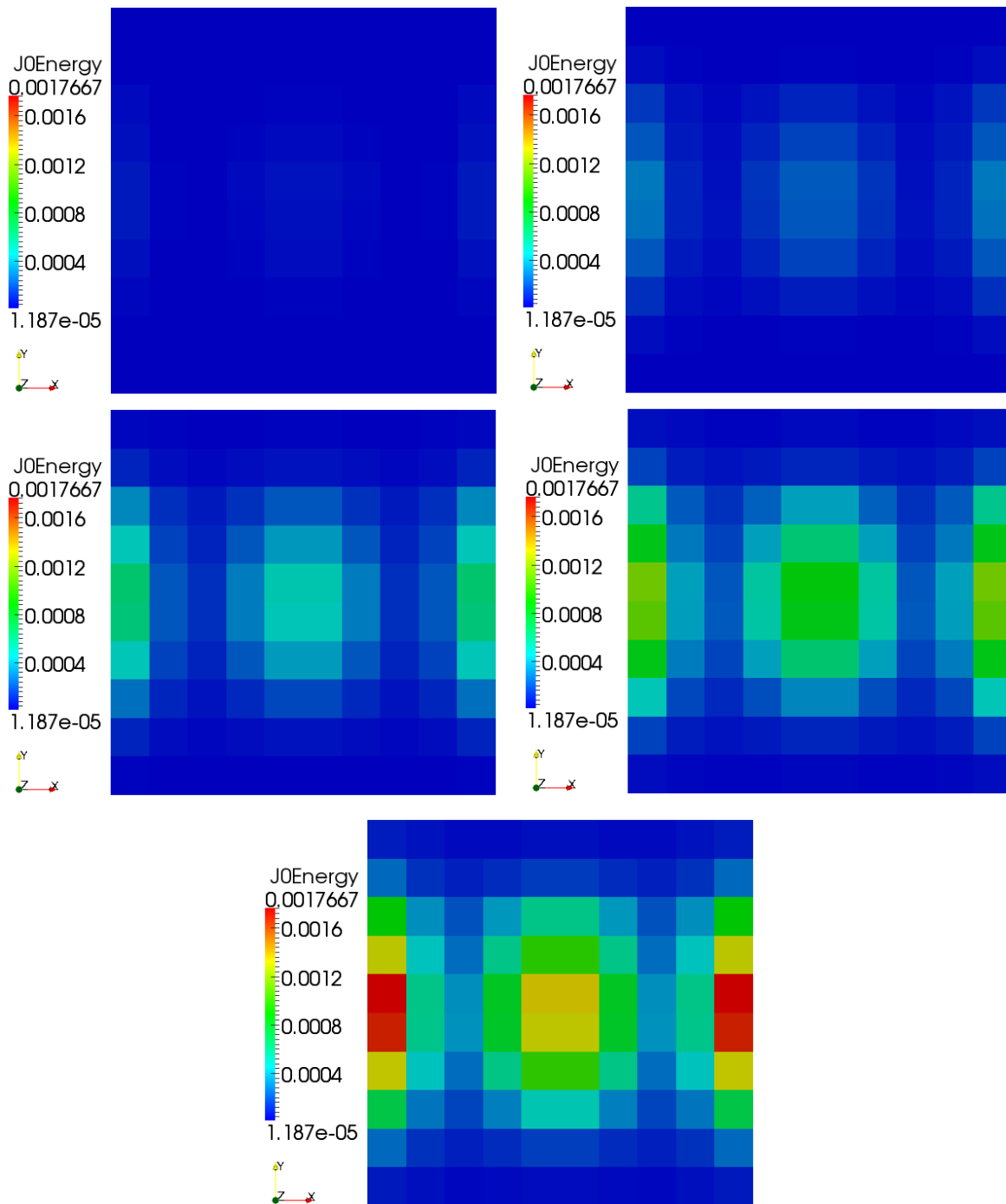
Figure 7.9: Plots showing ζ_k error indicatorat each loading time for fixed x surfaces as a function of the loading. The loading increasing going from left to right
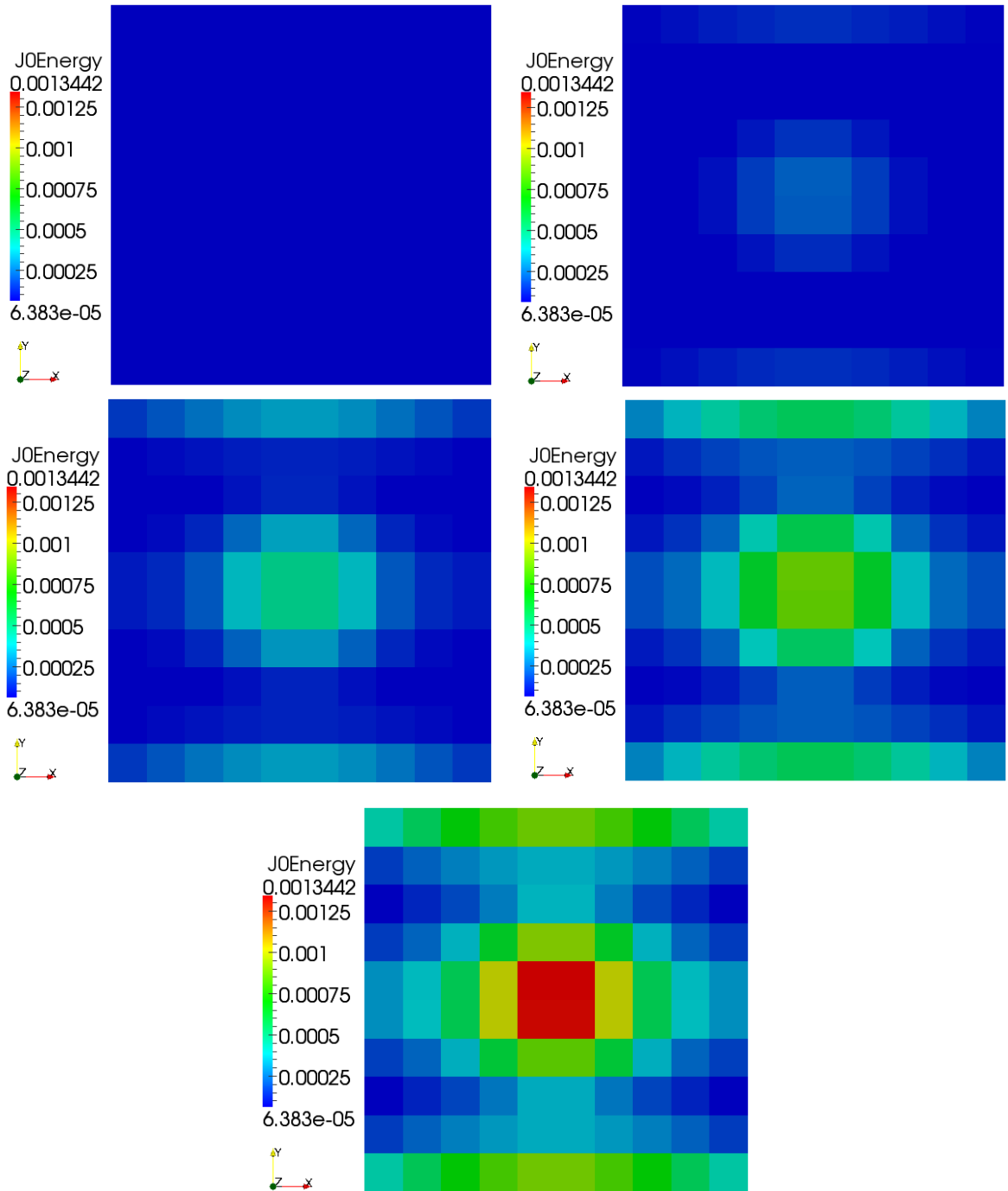
Figure 7.10: Plots showing ζ_k error indicator at each loading time for fixed y surface as a function of the loading. The loading increasing going from left to right

guaranteed in other situations. We also notice that if we compare two subdomains such that subdomain1 has a larger exact error than subdomain2, it is possible that the predicted error in subdomain2 is larger than the predicted error in subdomain1. This emphasis the fact the error predictions in the subdomains must be treated with caution and can only be used as a guide.
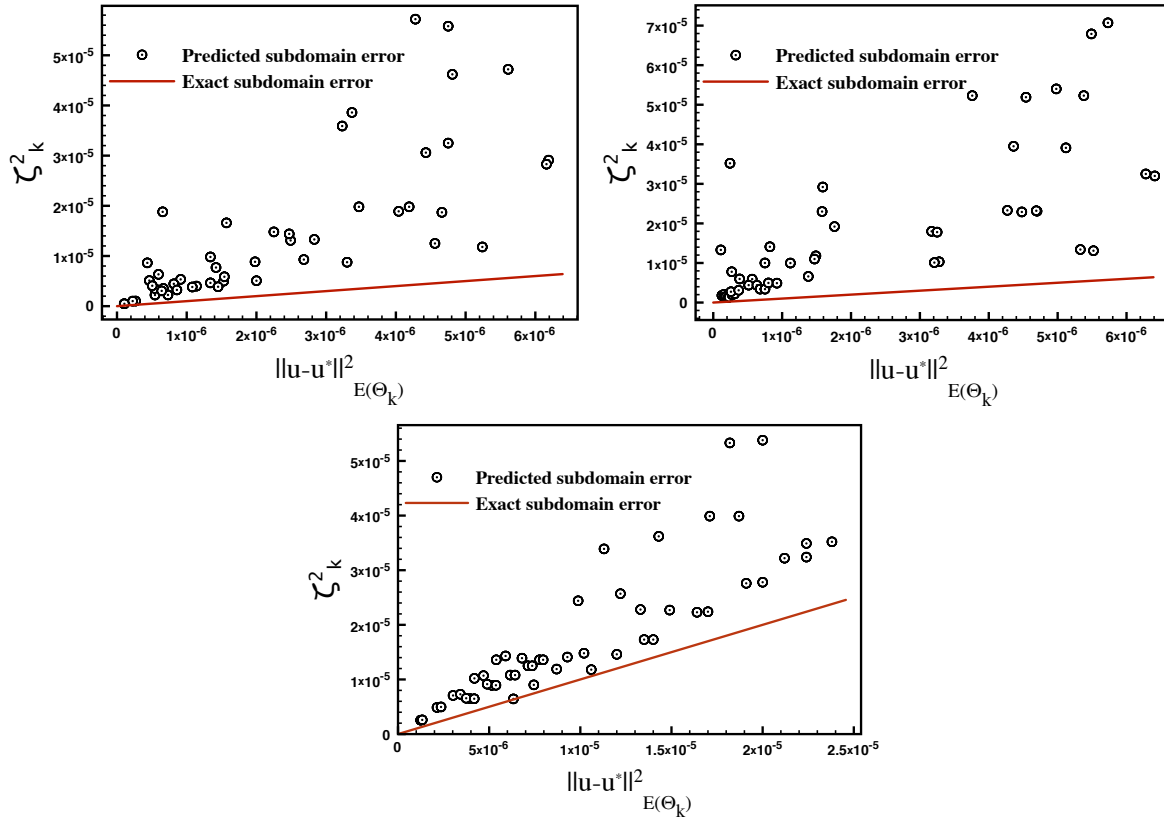
Figure 7.11: These figures show ζ_k error indicator at each subdomain for the following boundary conditions 1)x -y fixed which is shown in the upper left, 2) x fixed which is shown in the upper right and 3) y fixed which is shown in the bottom center.

It is interesting to note that the relative error $\zeta/||\mathbf{u}^{*,h}||_{E(\Omega)}$ remains constant as the traction load is increased, this is clearly due to the linearity of the system. Table. 7.2 shows the global error for the different applied boundary conditions. We notice how the overall performance of the error indicator clearly depends on the boundary conditions, where for y place fixed case we have the best approximation to the exact error.

Table 7.2: Global Errors

Boundary condition	$\dfrac{\zeta}{\lVert \mathbf{u}^h - \mathbf{u}^{*,h} \rVert_{E(\Omega)}}$	$\dfrac{\zeta}{\lVert \mathbf{u}^{*,h} \rVert_{E(\Omega)}}$
X-Y Fixed	2.384	2.652
X Fixed	2.831	2.987
Y Fixed	1.335	1.869

7.4 Multiscale Analysis of Plate with Fiber Radius of 0.04m

In this section we will solve the local subdomain boundary value problem defined in Eqn. 7.0.3 and update the global solution using Eqn. 7.0.6. We will analyze both the effect the subdomain size has on enhancing the global solution and the effect of choosing only some subdomains that are above a certain error tolerance. The analysis is conducted on a plate in bending with similar boundary conditions used in the plate bending example to analyze the subdomain errors. Specifically, the plate is clamped on all edges and we employ both displacement and traction control boundary conditions on the surface ($z = 0.1m$). The applied displacement is $\mathbf{u} = [0, 0, -0.01]$ and the traction is $\mathbf{t} = [0, 0, -0.1]$. The loads are imposed on a circular region with radius 0.15m and centered in the middle of the plate. The fiber radius is $r = 0.04$m which is the same as before. Additionally, the fiber positions are kept constant with the orientations summarized in Table. 7.3 and Figure. 7.12 showing the fibers in a matrix. We will also explore the effect the material mismatch ratios $\kappa = [5, 10, 52]$ have on the solution updates. Keep in mind that the homogenized material properties are summarized in Table. 7.1 and will be used to solve the homogeneous problem.

The mesh size to solve both the homogeneous and heterogenous boundary value problem was $81 \times 81 \times 9$ elements. This guaranteed about 8 elements across each fiber. Figure. 7.13 shows the displacement contours for both the homogeneous and heterogeneous solutions under a displacement control punch for $\kappa = 52$.

7.4.1 Effect of Number of Subdomain on Enhancing Homogeneous Solutions

For this analysis the sub-structuring of the global domain is changed to understand it's effect on the updated solution $\tilde{\mathbf{u}}^*$. We will consider three mismatch ratios of $\kappa = 5, 10, 52$

Table 7.3: Fiber positions for nine fibers

Y position	Z position	Radius
0.7358	0.0538	0.04
0.8534	0.0598	0.04
0.3145	0.0428	0.04
0.1587	0.0442	0.04
0.6302	0.0503	0.04
0.4503	0.0464	0.04
0.9563	0.0449	0.04
0.0622	0.0421	0.04
0.5319	0.0499	0.04
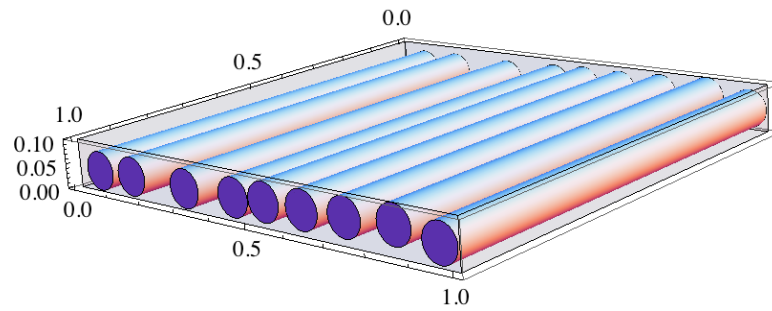
Figure 7.12: Plot showing the fibers with radius 0.04m inside the plate
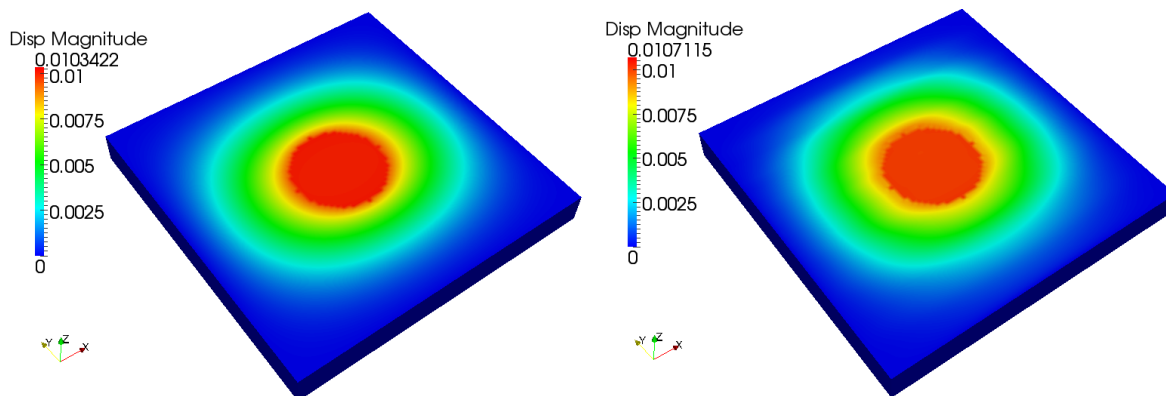
Figure 7.13: Displacement of 1) Homogeneous body on the left, 2) Hetrogeneous body on the right with x-y fixed boundary conditions and $\kappa = 52$

and 7 cases for sub-structuring the domain. The results for both traction and displacement boundary conditions are summaried in in Table. 7.4-7.5. The first substructuring case is by considering 1X1X1 subdomains, in other words we are solving the complete heterogeneous problem. As expected this drives the error down to zero. In the next cases the domain is halved along x and y. Figures. 7.14-7.15 shows the percent change in solution error defined as

$$\%\Delta e = 100 \times \frac{||\mathbf{u}^h - \mathbf{u}^{*,h}||_{E(\Omega)} - ||\mathbf{u}^h - \tilde{\mathbf{u}}^{*,h}||_{E(\Omega)}}{||\mathbf{u}^h - \mathbf{u}^{*,h}||_{E(\Omega)}} \tag{7.4.1}$$

for both the displacement controlled and traction controlled punch, respectively. The percent change between the exact error in column 5 and enhanced error column 6 of Tables. 7.4-7.5 drops rapidly once we partition the global domain. This is ofcourse expected since we are solving a local boundary value problem with incorrect internal boundary conditions. Nonetheless, there is clearly a significant improvement in the homogeneous solution when sub-subtructuring the global domain. Clearly, the larger the size of the subdomain the better, this size will be limited by memory considerations in real domains with fine micro-structural attributes.

Figure 7.14: Percent change in solution error $\%\Delta e$ by solving the smaller subdomain boundary value problem under a displacement controlled punch.

One thing to note is that we are able to get better solution improvements when

Table 7.4: Subdomain size effect on solution improvement for displacement control

Subdomain size	κ	Number Subdomain	$\frac{\zeta}{||\mathbf{u}^{*,h}||_{E(\Omega)}}$	$\frac{||\mathbf{u}^h - \mathbf{u}^{*,h}||_{E(\Omega)}}{||\mathbf{u}^{*,h}||_{E(\Omega)}}$	$\frac{||\mathbf{u}^h - \tilde{\mathbf{u}}^{*,h}||_{E(\Omega)}}{||\mathbf{u}^{*,h}||_{E(\Omega)}}$	$\%\Delta e$
$1 \times 1 \times 1$	5	1	1.0055	0.435	0.0	100.0
$2 \times 2 \times 1$	5	4	1.0055	0.435	0.137	68.5
$4 \times 4 \times 1$	5	16	1.0055	0.435	0.191	56.1
$6 \times 6 \times 1$	5	36	1.0055	0.435	0.238	45.2
$8 \times 8 \times 1$	5	64	1.0055	0.435	0.270	37.8
$12 \times 12 \times 1$	5	144	1.0055	0.435	0.318	26.8
$16 \times 16 \times 1$	5	256	1.0055	0.435	0.346	20.4
$1 \times 1 \times 1$	10	1	1.554	0.621	0.0	100
$2 \times 2 \times 1$	10	4	1.554	0.621	0.194	68.7
$4 \times 4 \times 1$	10	16	1.554	0.621	0.272	56.2
$6 \times 6 \times 1$	10	36	1.554	0.621	0.339	45.3
$8 \times 8 \times 1$	10	64	1.554	0.621	0.388	37.6
$12 \times 12 \times 1$	10	144	1.554	0.621	0.456	26.5
$16 \times 16 \times 1$	10	256	1.554	0.621	0.497	19.9
$1 \times 1 \times 1$	52	1	4.068	2.754	0.0	100.0
$2 \times 2 \times 1$	52	4	4.068	2.754	0.950	65.5
$4 \times 4 \times 1$	52	16	4.068	2.754	1.299	52.8
$4 \times 4 \times 1$	52	36	4.068	2.754	1.653	39.9
$8 \times 8 \times 1$	52	64	4.068	2.754	1.889	31.4
$12 \times 12 \times 1$	52	144	4.068	2.754	2.189	20.5
$16 \times 16 \times 1$	52	256	4.068	2.754	2.396	13.0

Table 7.5: Subdomain size effect on solution improvement for traction control

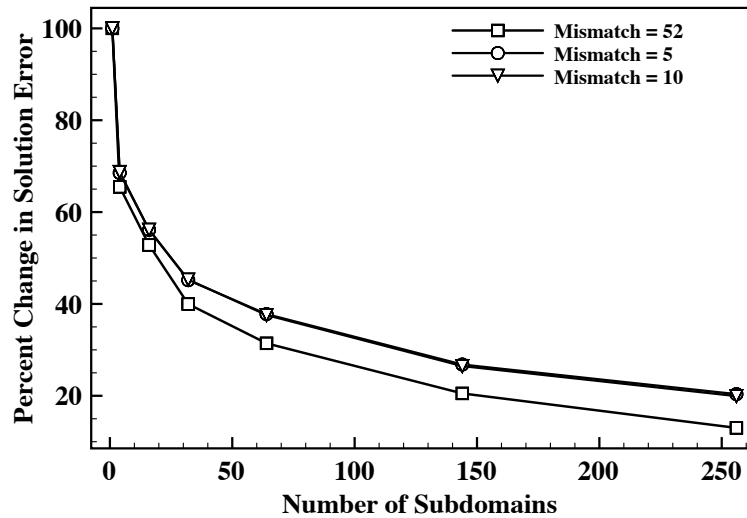| Subdomain size	κ	Number Subdomain	$\frac{\zeta}{\|\mathbf{u}^{*,h}\|_{E(\Omega)}}$	$\frac{\|\mathbf{u}^h-\mathbf{u}^{*,h}\|_{E(\Omega)}}{\|\mathbf{u}^{*,h}\|_{E(\Omega)}}$	$\frac{\|\mathbf{u}^h-\tilde{\mathbf{u}}^{*,h}\|_{E(\Omega)}}{\|\mathbf{u}^{*,h}\|_{E(\Omega)}}$	$\%\Delta e$
$1 \times 1 \times 1$	5	1	1.005	0.435	0.0	100.0
$2 \times 2 \times 1$	5	4	1.005	0.435	0.137	68.5
$4 \times 4 \times 1$	5	16	1.005	0.435	0.191	56.1
$6 \times 6 \times 1$	5	36	1.005	0.435	0.238	45.2
$8 \times 8 \times 1$	5	64	1.005	0.435	0.270	37.8
$12 \times 12 \times 1$	5	144	1.005	0.435	0.318	26.8
$16 \times 16 \times 1$	5	256	1.005	0.435	0.346	20.3
$1 \times 1 \times 1$	10	1	1.536	0.723	0.0	100.0
$2 \times 2 \times 1$	10	4	1.536	0.723	0.453	37.4
$4 \times 4 \times 1$	10	16	1.536	0.723	0.491	32.1
$6 \times 6 \times 1$	10	36	1.536	0.723	0.533	26.3
$8 \times 8 \times 1$	10	64	1.536	0.723	0.558	22.9
$12 \times 12 \times 1$	10	144	1.536	0.723	0.609	15.8
$16 \times 16 \times 1$	10	256	1.536	0.723	0.634	12.4
$1 \times 1 \times 1$	52	1	2.698	0.905	0.0	100.0
$2 \times 2 \times 1$	52	4	2.698	0.905	0.473	47.7
$4 \times 4 \times 1$	52	16	2.698	0.905	0.542	40.1
$6 \times 6 \times 1$	52	36	2.698	0.905	0.614	32.1
$8 \times 8 \times 1$	52	64	2.698	0.905	0.658	27.2
$12 \times 12 \times 1$	52	144	2.698	0.905	0.740	18.2
$16 \times 16 \times 1$	52	256	2.698	0.905	0.783	13.4
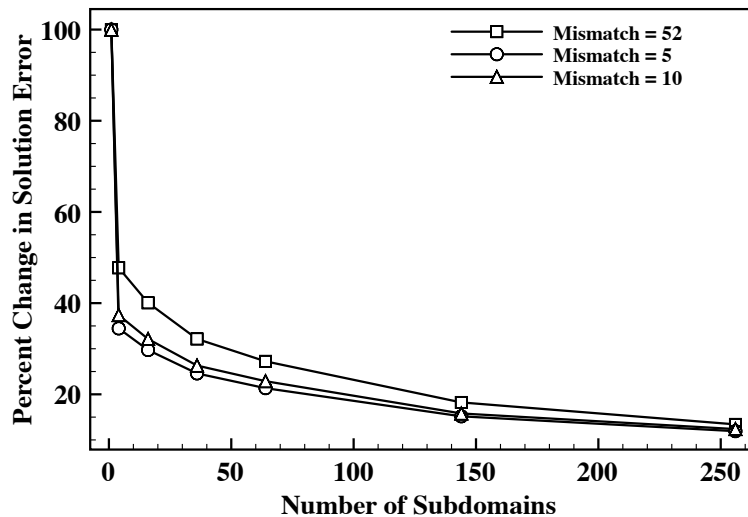
Figure 7.15: Percent change in solution error $\%\Delta e$ by solving the smaller subdomain boundary value problem under a traction controlled punch.

applying displacement boundary conditions. This is because the boundary displacements match for both the homogeneous and heterogenous solution spaces and the only error is arising from the projection of the wrong boundary conditions on the interior parts of the subdomains. On the other hand, when applying the traction boundary condition, the displacement of the circular region where the tractions are applied do not match for the homogeneous and heterogenous bodies. Thus in this case, we have an additional source of error.

7.4.2 Effect of Choosing Some Subdomains on Enhancing Homogeneous Solution

It is realistic to assume that under most circumstances we only want to solve a specified number of subdomains whose error indicator ζ_k are above some tolerance. We can set a criteria to include only a certain number of subdomains by considering

$$\zeta_{\text{limit}} = max(\zeta_k) - \alpha(max(\zeta_k) - min(\zeta_k)) \tag{7.4.2}$$

where $0.0 \leq \alpha \leq 1.0$ is a user defined constant. If we want all the subdomains to be

included in the analysis then $\alpha = 1$, otherwise only the subdomains whose error exceeds ζ_{limit} are used. It can be computationally expensive to solve all the subdomains however the added benefit on enhancing the homogeneous solution is not clear. To analyze this effect we consider the displacement controlled punch scenario that is partitioned into $8 \times 8 \times 1$ subdomains. The scaling factor α is varied and the complete boundary value problem is solved to obtain the homogeneous solution which is updated with the local subdomain solution. The results for a mismatch ratio $\kappa = 52$ are summarized in Table. 7.6 and Figure. 7.16. It's interesting to note that for $\alpha = 0.8$ the drop in the %Δe change is slight however the number of subdomains solved drops significantly. This can significantly reduce the computational cost with minimal effect on the results. It should be noted however, that using very few subdomains would result in a very small enhancement in the solution space. This is clear when using an $\alpha = 0.2$, which resulted in using only 4 subdomains and in turn a %Δe of only 3.66% was achieved. Additionaly, to illustrate the process, Figure. 7.17 shows the solved subdomains and the updated homogeneous solution for the case with $\alpha = 0.8$.

Table 7.6: Effect of number of subdomains used on improving solution

Number Subdomain	α	$\frac{\zeta}{\|\|\mathbf{u}^{*,h}\|\|_{E(\Omega)}}$	$\frac{\|\|\mathbf{u}^h - \mathbf{u}^{*,h}\|\|_{E(\Omega)}}{\|\|\mathbf{u}^{*,h}\|\|_{E(\Omega)}}$	$\frac{\|\|\mathbf{u}^h - \tilde{\mathbf{u}}^{*,h}\|\|_{E(\Omega)}}{\|\|\mathbf{u}^{*,h}\|\|_{E(\Omega)}}$	%Δe
64	1	4.068	2.754	1.889	31.4
30	0.8	4.068	2.754	1.991	27.6
24	0.6	4.068	2.754	2.093	23.9
14	0.4	4.068	2.754	2.358	14.4
4	0.2	4.068	2.754	2.653	3.66
4	0.05	4.068	2.754	2.653	3.66
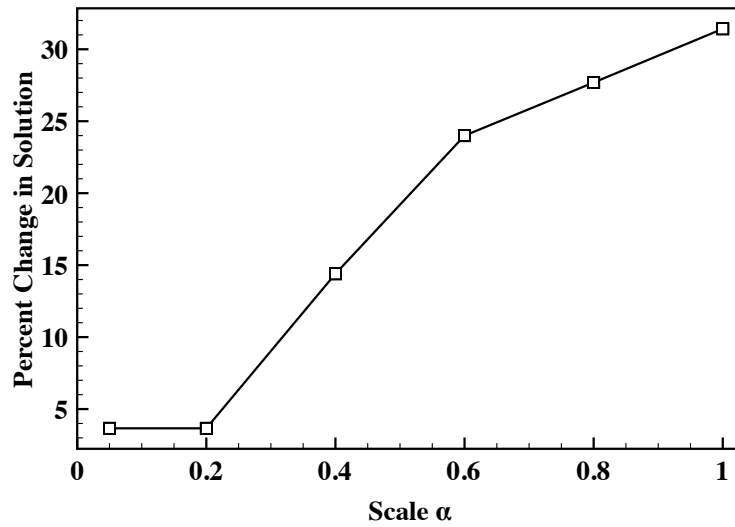
Figure 7.16: Percent change in solution error $\%\Delta e$ by choosing some subdomains in the $8 \times 8 \times 1$ partition.
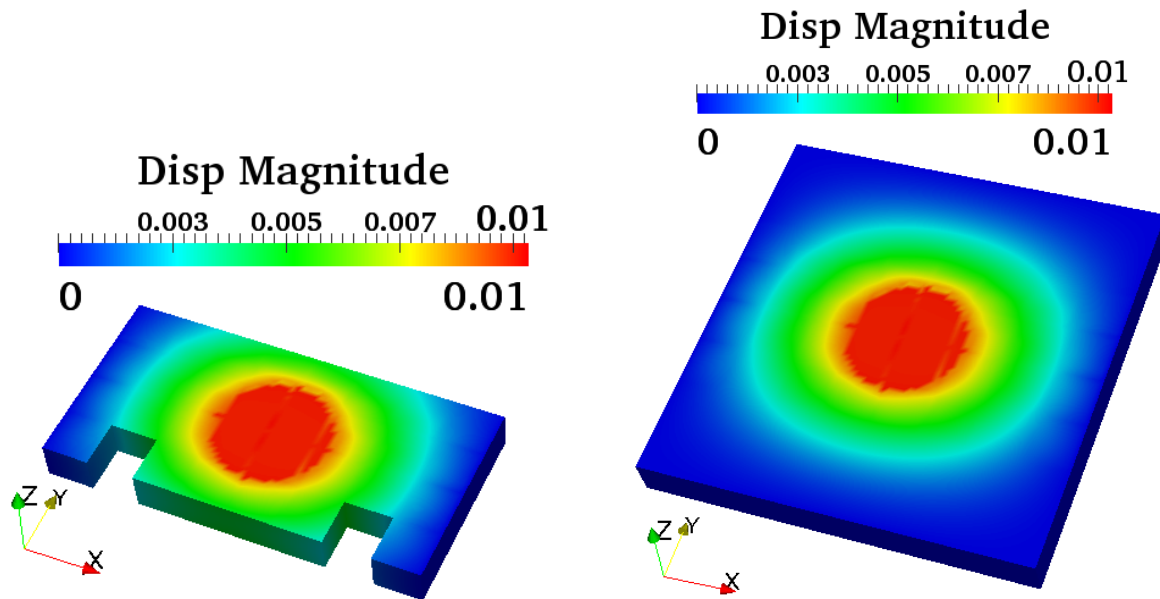
Figure 7.17: Displacement contours for $\kappa = 52$ of 1) Solved subdomains on the left 2) Updated solution $\tilde{\mathbf{u}}$ on the right for $\alpha = 0.8$.

7.5 Multiscale Analysis of Plate with Fiber Radius of 0.01m

In this section we will consider a microstructure that is more challenging. The same boundary conditions are imposed as in the previous section. A traction controlled punch in the center is applied with load $t = [0, 0, -0.1]$. The microstructure geometry is shown in Figure. 7.19. Specifically, a fiber radius of $0.01m$ is assumed which results in 159 fibers with a fiber volume fraction of 0.5. We will only consider the material property with $\kappa = 52$, which gives us a carbon fiber.
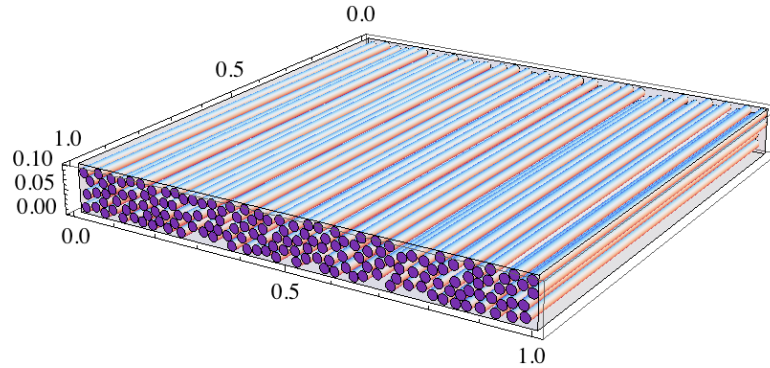
Figure 7.18: Fibers with radius 0.01m in a matrix

Due to the fineness of the microstructure it is very difficult in this case to solve the exact boundary value problem and thus cannot compare the homogeneous solution to the exact solution. Requiring 8 nodes across a fiber would result in almost 19 million degrees of freedom. This is assuming a square non-conforming mesh. Solving this is computationally very expensive therefore, we don't attempt it. To conduct the multiscale analysis we must use different mesh sizes for the subdomain that includes microstructure and the subdomain without the microstructure. To capture the details of the fibers we utilize a finer mesh for these small scale problems and connect the two scales together with Algorithm. 1. For this analysis the global domain is sub-structured into $10 \times 10 \times 1$ subdomains. The mesh on the subdomains that include the microstructure was set to $51 \times 51 \times 51$ nodes, while the subdomains without the microstructure is $9 \times 9 \times 9$ nodes. This results in a mesh size $81 \times 81 \times 9$ nodes on the global domain to solve the homogeneous problem.

The results of this simulation are shown in Figure. 7.19, where the equivalent stress σ_{eq}(Von-Mises) is plotted for both the homogeneous solution and for parts of the subdomains that have high local error indicators. Figure. 7.20, plots the ratio of ζ_k / ζ_k^{max} vs the

subdomain number showing where the maximum error indicators occur. It's clear that the equivalent stress ranges are very different between the microsturcture and the homogenous solution, this is of course to be expected. Clearly, this variation in σ_{eq} can be very important for damage analysis. As a comparison the average $\langle \sigma_{eq} \rangle$ stress in each subdomain with and without microstructure is computed and their ratio is plotted in Figure. 7.21. We notice this ratio fluctuates with some values over 1 and some below, meaning that in some subdomains the average σ_{eq} with microstructure is higher than without while in others the opposite is true.
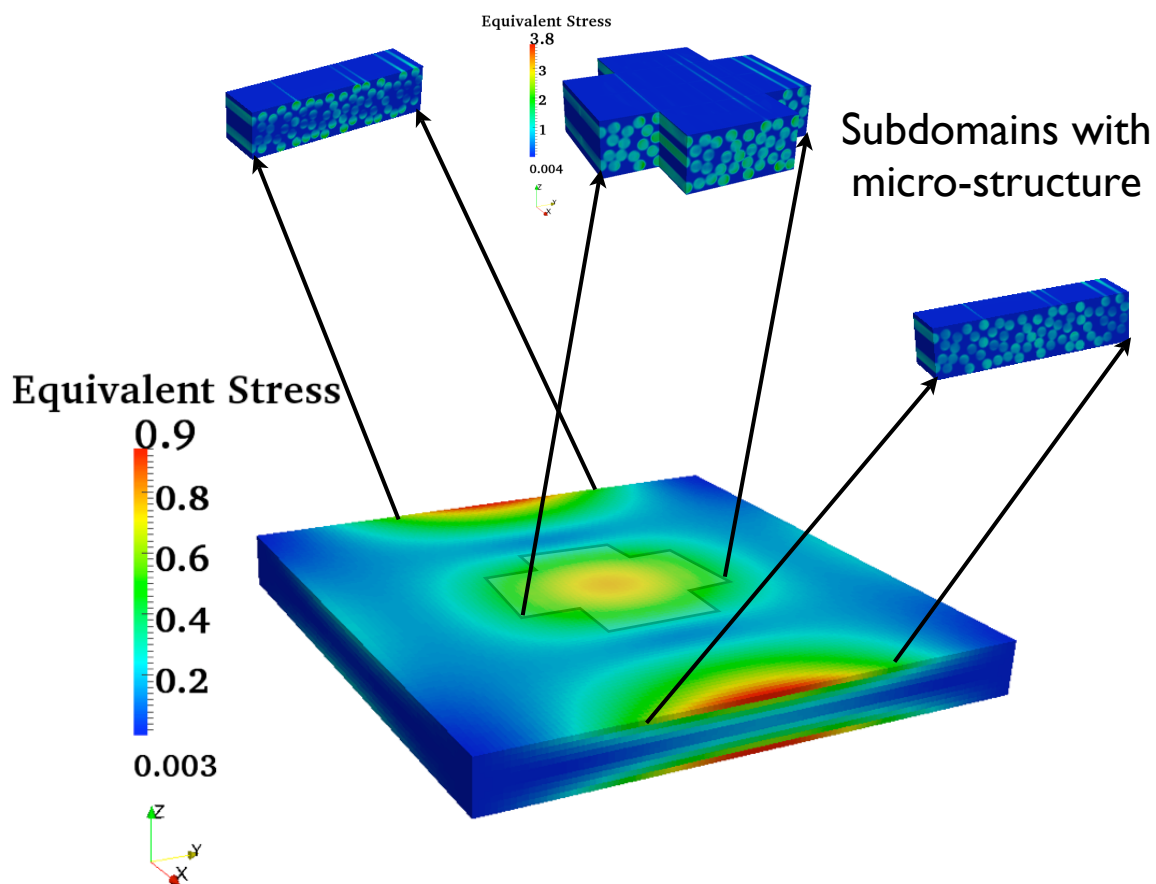
Figure 7.19: Contour solutions of the equivalent stress $\boldsymbol{\sigma}_{eq}$ for the case of fibers with radius 0.01m. The complete domain shows the solution for the homogenized body and the extended sections show the subdomains with fibers used to update the solutions space. We note the difference in the contour results and variation in $\boldsymbol{\sigma}_{eq}$.
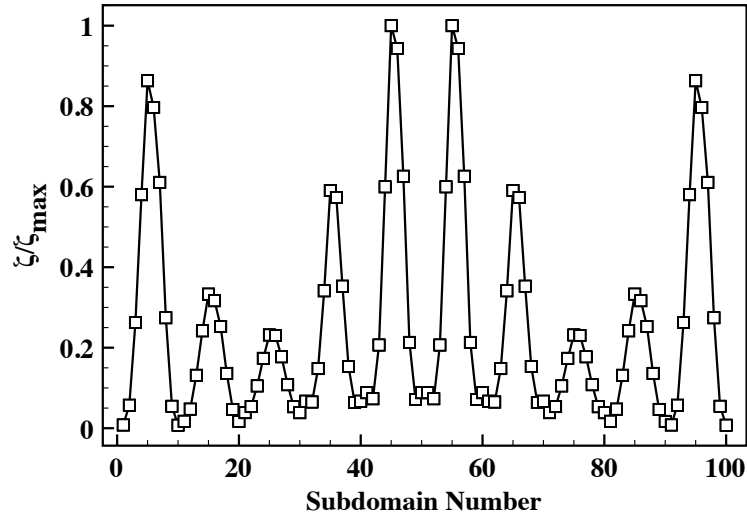
Figure 7.20: This figure shows the variation of the fraction $\frac{\zeta_k}{\zeta_k^{max}}$ in each subdomain. This identifies the regions with high local error.
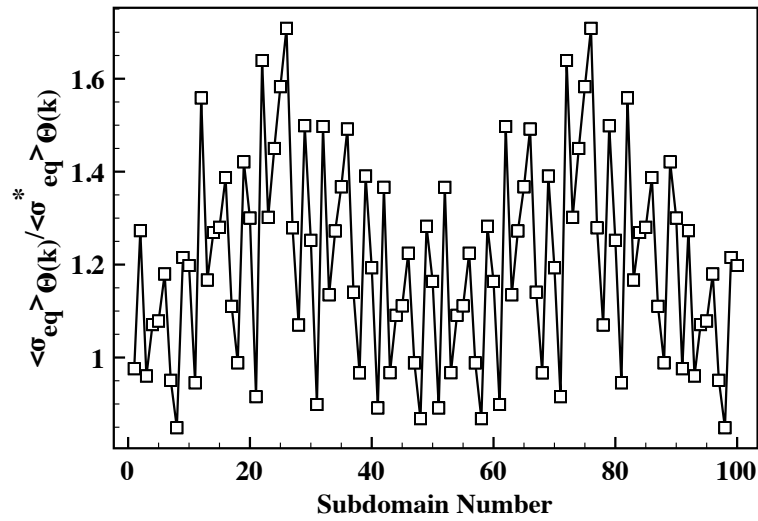
Figure 7.21: Plot of the ratio of the average equivalent stress from the subdomain calculation to the average equivalent stress of homogenized solution in each subdomain.

Chapter 8

Multiscale Modeling with Large Deformations: Global Error Analysis

Deriving an exact upper bound on the modeling error for nonlinear elasticity is a very difficult task if not impossible. Hence, in this chapter we will utilize the error bounds derived in Chapter. 6 in Section. 6.2 as an indicator of the error for the case of large deformations. In looking at large deformation we solve a nonlinear problem and refer to the formulation of nonlinear finite elements described in Chapter. 3. For this analysis we limit our interest to a Kirchhoff-St.Venant material model defined as

$$\mathbf{S} = \mathbb{C}\mathbf{E} \tag{8.0.1}$$

Where, $\mathbb{C} = \frac{\partial \mathbf{S}}{\partial \mathbf{E}}$. This model is generally satisfactory for deformations that involve large displacements but relatively small strains. Since we are interested in fiber composites this model is therefore satisfactory. Since we are limiting ourselves to this model, all results that ensue are only valid for this type of material.

As stated before, we refer to the upper bound derived for the case of linear elasticity as an error indicator for simulations with large deformations. Specifically, we will assume the error bound to be defined on the reference configuration and we then have,

$$\zeta^2 = \int_{\Omega_0} \mathcal{J}_0 \nabla_X \mathbf{u}^* : \mathbb{C} \mathcal{J}_0 \nabla_X \mathbf{u}^* d\Omega_0 \tag{8.0.2}$$

where again $\mathcal{J}_0 = \mathbf{I} - \mathbb{C}^{-1} \mathbb{C}^*$ and ∇_X is the gradient operator with respect to the referential positions X_I. Since Eqn. 8.0.2 is not derived but assumed, the first set of actions is to understand its response under large deformations. The questions that come to mind are

1. Does it always bound the exact error?

2. Under what circumstances does it fail?

In this chapter we attempt to answer these questions. We construct some basic examples to elucidate the behavior of the error estimate. This will be conducted purely in a numerically setting. Three loading scenarios are considered. First, simple shear along the fiber direction. Second, simple shear perpendicular to the fiber direction and third, bending of a beam. Each case will be discussed independently. First let's consider the general case of simple shear as shown in Figure. 8.1 and thus we have

$$x_1 = X_1 + KX_2$$
$$x_2 = X_2$$
$$x_3 = X_3 \tag{8.0.3}$$

and therefore, we can calculate the lagrangian strain $\mathbf{E}$ to be

$$\mathbf{E} = \begin{bmatrix} 0 & \frac{1}{2}K & 0 \\ \frac{1}{2}K & \frac{1}{2}K^2 & 0 \\ 0 & 0 & 0 \end{bmatrix} \tag{8.0.4}$$

where K is a constant. We note that to produce this exactly, we must apply the exact displacement boundary conditions on the block. However, for our purposes we want to apply a transverse shear load on the surface of interest instead of pure displacement boundary conditions. This is mainly to increase the error between the homogeneous and heterogeneous
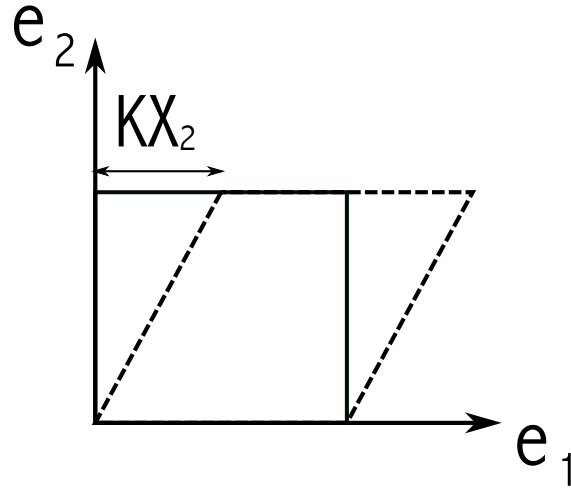
Figure 8.1: This is a schematic of a simple shear deformation

solution. Although the above is the exact formulation for simple shear, we apply the set of boundary conditions shown in Figure. 8.2. Where the traction is applied on different faces depending on if the load is parallel or perpendicular to the fiber direction. When referring to simple shear conditions, we are implying the boundary condition stated in Figure. 8.2.

All the tests are conducted for a fiber volume fraction of $\nu_f = 0.5$ and to reduce the uncertainty the fibers are placed in the body symmetrically. The conducted analysis will mainly examine whether using equation Eqn. 8.0.2 will bound the real error. To do this we will compare ζ to the exact error and plot the ratio $\frac{||\mathbf{u}-\mathbf{u}^*||_{E(\Omega)}}{\zeta}$ as a function of the applied traction $\mathbf{t}$.

8.1   Simple Shear of a Block: Along Fiber Direction

The first set of parametric tests are conducted on a $1m \times 1m \times 1m$ block in simple shear with a traction load parallel to the fiber direction. The traction is loaded incrementally to evaluate the change in the error prediction as a function of load. Additionally, the number of fibers are increased and the same loading conditions are applied. The number of fibers used was 4,16 and 36. Two material mismatch ratios are considered with $\kappa = 5$ and 52. This is to see if the material type has an effect on the analysis. The mesh size depends on the number of fibers added to the block. As usual we maintained approximately 8 elements across each fiber.
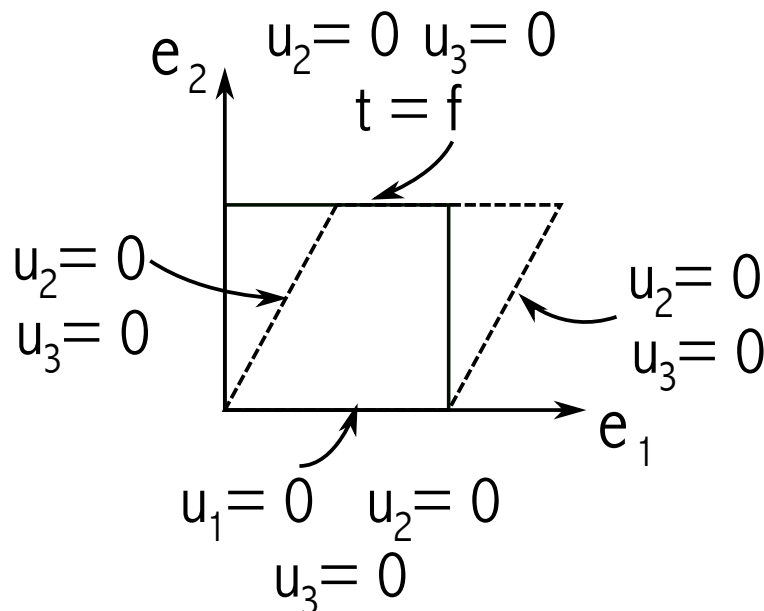
Figure 8.2: Simple shear with traction boundary condition and the applied displacement constraints on the different faces. These are the conditions used for the computational simulations

For the case of $\kappa = 52$ the final applied traction was $t_1 = 3.0N/m^2$ while for $\kappa = 5$ the final applied traction was $t_1 = 2.6N/m^2$ and both were applied on the surface $X_2 = 1.0$. The reason for different max loadings for the two mismatch ratios is shear locking occurring at the different loads which resulted in a lack of convergence with newton's method for the heterogenous solution. As mentioned the loading was applied incrementally and Figure. 8.3 shows the displacement solution contour for the case of 36 fibers at traction loading $t_1 = 2.0N/m^2$ and with a mismatch ration of $\kappa = 5$.

To analyze how well the error bound ζ works we plot a normalized load t_1/E_m vs the ratio of the exact error divided by the predicted error. Specifically, as previously mentioned $\frac{||\mathbf{u} - \mathbf{u}^*||_{E(\Omega)}}{\zeta}$ is evaluated. The key is that this ratio remains under unity, therefore ζ maintains an upper bound estimate on the error. Figure. 8.4 shows the plots of the results from the parametric tests for both mismatch ratios of $\kappa = 5$ and 52. The desired ratio remains below unity, however the error estimate deteriorates with increasing load. One thing to notice, is that for mismatch ratio of $\kappa = 5$ the loss in accuracy is more pronounced and at loading ratio of 0.41 a small jump in the trend occurs. The jump can be attributed
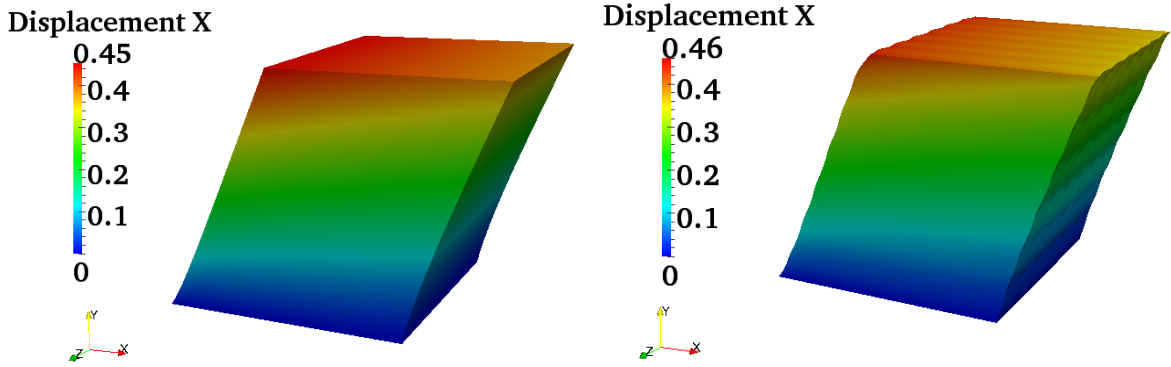
Figure 8.3: Displacement contours for load parallel to fiber with 36 fiber and $\kappa = 5$ at load increment $t_1 = 2.0 N/m^2$ for a) Homogeneous body is shown on the left b) Heterogeneous body is on the right

to some shear locking in the heterogeneous solution due to the large deformations.
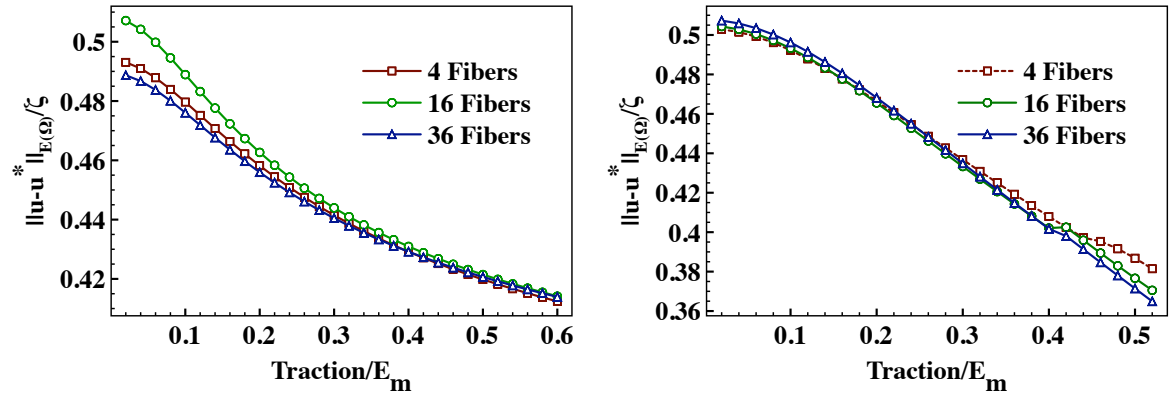
Figure 8.4: These plots show the performance of the global error indicator ζ under large deformations for 1) $\kappa = 52$ on the left and for 2) $\kappa = 5$ on the right under loading parallel to the fiber.

8.2   Simple Shear of a Block: Perpendicular to Fiber Direction

The next set of parametric tests is simple shear with a load perpendicular to the fiber direction. As previously described the same parameters are changed for this study as they were for the case of simple shear with a load parallel to the fiber. For a mismatch ratio of $\kappa = 52$, the maximum traction is set to $t_2 = 1.2 N/m^2$ while for a mismatch

ratio of $\kappa = 5$ the maximum traction is set to $t_2 = 1.1 N/m^2$. The traction is increased incrementally as previously described. Again, the variation of maximum loads is due to shear locking occurring for $\kappa = 5$. The displacement contours for the homogeneous and heterogenous results are shown in Figure. 8.5 the case of 36 fibers at a traction value of $t_2 = 0.5 N/m^2$ and a material mismatch of $\kappa = 5$.

The results from the parametric studies are shown in Figure. 8.6. They show the evolution of the error ratios as a function of load. In contrast to the simple shear with load parallel to the fiber, the error ratios do not change as dramatically. In fact, with increasing load ζ gets closer to the actual error. This is more pronounced for mismatch ration $\kappa = 5$. We also observe a dependence on the number of fibers used. For example there is a large change for both mismatch ratios when going from 4 fibers to 16 fibers. However, the change is smaller when increasing fibers from 16 to 36. The change is negligible for $\kappa = 52$. This dependence makes sense from the point of you that as you increase the number of fibers the response from an average point of you converges to some value.
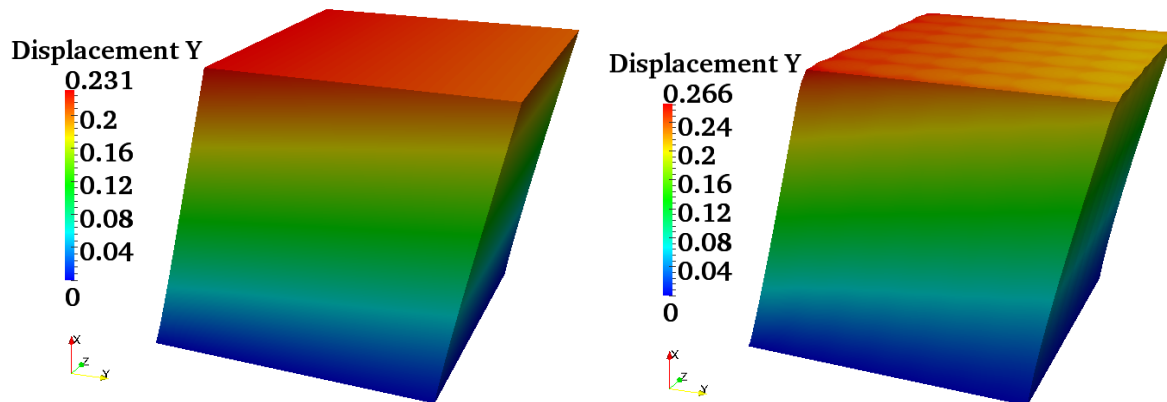
Figure 8.5: Displacement contours for load perpendicular to fiber with 36 fibers and $\kappa = 5$ at load increment $t_2 = 0.5 N/m^2$ for a) Homogeneous body is shown on the left b) Heterogeneous body is on the right

8.3 Transverse Shear Loading of a Beam

This is the last set of parametric studies used to understand the behavior of the error indicator defined in Eqn. 8.0.2. In this part we look at the case of transverse shear of a beam of dimensions $1m \times 0.1m \times 0.1m$. A traction is applied on the surface that is

Figure 8.6: These plots show the performance of the global error indicator ζ under large deformations for 1) $\kappa = 52$ on the left and for 2) $\kappa = 5$ on the right under loading perpendicular to the fiber.

perpendicular to the fibers as shown in Figure. 8.7. The fibers are arranged so that they are placed along the length of the beam. This test will produce large deformations that include both displacements and rotations. The same set of fibers and mismatch ratios κ are used for this study. For a mismatch ratio of $\kappa = 52$, the maximum traction is $t_3 = 0.2 N/m^2$ while for a mismatch ratio of $\kappa = 5$ the maximum traction is $t_3 = 0.2 N/m^2$. The displacement contours for the homogeneous and heterogeneous results are shown in Figure. 8.8 for the case of 36 fibers and mismatch ratio of $\kappa = 5$ at load increment $t_3 = 0.15 N/m^2$.

Figure 8.7: Figure of a beam under transverse shear loading conditions. The fibers are assumed to go along the length of the beam.

The results from the parametric studies are shown in Figure. 8.9. The error indicator ζ for this test performs poorly in predicting the error. However, it remains an upper bound. The ratio of exact error to ζ does not change significantly for the case of 16 and 36 fibers for both mismatch ratios. However, the case of 4 fibers behaves in an unpredictable manner for both mismatch ratios. In fact for mismatch ration $\kappa = 52$, ζ approaches the exact error while for mismatch ration $\kappa = 5$, ζ deviates away from the exact error. Once again, we notice that the results are very similar between cases of 16 and 36 fibers.
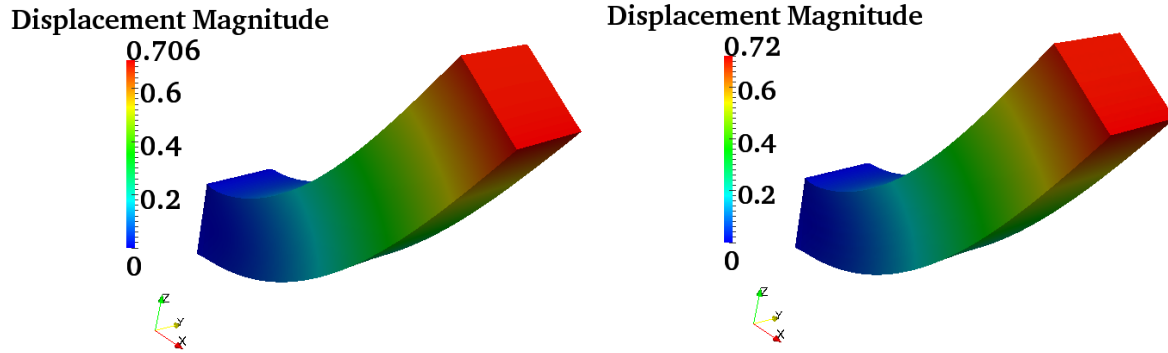
Figure 8.8: Displacement contours for transverse shear loading with 36 fibers and $\kappa = 5$ at load increment $t_3 = 0.15 N/m^2$ for 1) Homogeneous body is shown on the left b) Heterogeneous body is on the right
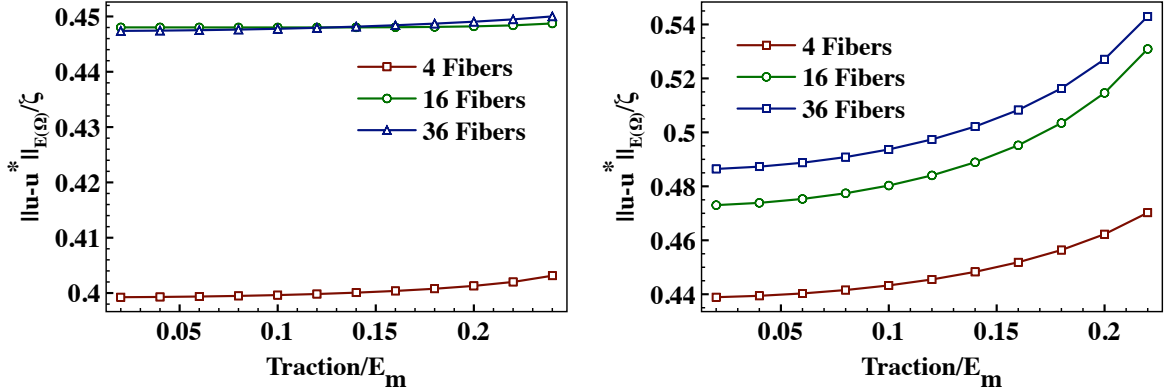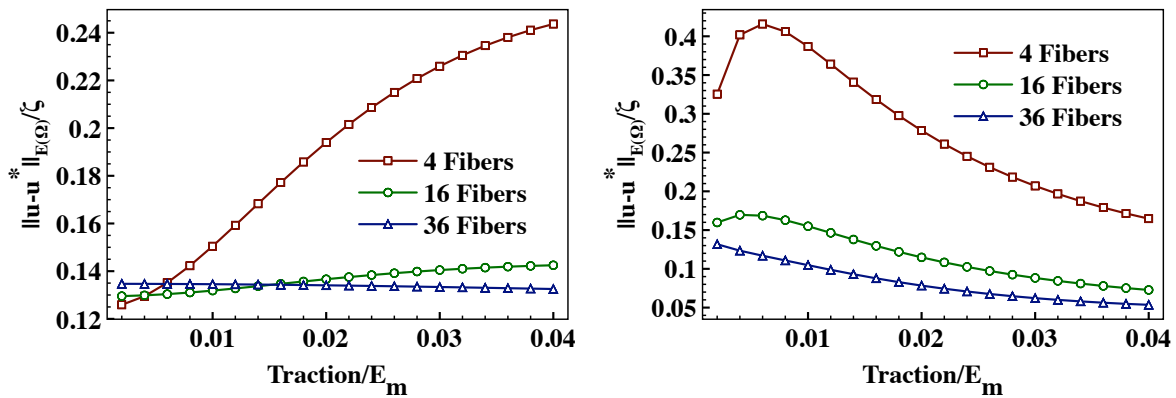

Figure 8.9: These plots show the performance of the global error indicator ζ under large deformations for 1) $\kappa = 52$ on the left and for 2) $\kappa = 5$ on the right under transverse shear loading.

8.4   General Remarks on the Error Indicator ζ

From the conducted tests we notice that ζ remains an upper bound for all the test cases conducted. However, there is no mathematical reason for this to hold under other circumstances. We also note that the general behavior of the error indicator depends on the type of boundary value problem that is being solved. This further complicates matters because given a boundary value problem we are not able to a-priori predict the trend in which the error indicator will evolve as a function of deformation.

With this in mind, we can still use ζ to adaptively choose the subdomains of interest to solve smaller microstructural problems. The same process that was used for the case of linear elasticity is adopted here with Eqn. 8.0.2 serving as an error indicator. The procedure and results will be discussed in the next chapter.

Chapter 9

Nonlinear Multiscale Subdomain Construction

In this chapter the subdomain construction follows what was presented in Chapter. 7. The only difference is the local boundary value problem that defines each subdomain problem. The problem is defined in the context of nonlinear elasticity with the weak form expressed as

$$\int_{\Theta_k} \nabla_{\mathbf{X}} \mathbf{v} : (\mathbf{F}\mathbb{C}\mathbf{E})^T d\Omega_{0,k} = \int_{\partial \Theta_{k,\mathbf{t}}} \mathbf{v} \cdot \mathbf{T} d\Gamma_{0,k} + \int_{\Theta_k} \rho_0 \mathbf{v} \cdot \mathbf{f} d\Omega_{0,k} \qquad (9.0.1)$$

with displacement boundary conditions being projected on to the subdomain from the homogeneous solution. Specifically, we have $\tilde{\mathbf{u}}|_{\partial \Theta_{k,\mathbf{u}}} = \mathbf{u}^*|_{\partial \Theta_{k,\mathbf{u}}}$. However, in addition the solution from the homogeneous boundary value problem is also used as an initial guess for the Newton's iteration. Therefore, we project $\tilde{\mathbf{u}}|_{\Theta_k} = \mathbf{u}^*|_{\Theta_k}$ as the first iteration.

The domain Ω is deconstructed into subdomains as was presented in Chapter 7 and the local error indicators are constructed by simply breaking the integral over each subdomain such that,

$$\zeta^2 = \sum_{k=1}^{N} \zeta_k^2 \qquad (9.0.2)$$

with

$$\zeta_k^2 = \int_{\Theta_k} \mathcal{J}_0 \nabla_X \mathbf{u}^* : \mathbb{C}\mathcal{J}_0 \nabla_X \mathbf{u}^* d\Omega_{0,k} \tag{9.0.3}$$

and $\mathcal{J}_0 = \mathbf{I} - \mathbb{C}^{-1}\mathbb{C}^*$. Note all integrals are over the reference volumes.

9.1 Multiscale Modeling of Plate with Fiber Radius of 0.04m

The example of a plate in bending that was used for the analysis of multiscale modeling in linear elasticity is used again in this section. The same configuration is used, where the domain has 9 fibers and we conduct the analysis for multiple material mismatch ratios and for both displacement and traction control boundary conditions. The same mismatch ratios as described previously are used. To guarantee convergence in an efficient way, the load is applied incrementally. For the traction controlled punch the following condition is prescribed $\mathbf{t} = [0.0, 0.0, -0.1t - 0.1]$ and it's applied in a region defined by a circle with radius $r = 0.15$ and centered in the middle of the plate. The time varied from $t = [1, 2, 3, 4, 5]$. While for the displacement controlled punch, we have $\mathbf{u} = [0.0, 0.0, -0.001t - 0.001]$ with $t = 1 : 50$ in increments of 1. A small displacement increment was needed for Newton's method to converge.

9.1.1 Effect of Number of Subdomains on Enhancing Homogeneous Solution

We initially look at the global error value at each increment for each material mismatch ratio condition. The results for both the traction and displacement controlled punch are summarized in Tables. 9.1-Table. 9.2. Since the displacement controlled punch required more iterations for Newton's method to converge we only show every 10th increment. The results show that the predicted errors are upper bounds and over-predict the error in this case by a factor of 2-3. This factor depends on the mismatch ratio and the load increment as was previously observed.

We now break the domain Ω_0 into subdomains of different size and solve these smaller boundary value problems defined in Eqn. 9.0.1. The analysis is conducted for a

Table 9.1: Traction controlled punch: global error for different time increments and different mismatch ratios

	Increment	1	2	3	4	5
	$\frac{\zeta}{\|\|\mathbf{u}^{*,h}\|\|_{E(\Omega)}}$	0.941	0.906	0.881	0.863	0.849
Mismatch 5	$\frac{\|\|\mathbf{u}^h - \mathbf{u}^{*,h}\|\|_{E(\Omega)}}{\|\|\mathbf{u}^{*,h}\|\|_{E(\Omega)}}$	0.452	0.413	0.385	0.365	0.353
	$\frac{\zeta}{\|\|\mathbf{u}^h - \mathbf{u}^{*,h}\|\|_{E(\Omega)}}$	2.079	2.195	2.291	2.361	2.405
	$\frac{\zeta}{\|\|\mathbf{u}^*\|\|_{E(\Omega)}}$	1.385	1.333	1.288	1.252	1.223
Mismatch 10	$\frac{\|\|\mathbf{u}^h - \mathbf{u}^{*,h}\|\|_{E(\Omega)}}{\|\|\mathbf{u}^{*,h}\|\|_{E(\Omega)}}$	0.643	0.607	0.573	0.545	0.524
	$\frac{\zeta}{\|\|\mathbf{u}^h - \mathbf{u}^{*,h}\|\|_{E(\Omega)}}$	2.153	2.197	2.249	2.296	2.332
	$\frac{\zeta}{\|\|\mathbf{u}^{*,h}\|\|_{E(\Omega)}}$	2.513	2.487	2.457	2.423	2.388
Mismatch 52	$\frac{\|\|\mathbf{u}^h - \mathbf{u}^{*,h}\|\|_{E(\Omega)}}{\|\|\mathbf{u}^{*,h}\|\|_{E(\Omega)}}$	0.846	0.845	0.843	0.838	0.832
	$\frac{\zeta}{\|\|\mathbf{u}^h - \mathbf{u}^{*,h}\|\|_{E(\Omega)}}$	2.970	2.943	2.915	2.891	2.871

Table 9.2: Displacement controlled punch: global errors for different time increments and different mismatch ratios

	Increment	10	20	30	40	50
	$\frac{\zeta}{\|\|\mathbf{u}^{*,h}\|\|_{E(\Omega)}}$	0.999	0.988	0.973	0.956	0.938
Mismatch 5	$\frac{\|\|\mathbf{u}^h - \mathbf{u}^{*,h}\|\|_{E(\Omega)}}{\|\|\mathbf{u}^{*,h}\|\|_{E(\Omega)}}$	0.442	0.434	0.423	0.411	0.398
	$\frac{\zeta}{\|\|\mathbf{u}^h - \mathbf{u}^{*,h}\|\|_{E(\Omega)}}$	2.261	2.277	2.299	2.326	2.356
	$\frac{\zeta}{\|\|\mathbf{u}^{*,h}\|\|_{E(\Omega)}}$	1.427	1.407	1.379	1.349	1.316
Mismatch 10	$\frac{\|\|\mathbf{u}^h - \mathbf{u}^{|*,h}\|\|_{E(\Omega)}}{\|\|\mathbf{u}^{*,h}\|\|_{E(\Omega)}}$	0.589	0.578	0.564	0.548	0.531
	$\frac{\zeta}{\|\|\mathbf{u}^h - \mathbf{u}^{*,h}\|\|_{E(\Omega)}}$	2.424	2.433	2.446	2.461	2.477
	$\frac{\zeta}{\|\|\mathbf{u}^{*,h}\|\|_{E(\Omega)}}$	2.456	2.411	2.356	2.293	2.226
Mismatch 52	$\frac{\|\|\mathbf{u}^h - \mathbf{u}^{*,h}\|\|_{E(\Omega)}}{\|\|\mathbf{u}^{*,h}\|\|_{E(\Omega)}}$	0.789	0.777	0.762	0.745	0.727
	$\frac{\zeta}{\|\|\mathbf{u}^h - \mathbf{u}^{*,h}\|\|_{E(\Omega)}}$	3.112	3.104	3.093	3.079	3.062

total number of subdomains ranging from 4 to 81 subdomains. The percent change in solution error (%Δe) defined in Eqn. 7.4.1 is calculated and plotted as a function of total number of subdomains and load increment. The results for each mismatch ratio are shown in Figure. 9.1 for the traction controlled punch and in Figure. 9.2 for the displacement controlled punch.

Figure 9.1: Percent change in error %Δe for traction controlled punch for 1) $\kappa = 52$ which is shown in the top left, 2) $\kappa = 5$ which is shown in the top right, 3) $\kappa = 10$ which is shown in the bottom center

All the subdomain solutions were included in the update process. The results indicate a similar trend seen in the analysis conducted for linear elasticity. The subdomain solutions can reduce the error of the homogenized solution significantly. Clearly, the larger the size of the subdomains the better the results. Also, there is greater percentage of enhancement when using the displacement controlled punch.
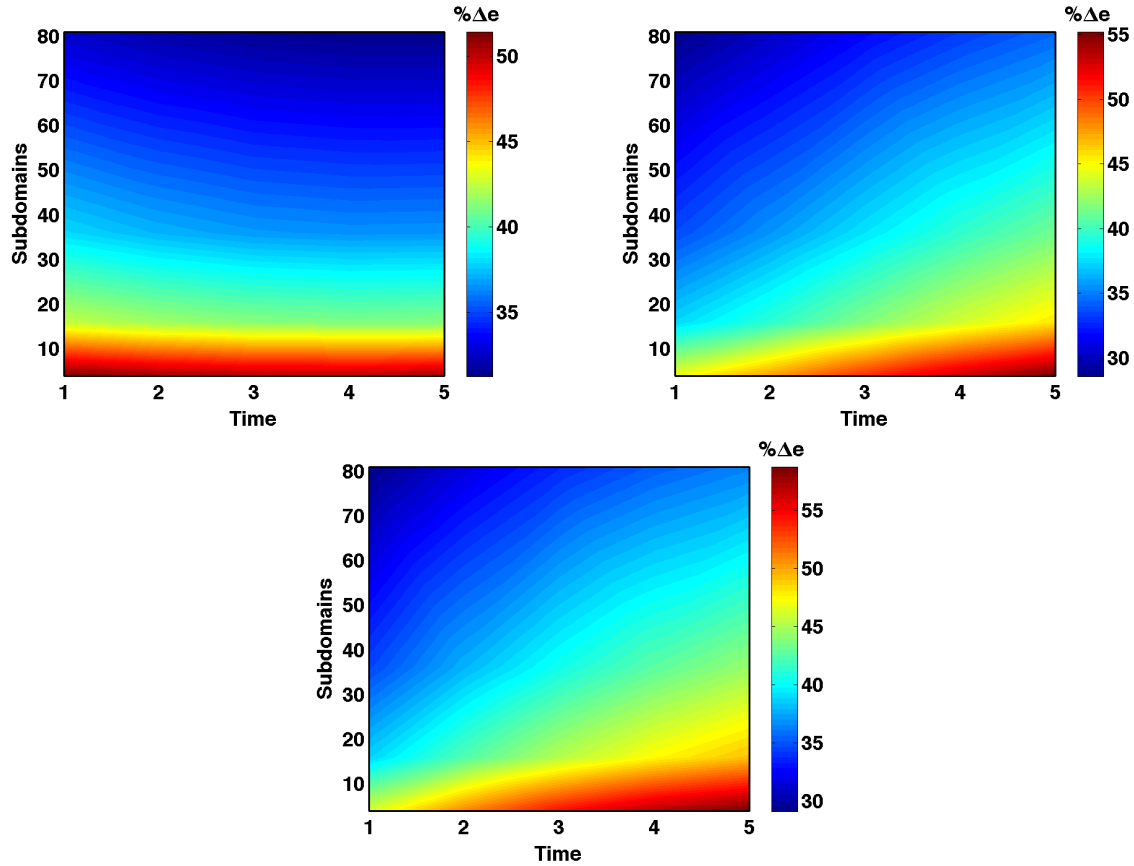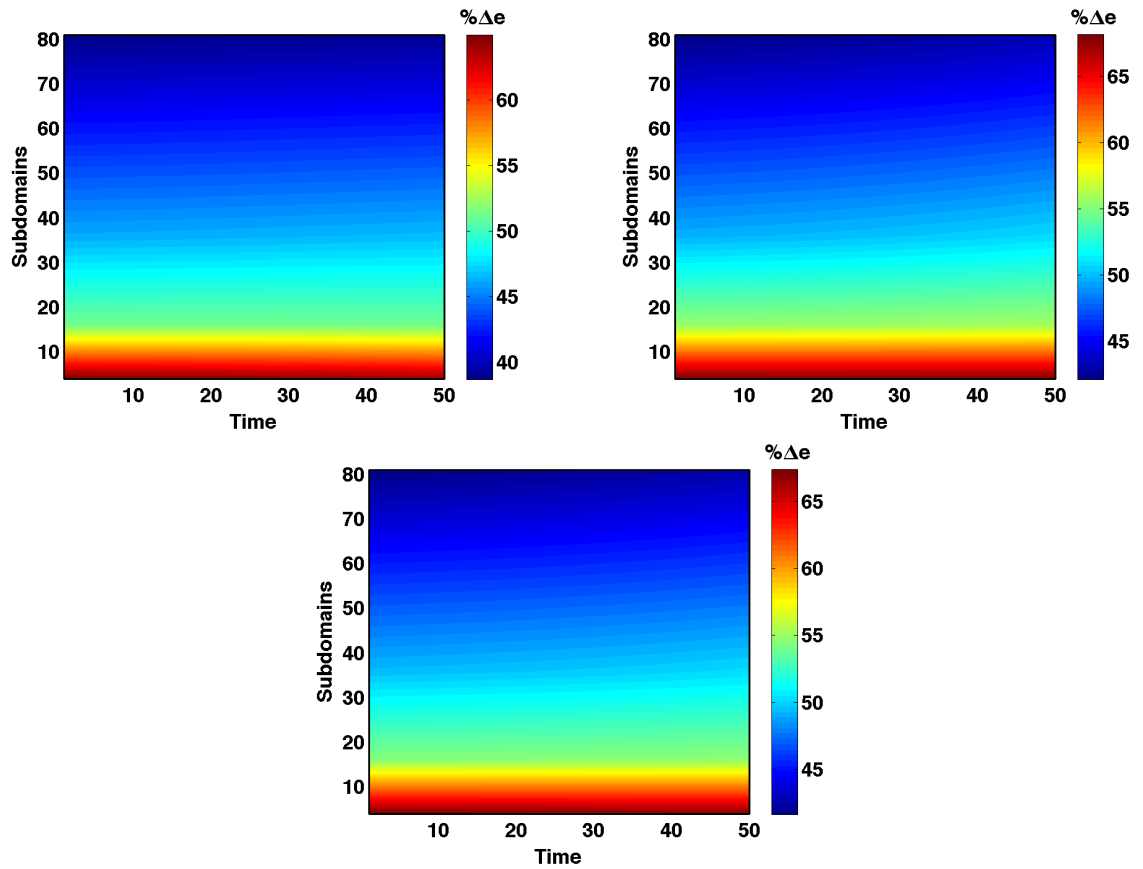
Figure 9.2: Percent change in error %Δe for displacement controlled punch for 1) $\kappa = 52$ which is shown in the top left, 2) $\kappa = 5$ which is shown in the top right, 3) $\kappa = 10$ which is shown in the bottom center

9.1.2 Effect of Choosing Some Subdomains on Enhancing Homogeneous Solution

In this section as previously shown for the case of small strains, we explore the effect of choosing only some of the subdomains in the solution space. Recall the criteria used to determine which subdomains to use is defined in Subsection. 7.4.2 in Eqn. 7.4.2. For the analysis we choose the displacement controlled punch with material mismatch ratio $\kappa = 52$ as used in the previous section. The domain is broken up into $9 \times 9 \times 1$ subdomains and α Eqn. 7.4.2 is varied to see its effect on the solution space. The value $\%\Delta e$ is calculated as defined in Eqn. 7.4.1. We note that for large deformations the number of subdomains utilized at a given increment can change as shown in Figure. 9.3. This is because depending on the load increment the local error in subdomains will change and some might increase and become larger than the imposed criteria. Therefore, we look at the last time increment $t = 50$ to analyze the effect of using some of the subdomains. The results are summarized in Table. 9.3 and in Figure. 9.4. We note the significant reduction of number of subdomains used for $\alpha = 0.8$ from 81 subdomains to 37 subdomains. However, the drop in $\%\Delta e$ is small. Specifically it drops from a 39% change in error to a 28% change in error. This clearly reduces the computational effort while maintaining a significant improvement in the solution space. As in the case for small strains the less subdomains we use the less we are able to improve our solution space as illustrated on Figure. 9.4.

Table 9.3: Effect of using some subdomains on improving solution for time increment $t = 50$

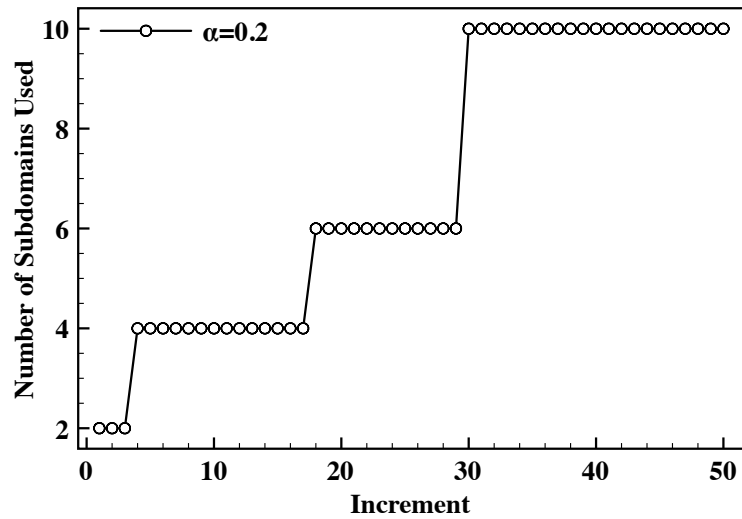| Number Subdomain	α	$\frac{\zeta}{||\mathbf{u}^{*,h}||_{E(\Omega)}}$	$\frac{||\mathbf{u}^h - \mathbf{u}^{*,h}||_{E(\Omega)}}{||\mathbf{u}^{*,h}||_{E(\Omega)}}$	$\frac{||\mathbf{u}^h - \tilde{\mathbf{u}}^{*,h}||_{E(\Omega)}}{||\mathbf{u}^{*,h}||_{E(\Omega)}}$	$\%\Delta e$
81	1	2.221	0.725	0.442	39.0
37	0.8	2.221	0.725	0.516	28.9
17	0.6	2.221	0.725	0.585	19.3
14	0.4	2.221	0.725	0.598	17.5
10	0.2	2.221	0.725	0.608	16.2
6	0.1	2.221	0.725	0.666	8.3

Figure 9.3: Number of subdomains used as a function of the time increament for $\alpha = 0.2$. We notice how the number of subdomains used can change. This is also true for other value of α.
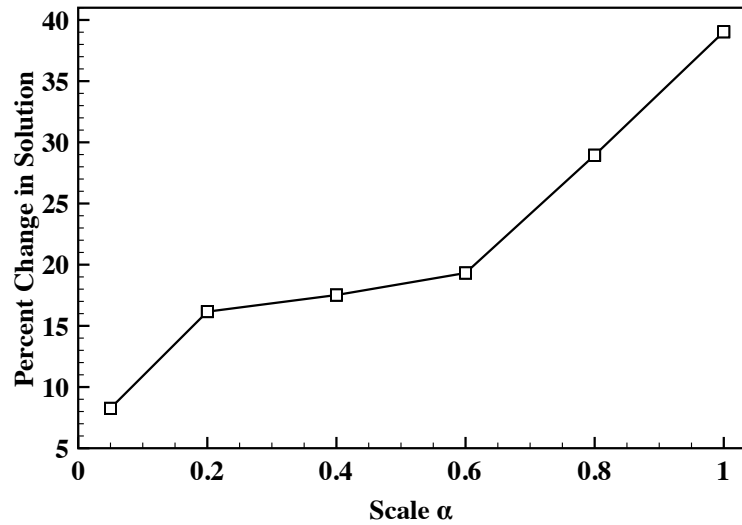

Figure 9.4: Percent change in solution error $\%\Delta e$ by choosing some subdomains in the solution space for time increment $t = 50$ and a domain broken up into $9 \times 9 \times 1$.

9.2   Multiscale Modeling of Plate with Fiber Radius 0.01m

In a similar fashion to the case of small strains we consider a more challenging micro-structure. A traction controlled punch in the center is applied with load $\mathbf{t} = [0, 0, -0.1t - 0.1]$ with $t = [1, 2, 3, 4, 5]$ as previously stated. The microstructure geometry is shown in Figure. 7.19. Specifically, a fiber radius of $0.01m$ is assumed which results in 159 fibers with a fiber volume fraction of 0.5. We will only consider the material property with mismatch ratio $\kappa = 52$, which gives us a carbon fiber.

To conduct the multiscale analysis we must use different mesh sizes for the subdomain that includes microstructure and the subdomain without the microstructure. To capture the details of the fibers we utilize a finer mesh for these small scale problems and connect the two scales together with Algorithm. 1. For this analysis the global domain is sub-structured into $10 \times 10 \times 1$ subdomains. The mesh on the subdomains that includes the microstructure was set to $51 \times 51 \times 51$ nodes, while the subdomains without the microstructure is $9 \times 9 \times 9$ nodes. This results in a mesh size $81 \times 81 \times 9$ nodes on the global domain to solve the homogeneous problem.

The results of this simulation are shown in Figure. 9.5, where the equivalent stress σ_{eq}(Von-Mises) is plotted for both the homogeneous solution and for parts of the subdomains that have high local error indicators, specifically an $\alpha = 0.8$ was used for this simulation. Figure. 9.6, plots the ratio of ζ_k / ζ_k^{max} vs the subdomain number showing where the maximum error indicators occur. It's clear that the equivalent stress ranges are very different between the microsturcture and the homogenous solution, this is of course to be expected. Clearly, this variation in σ_{eq} can be very important for damage analysis. As a comparison the average $\langle \sigma_{eq} \rangle$ stress in each subdomain with and without microstructure is computed and their ratio is plotted in Figure. 9.7. We notice this ratio fluctuates with some values over 1 and some below, meaning that in some subdomains the average σ_{eq} with microstructure is higher than without while in others the opposite is true.

9.3   Multiscale Modeling of Block in Shear Along Fiber

In this example we use the block in shear along the fiber direction that was used to asses the performance of the error indicator ζ as shown in section. 8.1. The global error results for a block in shear along the fiber direction are summarized in Figure. 8.4 and are
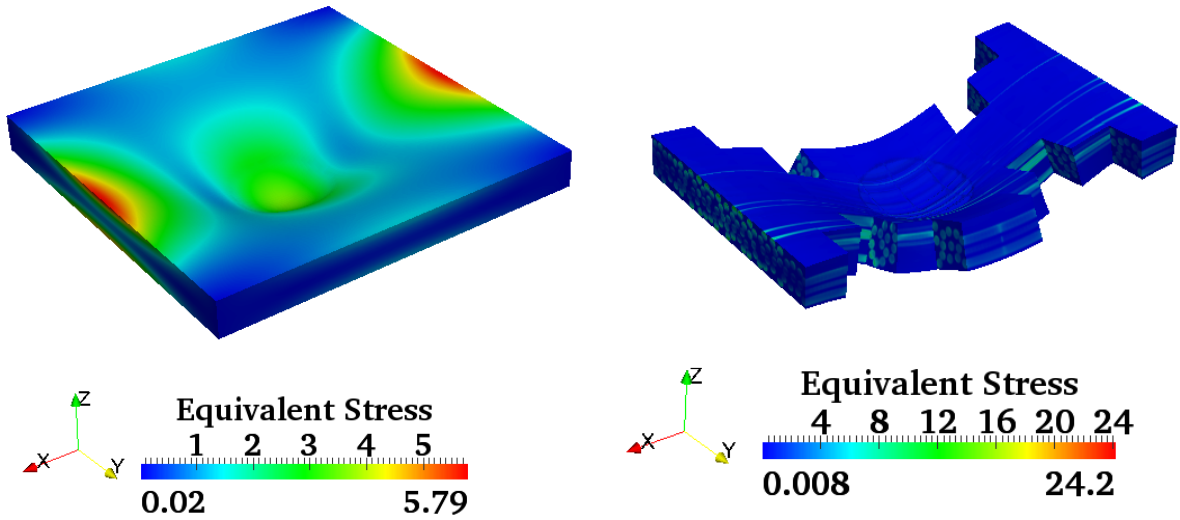
Figure 9.5: Equivalent stress $\boldsymbol{\sigma}_{eq}$ contours for a) the homogenized body on the left and b) the subdomains used in the solution space on the right with $\alpha = 0.8$.
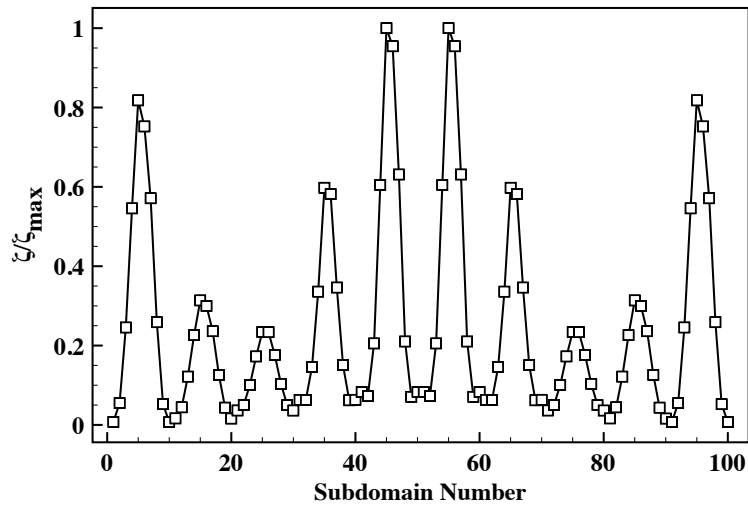
Figure 9.6: This figure shows the variation of the fraction $\frac{\zeta_k}{\zeta_k^{max}}$ in each subdomain. This identifies the regions with high local error.
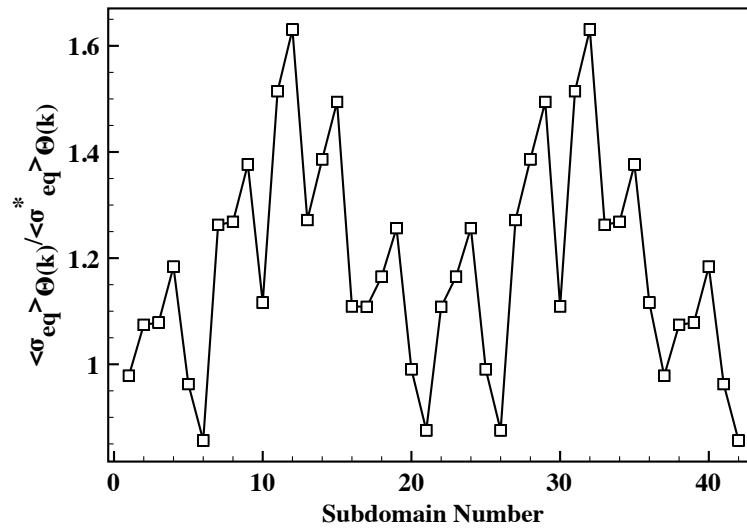
Figure 9.7: Plot of the ratio of the average equivalent stress from the subdomain calculation to the average equivalent stress of homogenized solution in each subdomain

shown in Table. 9.4. For the multiscale simulations we use the block with 36 fibers and it is broken up into a total number of subdomains ranging between 8 and 27. Figure. 9.8 shows the percent change in solution error $\%\Delta e$ for the three different mismatch ratios $\kappa = [5, 10, 52]$. Again, with this example we are able to achieve a significant improvement in the solution space. We also see that $\%\Delta e$ has a dependence on the increment step similar to what has been observed in the previous examples.
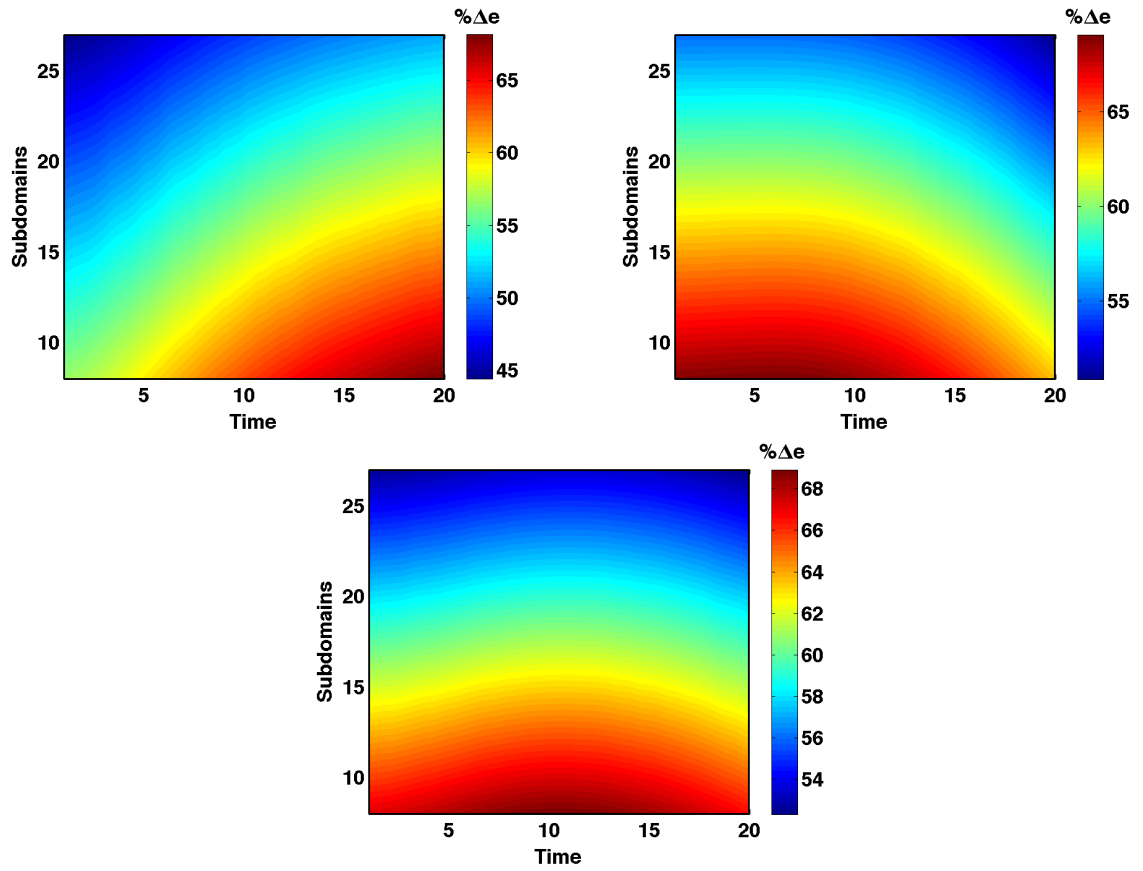
Figure 9.8: Percent change in error $\%\Delta e$ for shear along fiber direction for 1) $\kappa = 52$ which is shown in the top left, 2) $\kappa = 5$ which is shown in the top right ,3) $\kappa = 10$ which is shown in the bottom center.

Table 9.4: Errors for shear along fiber direction at different time increments and different mismatch ratios

	Increment	1	5	10	15	20
Mismatch 5	$\frac{\zeta}{\|\mathbf{u}^*\|_{E(\Omega)}}$	1.030	1.029	1.026	1.022	1.016
	$\frac{\|\mathbf{u}-\mathbf{u}^*\|_{E(\Omega)}}{\|\mathbf{u}^*\|_{E(\Omega)}}$	0.521	0.509	0.478	0.441	0.405
	$\frac{\zeta}{\|\mathbf{u}-\mathbf{u}^*\|_{E(\Omega)}}$	1.978	2.024	2.149	2.316	2.505
Mismatch 10	$\frac{\zeta}{\|\mathbf{u}^*\|_{E(\Omega)}}$	1.354	1.354	1.354	1.353	1.352
	$\frac{\|\mathbf{u}-\mathbf{u}^*\|_{E(\Omega)}}{\|\mathbf{u}^*\|_{E(\Omega)}}$	0.697	0.677	0.641	0.613	0.578
	$\frac{\zeta}{\|\mathbf{u}-\mathbf{u}^*\|_{E(\Omega)}}$	1.943	1.998	2.113	2.207	2.339
Mismatch 52	$\frac{\zeta}{\|\mathbf{u}^*\|_{E(\Omega)}}$	1.929	1.929	1.929	1.929	1.931
	$\frac{\|\mathbf{u}-\mathbf{u}^*\|_{E(\Omega)}}{\|\mathbf{u}^*\|_{E(\Omega)}}$	0.986	0.947	0.894	0.856	0.831
	$\frac{\zeta}{\|\mathbf{u}-\mathbf{u}^*\|_{E(\Omega)}}$	1.957	2.036	2.159	2.254	2.324

Chapter 10

Conclusions

In this work, both multiscale modeling and homogenization of composite materials was addressed. In the context of this work the process of homogenization and multiscale modeling were separate entities. Each one was addressed independently and the connection between the two was addressed.

The homogenization analysis was limited to linear elasticity where special attention was dedicated to understanding the effect of using randomly positioned unidirectional fibers. The RVE size was determined by successively enlarging the size until material parameters converged. Also, given the random nature of the fibers it was necessary to conduct ensemble averages for a given RVE size. Parameter studies were conducted with different material properties and varying volume fractions. It was observed that for smaller volume fraction a larger RVE size was needed, which made the numerical experiments more intensive. The results in turn were compared to analytical bounds of varying degree of accuracy. To conduct these numerical tests two types of material tests were explored, the first did not account for the assumed overall transverse isotropy of the material and thus required 6 material tests. On the other hand, the second test assumed that the macroscopic response is transversely isotropic and therefore, only three material tests were needed to obtain the material properties.

On the multiscale front, we assumed that the overall macroscopic constitutive response was known a priori. Hence, the need for a process of homogenization. The overarching theme is then to include specific zones that include the micorstructural information by predicting an error in some norm. To this end we derived an upper bound on the error

between the exact solution and the homogenized solution. The error we defined provided us with a clear understanding of the sources of error when solving a homogenized problem. In particular, we found that the sources of error included 1) the differences in applied traction and resultant traction 2) the satisfaction of divergence of the homogenized strain acting on the exact material properties. However, we noted that this bound was not appropriate for numerical calculations due to the presences of some unknown constants. Therefore, we utilized a bound derived by Zohdi et al. [16]. This bound was analyzed for fiber composites where we found that its accuracy depended on the homogenized macro-properties. Nonetheless, it remained an upper bound. To utilize this bound in a multiscale setting, the global domain was broken up into subdomains over which local error indicators were calculated. These local indicators allowed us to adaptively choose the subdomains we wanted to include in the analysis. Parameter studies were then conducted by changing the material properties, number of sudomains and the type of applied boundary conditions.

For the small strains analysis we looked at the effect the subdomain solutions had on improving the overall solutions space i.e decreasing the modeling error. We found that significant improvement could be achieved by this coupling process. Also, when utilizing only some subdomains in the analysis the computational cost was reduced significantly with little detriment to the overall enhancement of the solution space. We also found that the type of boundary conditions had some effect on the enhancement of the solution space, specifically applying displacement control conditions resulted in a larger decrease in the modeling error.

For large deformations, we assumed the same form of the error indicator as derived for small strains. The analysis proceeded by first establishing the effectiveness of the error bound under these conditions. We compared the exact modeling error to the predicated error and found that for the examples used the predicted error remained an upper bound. We observed however, that it's accuracy was a function of both the type of problem being analyzed and the load increment. We then analyzed the effectiveness of the multiscale process under large deformations and found that a significant reduction in the modeling error can be achieved. In comparison to small deformations, similar trends were observed for the reduction in the modeling error. There was however, a dependence on the load increment as was observed when analyzing the predicted error.

In future work extensions to include inertial effects will be explored. Also, for

large deformations different types of material models should be explored to understand the response of the error indicator. For example Neo-Hookean and Mooney-Rivlin type constitutive laws could be explored.

Bibliography

[1] S Nemat-Nasser and M Hori. *Micromechanics: overall properties of heterogeneous solids*, volume 1. Elsevier, 2nd edition, 1999.

[2] J Aboudi. *Mechanics of composite materials a unified micromechanical approach*, volume 1. Elsevier, 1st edition, 1992.

[3] Muneo Hori and Sia Nemat-Nasser. On two micromechanics theories for determining micro-macro relations in heterogeneous solids. *Mechanics of Materials*, 31:667–682, 1999.

[4] Richard M. Christensen. *Mechanics of Composite Materials*. Dover, 2005.

[5] Bensoussan A, Lionis JL, and Papanicolaou G. *Asymptotic Analysis for Periodic Structures*, volume 1. North-Holland, Amsterdam, 1978.

[6] Jacob Fish and Kamlun Shek. Multiscale analysis of composite materials and structures. *Composites Science and Technology*, 60:2547–2556, 2000.

[7] David H. Allen. Homogenization principles and their application to continuum damage mechanics. *Composites Science and Technology*, 61:2223–2230, 2001.

[8] Kumar K. Tamma Peter W. Chung and Raju R. Namburu. Asymptotic expansion homogenization for heterogeneous media: computational issues and applications. *Composites*, 32:1291–1301, 2006.

[9] Jacob Fish and Amir Wagiman. Multiscale finite element method for a locally nonperiodic heterogeneous medium. *Computational Mechanics*, 12:164–180, 1993.

[10] Somnath Ghosh, Kyunghoon Lee, and Suresh Moorthy. Multiple scale analysis of heterogeneous elastic structures using homogeniation theory and voronoi cell finite element method. *International Journal of Solids and Structures*, 32:27–62, 1994.

[11] F. P. T. Baaijens V. Kouznetsova, W. A. M. Brekelmans. An approach to micro-macro modeling of heterogeneous materials. *Computational Mechanics*, 27:37–48, 2001.

[12] Christian Miehe. Computational micro-to-macro transitions for discretized micro-structures of heterogeneous materials at finite strains based on the minimization of averaged incremental energy. *Comput. Methods Appl. Mech. Engrg*, 192:559–591, 2003.

[13] Frederic Feyel and Jean-Louis Chaboche. FE^2 multiscale apporach for modelling the elastoviscoplastic behavior of long fiber sic/ti composite materials. *Comput. Methods Appl. Mech. Engrg*, 183:309–330, 2000.

[14] Arkaprabha Sengupta, Panayiotis Papadopoulos, and Robert L. Taylor. Multiscale finite element modeling of superelasticity in nitinol polycrystals. *Computational Mechanics*, 43:573–584, 2008.

[15] Ben Nadler, Panayiotis Papadopoulos, and David J. Steigmann. Multiscale constitutive modeling and numerical simulation of fabric material. *International Journal of Solids and Structures*, 43:206–221, 2006.

[16] Tarek I.Zohdi, J.Tinsley Oden, and Gregory J.Rodin. Hierarchical modeling of hetrogeneous bodies. *Comput.Methods Appl. Mech.Engrg*, 138:273–298, 1996.

[17] Tarek I. Zohdi J.Tinsely Oden. Anaylsis and adaptive modeling of highly heterogeneous elastic structures. *Computer Methods Applied Mech. Engrg*, 148:367–391, 1997.

[18] P.Chadwick. *Continuum Mechanics: Concise Theory and Problems*, volume 1. Dover Publications, New York, 1st edition, 1999.

[19] A.J.M. Spencer. *Continuum Mechanics*, volume 1. Dover Publications, New York, 1st edition, 1980.

[20] Gerhard A. Holzapfel. *Nonlinear Solid Mechanics*. Wiley, 1st edition, 2007.

[21] R.W. Ogden. *Non-linear Elastic Deformations*. Dover, 1984.

[22] A.J.M. Spencer. *Continuum Theory of the Mechanics of Fibre-reinforced composites.* Wiley, 4th edition, 2002.

[23] T.J.R. Hughes and K.S. Pister. Consistent linearization in mechanics of solids and structures. *Computer and Structures*, 8:391–397, 1978.

[24] Thomas J.R. Hughes. *The Finite Element Method.* Dover, New York, 5th edition, 2000.

[25] O. C. Zienkiewicz and R. L. Taylor. *The Finite Element Method*, volume 1. McGraw Hill Book Company, London, 5th edition, 2000.

[26] Ted Belytschko, Wing Kam Liu, and Brian Moran. *Nonlinear Finite Elements for Continua and Structures.* Wiley, 1st edition, 2004.

[27] Plesha Cook, Malkus and Witt. *Concepts and Applications of Finite Element Analysis.* Springer, 1984.

[28] C.T.Sun and R.S Vaidya. Prediction of composite properties from a representative volume element. *Composites Science and Technology*, 56:171–179, 1996.

[29] Tarek I. Zohdi and Peter Wriggers. *An Introduction to Computational Micromechanics*, volume 20. Springer, 2nd edition, 2005.

[30] I.Temizer and T.I.Zohdi. A numerical method for homogenization in non-linear elasticity. *Computational Mechanics*, 40:281–298, 2007.

[31] S.Loehnert and P.Wriggers. Effective behavior of elastic heterogeneous thin structures at finite deformations. *Computational Mechanics*, 41:595–606, 2008.

[32] Z.F.Khisaeva and M. Ostoja-Starzewski. On the size of rve in finite elasticity of random composites. *Journal of Elasticity*, 85:153–173, 2006.

[33] T. Kanit, S. Forest an d I. Galliet, V. Mounoury, and D. Jeulin. Determination of the size of the representative volume element for random composites: statistical and numerical approach. *International Journal of Solids and Strucutures*, 40:3647–3679, 2003.

[34] Ilker Temzier. *Homogenization in Linear and Non-Linear Elasticity*. PhD thesis, Berkeley, CA, 2005.

[35] R. Hill. Elastic properties of reinforced solids: Some theoretical principles. *J.Mech.Phys.Solids*, 11:357–372, 1963.

[36] C. Huet. Application of variational concepts to size effects in e heterogeneous bodies. *J.Mech.Phys.Solids*, 38:813–841, 1990.

[37] Z. Hashin and W. Rosen. The elastic moduli of fiber reinforced materials. *J.Appl. Mech*, 31:223, 1964.

[38] O. C. Zienkiewicz and R. L. Taylor. *The Finite Element Method for Solid and Structural Mechanics*, volume 1. McGraw Hill Book Company, London, 6th edition, 2005.

[39] Mark Ainsworth and J. Tinsley Oden. A posteriori error estimation in finite element analysis. *Comput. Methods Appl. Mech. Engrg*, 142:1–88, 1997.

[40] Leszek F.Demkowicz J.Tinsley Oden. *Applied Functional Analysis*. CRC, 1996.

[41] Dietrich Braess. *Finite elements Theory, fast solvers, and applications in solid mechanics*. Cambridge, 2nd edition, 2001.

[42] Patrick M. Knupp. On the invertibility of the isoparametric map. *Computer Methods in Applied Mechanics and Engineering*, 78:313–329, 1989.

[43] V. Murti, Y. Wang, and S. Valliappan. Numerical inverse isoparametric mapping in 3d fem. *Computers and Structures*, 29:611–622, 1987.

[44] K. Y. Yuan, Y.S. Huang, H.T. Yang, and T. H. H. Pian. The inverse mapping and distortion measures for 8-node hexahedral isoparametric elements. *Computational Mechanics*, 14:189–199, 1994.

Appendix A

Finite Element Algorithms

For this research a self authored finite element code was in Fortran 90. In this appendix, the integration schemes, conjugate gradient methods and sparse storage techniques are elaborated on.

A.1   Sparse Storage

To reduce both memory cost and computational costs we make use of the sparsity of the stiffness matrix $\mathbf{K}_T$ in finite elements and write a sparse storage module. The basic structure is developed in a Fortran module by defining a TYPE. We have

```
TYPE Sparse
      integer, pointer    :: columns(:)
      real, pointer       :: values(:)
      integer, pointer    :: entries
END TYPE
```

where column(:) identifies the column numbers, values(:) identifies the value at the specific column, and entries identifies the number of values in the column. To generate a matrix we simply create a TYPE Sparse with dimensions equal to the number of rows. In other words, we define TYPE(SPARSE) :: SMatrix(rows). Then for a given row we have column, value and entries information This gives us the basic data structure for the sparse matrix. To work with data structure, we allow it be dynamic. Therefore, the length of the columns and values vectors can change throughout the execution time.

Various subroutines are then introduced in the module that allow us to specifically,

- Initialize the sparse matrix

- Assign values

- Addition of values

- Perform matrix vector multiplication.

A.2 Integration Schemes

When building the tangent stiffness $\mathbf{K}_T$ we must perform numerical integration. Recall the form of the stiffness matrix as

$$\mathbf{K}_T = \underbrace{\int_\Omega F_{iA}\frac{\partial N_I}{\partial X_A}\frac{\partial S_{AB}}{\partial E_{CD}}F_{jC}\frac{\partial N_J}{\partial X_D}d\Omega}_{\mathbf{K}_{mat}} + \underbrace{\delta_{ji}\int_\Omega \frac{\partial N_I}{\partial X_A}S_{AB}\frac{\partial N_J}{\partial X_B}d\Omega}_{\mathbf{K}_{geo}} \tag{A.2.1}$$

to perform this integral numerically we utilize gauss quadrature. Guassian quadrature is a method that can allow exact integration of a polynomial of degree 2n-1, where n is the number of gauss points. For a 1 dimensional case we have the following

$$\int_{-1}^{1} f(\zeta)dx \approx \sum_{i=1}^{n} w_i f(\zeta_i) \tag{A.2.2}$$

where the domain of integration is always taken from [-1,1] and w_i are the weights corresponding to the gauss coordinates ζ_i. The weights and points for different gauss rules are summarized in Table. A.1.

assuming the limits of the integral are from [-1,1] we can now express the integral for the stiffness matrix as

$$\mathbf{K}_T = \sum_{i=1}^{n}\sum_{j=1}^{n}\sum_{k=1}^{n} w_i w_j w_k F_{iA}\frac{\partial N_I}{\partial X_A}\frac{\partial S_{AB}}{\partial E_{CD}}F_{jC}\frac{\partial N_J}{\partial X_D} \tag{A.2.3}$$

$$+ \sum_{i=1}^{n}\sum_{j=1}^{n}\sum_{k=1}^{n} w_i w_j w_k F_{iA}\frac{\partial N_I}{\partial X_A}S_{AB}\frac{\partial N_J}{\partial X_B} \tag{A.2.4}$$

Table A.1: Gauss Quadrature Rules

Gauss Points n	Coordinates ζ_i	Weights w_i
1	0	2
2	$\pm\frac{1}{\sqrt{3}}$	1
3	0	$\frac{8}{9}$
	$\pm\sqrt{\frac{3}{5}}$	$\frac{5}{9}$
4	$\pm\sqrt{3-2\sqrt{6/5}/7}$	$\frac{18+\sqrt{30}}{36}$
	$\pm\sqrt{3+2\sqrt{6/5}/7}$	$\frac{18-\sqrt{30}}{36}$
5	0	$\frac{128}{225}$
	$\pm\frac{1}{3}\sqrt{5-2\sqrt{10/7}}$	$\frac{322+13\sqrt{70}}{900}$
	$\pm\frac{1}{3}\sqrt{5+2\sqrt{10/7}}$	$\frac{322-13\sqrt{70}}{900}$

where all the arguments are evaluated at the gauss coordinates $(\zeta_i, \zeta_j, \zeta_k)$. We note that generally, the limits are not from [-1,1] and hence we must conduct a mapping that rewrites the integral in a manner amenable to gauss quadrature. When doing FEM this is achieved when using the isoparametric mappings.

A.3 Conjugate Gradient

To solve the systems of equations that arise when you using the finite element method we utilize the iterative scheme known as the conjugate gradient method. The algorithm is presented in Alogorith. 2 where we want to solve $\mathbf{K}_m\mathbf{x} = \mathbf{b}$

Algorithm 2 Algorithm for conjugate gradient
___
Given matrix $\mathbf{K}_m$ and $\mathbf{b}$ find $\mathbf{x}$

Set Tolerance for convergence

Select a starting guess $\mathbf{x}^i$

$\mathbf{r}^i = \mathbf{b} - \mathbf{K}_m \mathbf{x}^i$

Set $\mathbf{s}^i = \mathbf{r}^i$

$error = \frac{||\mathbf{r}^i||}{||\mathbf{x}^i||}$

while $error >$ TOL **do**

    $\mathbf{Ks} = \mathbf{K}_m \mathbf{s}^i$

    $r_{norm} = \mathbf{r}^i . \mathbf{r}^i$

    $\alpha = \frac{r_{norm}}{\mathbf{s}^i . \mathbf{Ks}}$

    $\mathbf{x}^{i+1} = \mathbf{x}^i + \alpha \mathbf{s}^i$

    $\mathbf{r}^{i+1} = \mathbf{r}^i - \alpha \mathbf{Ks}$

    $\beta = \frac{\mathbf{r}^{i+1} . \mathbf{r}^{i+1}}{r_{norm}}$

    $\mathbf{s}^{i+1} = \mathbf{r}^{i+1} + \beta \mathbf{s}^i$

    $error = \frac{||\mathbf{r}^{i+1}||}{||\mathbf{x}^{i+1}||}$

end while
___